PREPARATION, CHARACTERIZATION, AND ACTIVITY OF MONO-DISPERSED SUPPORTED CATALYLSTS

A Thesis

Presented to

The Academic Faculty

By

Tanya Hicks

In Partial Fulfillment

Of the Requirements for the Degree

Master of Science in Chemical Engineering in the

School of Chemical & Biomolecular Engineering

Georgia Institute of Technology

August 2004

PREPARATION, CHARACTERIZATION, AND ACTIVITY OF MONO-DISPERSED SUPPORTED CATALYSTS

Approved by:

Dr. Pradeep K. Agrawal, Chairman

Dr. Andreas S. Bommarius

Dr. F. Joseph Schork

Date Approved: 8/3/2004

ACKNOWLEDGEMENTS

Much gratitude is due to my advisor, Dr. Pradeep K. Agrawal, for his guidance and assistance during my research at Georgia Tech. Thank you for helping me expand my research and technical thinking skills. Thank you to the members of my committee, Dr. Andreas S. Bommarius and Dr. F. Joseph Schork, for their valuable insight concerning my project. A collective thanks goes to the ChBE staff and faculty for making my matriculation at Georgia Tech a memorable experience I will always cherish.

I must also thank several undergraduate, graduate, and postdoctoral students who were instrumental to the completion of my research. Much appreciation goes to members of Dr. Agrawal's research group – Dr. Limin He and Li Xue – for their generosity, insight, and patience. I would also like to thank Chris Hebing for his assistance and insight throughout my research experience. Thank you to Jim Russum and the members of Dr. Schork's research group for allowing me to use their lab equipment frequently. Thanks also go to Yolande Berta for her assistance during EM use. I must also recognize the FCGS, BGSA, AChEGS, and FACES Fellowship Program for providing a social outlet and opportunities for professional development here at Georgia Tech.

I would like to thank my family for their continuous love, encouragement, and support that kept me motivated during my studies. To my mother, sisters, grandparents, and the rest of my family, your confidence in my abilities is greatly appreciated, and I strive to make you proud. Grandfather, your encouraging words are forever in my heart, and thank you for the motivation you instilled in me at an early age. Lastly, all thanks go to my greatest inspiration – God.

TABLE OF CONTENTS

LIST OF TABLES

LIST OF FIGURES

LIST OF SYMBOLS and ABBREVATIONS

Symbol or Abbreviation	Meaning
A	Autocorrelation function constant or frequency factor
A.B.D.	Average bed density (g/cm^3)
A_c	Surface area of crystallite (nm^2, cm^2)
AFM	Atomic force microscopy
B	Autocorrelation function constant
$C(\tau)$	Autocorrelation function
CTAB	Cetyltrimethylammonium bromide
D	Diffusion coefficient (m^2/s)
d	Diameter (m, cm, nm)
d_c	Crystallite diameter (nm, cm)
DLS	Dynamic light scattering
d_m	Micelle diameter (nm)
E_a	Activation energy (cal/mol, J/mol)
EDS	Energy dispersive X-ray microanalysis
Γ	Decay rate
GC	Gas chromatogram
η	Solvent viscosity (kg/m/s)
IEP	Isoelectric point
IRAS	Infrared reflection absorption spectroscopy
k	Specific reaction rate (molecules reacted/site/s)
k_B	Boltzmann's constant (1.38×10^{-16} erg/molecule/K)
λ	Laser wavelength (m)
MSI	Metal-support interaction
n	Refractive index or number of molecules
O/A	Oil-to-aqueous phase molar ratio
O/W	Oil-in-water microemulsion
π	3.14
Pd	Polydispersity
P_{ethane}	Partial pressure of ethane (torr)
P_{H2}	Partial pressure of hydrogen (torr)
q	Scattering vector
θ	Scattering angle (rad)

R	Ratio of Ni(100) to Ni(111) surface area or gas constant (1.987 cal/mol/K)
RHA	Rice husk ash
SDS	Sodium dodecyl sulfate
SEM	Scanning electron microscopy
SFG	Sum frequency generation
STM	Scanning tunneling microscopy
t	Time (min)
τ	Time (μs)
T	Temperature (K or C)
TEM	Transmission electron microscopy
TOF	Turnover frequency (molecules reacted/site/s)
TON	Turnover number (molecules reacted/site/s)
TPD	Temperature-programmed desorption
TPR	Temperature-programmed reduction
V_c	Crystallite volume (nm3, cm3)
V_m	Volume of micelle (nm^3)
W/O	Water-in-oil microemulsion
W_o	Water-to-surfactant molar ratio
x	X-axis value
X	Magnification
y	Y-axis value

SUMMARY

Mono-dispersed supported Ni catalysts were synthesized using the water-CTAB-hexanol reverse micellar system. The core of the reverse micelles contained an aqueous solution of $NiCl_2$. Dynamic light scattering measurements showed that microemulsions having a water-to-surfactant molar ratio, W_o, of 10 led to reverse micelles with lowest polydispersity, longest stability, and size range of interest. At an oil-to-aqueous phase ratio of 2, the diameter of the reverse micelles was found to increase with W_o in a linear fashion. At higher values of W_o (i.e. 25-30), the polydispersity was found to increase when lowering the amount of surfactant in the system. Ultimately, $O/A = 2$ and $W_o = 10$ were chosen as optimal conditions for microemulsion preparation.

The aqueous $NiCl_2$ concentration within the micelles was varied between 0.1 and 0.001 M. DLS results showed that although the average micelle diameter was between 70-83 nm throughout the range of metal salt concentrations, the crystallite size estimate based upon the reported micelle diameter and known aqueous $NiCl_2$ concentration ranged between 2 to 7 nm. Therefore, the Ni crystallite size was varied by changing the aqueous $NiCl_2$ concentration due to instability issues arising when changing the value of W_o.

After deposition onto an alumina mesh support, the particles were dried, calcined, and reduced to produce Ni clusters. SEM and EDS analysis was used to confirm the presence of Ni compounds after the calcination stage. By the varying the aqueous $NiCl_2$ concentration within the micelles, .0039, .0013, and .00039 wt. % Ni catalysts were produced and characterized using SEM. Particles in the size range of 10-14 nm were noticed for the .0039 wt. % Ni catalysts after reduction, 7-11 nm for .0013 wt. % Ni, and

5-9 nm for .00039 wt. % Ni. The lower-end of these particle size ranges was comparable to the crystallite size estimates.

Ethane hydrogenolysis and ethylene hydrogenation reactions were conducted over the emulsion-prepared catalysts in order to determine particle size effects on catalytic activity. Results showed that the catalytic activity, defined in terms of per unit metal surface atom (or *TON*, turnover number), decreases with increasing particle size for the hydrogenolysis reaction. This trend may be due to an intrinsic size effect in which smaller particles exhibit the chemical or structural properties necessary for achieving a higher reaction rate. The results for ethylene hydrogenation showed that the reaction rate did not significantly change with crystallite size, confirming that the reaction is facile or structure-insensitive.

CHAPTER 1

INTRODUCTION

A catalyst is a substance that increases the rate at which a chemical reaction reaches equilibrium, without being consumed in the process. Catalysis is often simply referred to as the phenomenon of a catalyst at work. In the past, catalyst preparation methods such as impregnation, incipient wetness, and deposition-precipitation have been used with the main goal of obtaining a high degree of dispersion by attaching small metal particles to relatively inert surfaces, which is typically a high surface area oxide. These supported metal catalysts are composed of 0.1-20 wt. % of a metal from Groups II-VIII dispersed over the surface of a support [1]. They are widely used on an industrial scale and in research laboratories. Large-scale uses of the catalysts include hydrogenation of animal and vegetable oils, petroleum reforming to make high-octane gasoline, and treatment of vehicle exhaust to minimize environmental pollution.

In recent years, the preparation of metal catalysts via colloidal solutions of the metals has been investigated because the method promises enhanced control over particle size and morphology, with direct preparation of the metal component by reduction of the metal ions in solution. In particular, reverse micelles containing aqueous pools of the aqueous salt solution can be prepared. The solution, known as a microemulsion, can be key in controlling the size distribution of small metal clusters formed because the size of the micelles can be easily dictated by varying the water-to-surfactant ratio, W_o [2, 3]. Furthermore, varying the concentration of the active metal salt within the aqueous solution can also alter the size of the metal particles by changing the total number of

metal atoms in a cluster [3, 4]. Thus, as compared to traditional catalyst preparation techniques, the use of microemulsions allows one to better control the size of the metal particles and to obtain a more uniform particle size distribution. Another advantage of this technique is that it can be used with a wide array of support materials [5].

Due to the uniformity of the metal particles formed using reverse micelles, one has the potential means of developing catalysts with a uniform particle distribution. Using these types of catalysts, one can better ascertain the effects of particle size on catalytic activity. Therefore, the goal of this research is to determine the size-activity relationship of nano-sized, mono-dispersed supported nickel catalysts for various reaction types. Traditional methods of preparing supported metal catalysts, such as impregnation and deposition-precipitation, often have metal particles with a very broad size distribution (2-50 nm). Using these techniques, it is difficult to determine the role of metal crystallite size on the activity of the catalysts. Using reverse micelles, several batches of supported nickel catalysts will be prepared, each with a very narrow size distribution. The effect of metal crystallite size on catalytic reaction yield will be determined. A variety of characterization techniques are employed to determine the size, size distribution and activity of the nickel crystallites prepared using water-in-oil microemulsions.

Chapter 2 focuses on the basic principles of catalysis, factors that affect the activity, lifetime, and selectivity of catalyst, traditional catalyst preparation methods and microemulsion techniques used to prepare nano-sized metal crystallites. Previous research done utilizing microemulsions to prepare nano-sized metal particles is also presented. In Chapter 3, the process of using microemulsions to prepare mono-dispersed supported catalysts is described in detail. The reaction setup and trials are also outlined in

this chapter. The experimental procedures used to synthesize and characterize the catalysts are described. Challenges and obstacles encountered during catalyst preparation and experimentation are noted. Experimental results and their interpretations are presented in Chapter 4. Chapter 5 presents the conclusions and recommendations for future work.

CHAPTER 2

BACKGROUND

2.1 CATALYSIS

2.1.1 Purpose of Catalysis

By definition, a catalyst is a substance, usually metal, that affects the rate of a reaction but itself remains unchanged after the reaction process. A catalyst can either accelerate or slow down the formation of a particular product, but it does not affect the equilibrium of the reaction. Usually, a catalyst is thought to alter the reaction rate by promoting a different molecular mechanism for the reaction. For instance, gaseous hydrogen and oxygen are practically inert at room temperature, but react quickly when exposed to platinum. Figure 2.1 shows the progress along each reaction path as H_2 and O_2 approach and surpass the activation energy barrier to form H_20 [6]. Another interpretation of the role of catalyst is that of reducing the activation energy barrier of a reaction, thus increasing the reaction rate.

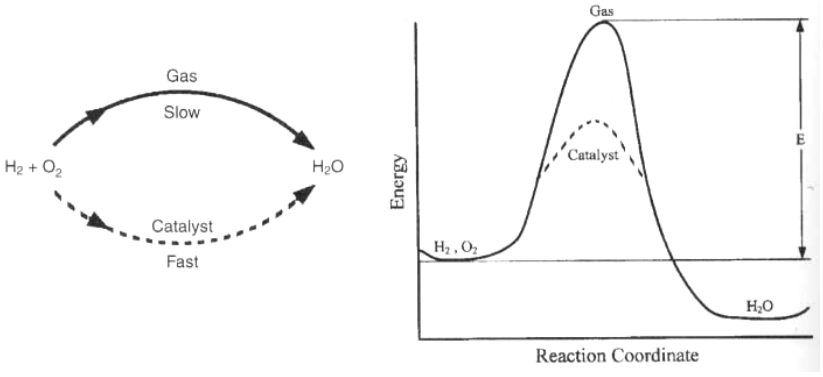

Figure 2.1 Reaction paths with and without catalyst use [6].

Catalysis is the occurrence, study, and use of catalysts and catalytic processes. Approximately one-third of the chemical gross national product of the U.S. involves a catalytic process somewhere between the raw materials and finished products. Presently, the emphasis of catalysis research has significantly shifted from traditional applications in petroleum and bulk chemical production to the synthesis of fine chemicals, agro- and oleo-chemicals, pharmaceuticals and environmental protection systems [5]. Due to these various applications, the field of catalysis research continues to be of importance in many scientific fields.

2.1.2 Types of Catalysis

A catalytic process can occur in either of two ways – homogeneous or heterogeneous. In homogeneous catalysis, the catalyst is in the same phase as at least one of the reactants. A heterogeneous catalytic process involves more than one phase. Usually, the catalyst is a solid and the reactants are in the liquid or gaseous phases. The heterogeneous catalytic reaction occurs at or very near the fluid-solid interface. Of these two forms of catalysis, heterogeneous is the most common type. The often simple and complete separation of the fluidic products from the solid catalyst makes heterogeneous catalysis economically favorable, especially because many catalysts are very valuable, and their reuse is highly desirable for the economic viability of the process [6].

2.1.3 Catalytic Reactions

Referring to the effects of catalyst structure on reaction rate, catalytic reactions can be labeled as either demanding or facile [4]. For demanding reactions, the ensemble

structure of the metal atoms composing the catalyst greatly affects the reaction rate. The structure of the metal atoms is known to vary with the crystallite size. Thus, the activity of metal clusters of different crystallite size has been found to vary with particle size. Therefore, these reaction types are termed "structure-sensitive" [4]. For facile reactions, the reaction rate is not affected by the structure of the metal surface atoms. A constant activity is observed as a function of crystallite size. This reaction type is known as "structure-insensitive" [4]. Both of these reaction types are extensively used in catalytic research to investigate structure-reactivity relationships for the different catalyst types.

2.1.4 Catalyst Properties

Several factors are known to affect the activity, lifetime, and selectivity of catalysts. These factors include the type of catalytic support used, crystallite size effects, and various types of catalyst deactivation. The following sections outline the significance of these factors in catalyst preparation and use.

A. Catalytic Supports

Most active catalysts are small metal particles that are thermodynamically unstable with respect to the bulk material. Since catalytic reactions occur at the fluid-solid interface, any effort to increase this interfacial area requires using small metal clusters or particles. The driving force towards coalescence is equal and opposite to the work performed in subdividing the bulk material. The smaller the catalytic particles, the less stable they are. The atoms are the least stable of all. Material handling issues are important when trying to prepare nano-sized metal particles that are uniformly dispersed

on the support surface. Therefore, a catalyst preparation mechanism that prevents the coalescence of particles is necessary to obtain high dispersions [1]. The degree of metal dispersion is defined as the ratio of surface metal atoms to the total metal atoms in the catalyst. The higher the degree of dispersion, the more efficient the catalyst becomes.

One solution for preventing the coalescence of small particles involves the use of catalytic supports. The metal particles are formed and are allowed to attach to the surface of the support, which is often a high-area oxide. For many applications, the support must have a high surface area in order to enable crystallites of the active phase to be well separated from one another. Furthermore, it is generally desirable for the support to be catalytically inert. Some commonly used catalyst supports include zeolites, silica, alumina, magnesia, and carbon. Some common shapes and sizes of catalyst particle supports are illustrated in Figure 2.2.

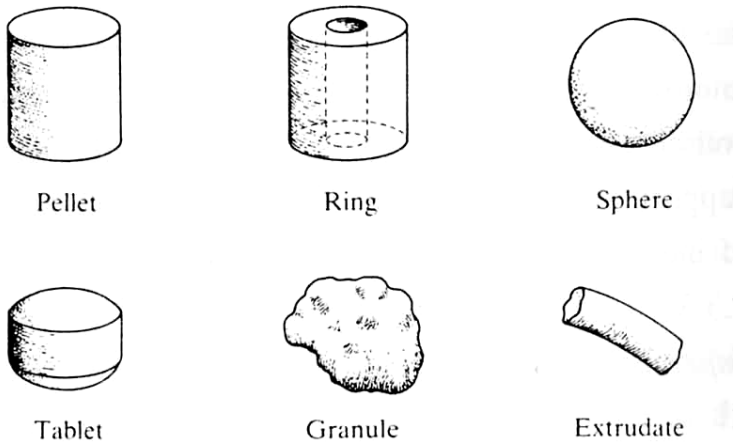

(a)

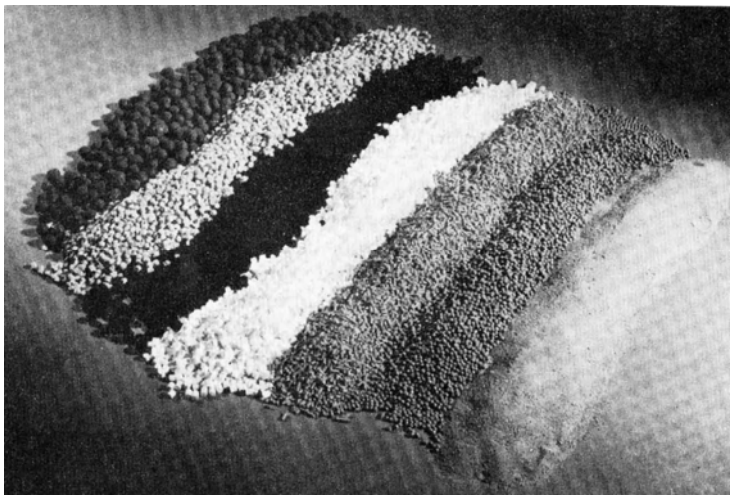

(b)

Figure 2.2 **a) Shapes of catalyst particles used in a fixed bed reactor [1].**
b) Different sizes and shapes of catalysts [6].

Because well-dispersed metal crystallites may have a size on the nano-scale, these metal atoms tend to undergo surface diffusion resulting in movement along the surface. The metal particles will aggregate together to reduce their surface energy and become more stable. Eventually, large particles form, and the surface area as well as the activity of the metal catalyst are reduced. This phenomenon is known as sintering, and it is facilitated at high temperatures and by weak interactions between the metal and support. On the contrary, when the support is composed of a metal oxide such as Al_2O_3, the metal-support interaction (MSI) will deter the surface migration. With the use of strong supports, a higher dispersion and greater particle stability can be achieved at higher reaction temperatures.

B. Particle Size Effects

In heterogeneous catalysis, the catalytic activity of the supported metal depends on the degree of dispersion of the metal on the support. The catalytic activity increases with increasing surface area or, that is, decreasing crystallite size. While the importance of crystallite size has been recognized in terms of dispersion, researchers are still gathering information to determine if the effect of crystallite size is limited to the effect on surface area, or whether there are other phenomena occurring due to crystallite size effects. Because understanding the size-dependent electronic, structural and chemical properties of metal clusters on oxide supports is an important aspect of heterogeneous catalysis, much catalytic research has been conducted to elucidate the structure-reactivity relationship of supported catalysts. The most difficult part in discovering the size-dependent behavior is the preparation of mono-dispersed clusters supported on oxide

supports. Furthermore, apart from preparing the catalysts, conductivity issues with the sample has to be addressed so that characterization is possible using techniques such as scanning electron microscopy (SEM), transmission electron microscopy (TEM), scanning tunneling microscopy (STM), and atomic force microscopy (AFM). Different types of supports, such as metal oxide thin films, have proved to be promising in investigating particle size effects [7-11]. Ultimately, in terms of studying particle size effects, identifying new ways of preparing model catalyst is an important step in bridging the gap between fundamental studies of single crystal activity and studies of high-surface area catalyst activities.

C. Catalyst Deactivation

Most catalysts experience deactivation, which means the catalytic activity declines as time progresses. Catalyst deactivation can occur by several mechanisms, including aging, poisoning, and coking. The aging phenomenon can be characterized by a gradual change in surface crystal structure or by the loss of active surface. The deposition of foreign materials, such as impurities present in the feed, on active sites of the catalytic surface is commonly known as poisoning or fouling. Coking refers to the deposition of carbon on the catalyst. This phenomenon is very common in the catalytic cracking of petroleum napthas. Due to coking, the catalyst has to be frequently removed from the reaction or undergo regeneration before reuse. Therefore, while running a catalytic reaction, potential causes for catalyst deactivation must be addressed to obtain optimal activity. Often, the catalyst configurations and operating conditions are adjusted to minimize the effect of catalyst deactivation.

2.1.5 Catalyst Preparation Methods

Many techniques have been used to prepare supported metal catalysts. The following section describes some of the most commonly used processes for catalyst preparation, including experimental methods and underlying chemical interactions at the support surface.

A. Impregnation and Incipient Wetness

Numerous methods have been developed for the preparation of catalytic metal particles. The most widely used methods involve the introduction of a simple or complex salt ion containing the metal to the support, followed by reduction [1]. In the process of impregnation, a solution of the metal precursor (Fe, Co, Ni, Cu, etc.) is drawn into the void pores of the catalyst support material. In a similar process referred to as incipient wetness, the volume of solution is taken so that the pores of the support are filled. The solution, added quickly to support, is absorbed completely. After absorption onto the support, the sample is dried and calcined in order to produce active metal crystallites.

Although incipient wetness impregnation is the simplest catalyst preparation procedure, the method does not result in the best dispersion of metal on the support. However, impregnation does provide easier control of metal loading and minimal liquid waste generation. Chang et al. [12] used the incipient wetness impregnation method to prepare nickel catalysts supported on rice husk ash (RHA)-alumina. In Figure 2.3a, unsupported nickel oxide, NiO, compounds are shown. Using temperature-programmed reduction (TPR), Chang et al. used the single reduction peak of unsupported NiO to identify the bulk NiO on the Ni/RHA-Al_2O_3 catalyst samples. Their TPR profiles of all

Ni/RHA-Al_2O_3 catalysts included a broad peak, which corresponded to the reduction of NiO. They also noted that the NiO obtained in the absence of the support was more easily reduced than supported NiO because of MSI effects on the latter. Figure 2.3b shows the surface structure of the alumina dispersed on rice husk ash. The surface of the rice husk ash is covered with a layer of amorphous structure that does not resemble the unsupported NiO. Referring to Figures 2.3c and d, the catalyst precursors resembled a quasi-meshy structure with mesh sizes of about 0.06-0.2 μm. The formation of the meshy structure was attributed to the replacement of the support pores by NiO with an increase in Ni loading. At high nickel loading, the agglomeration appeared due to the formation of multi-layer NiO that blocked the micropores of the support material. Using the catalyst prepared by incipient wetness, they concluded that higher nickel loadings results in the formation of bulk NiO, which in turn decreases the number of active sites.

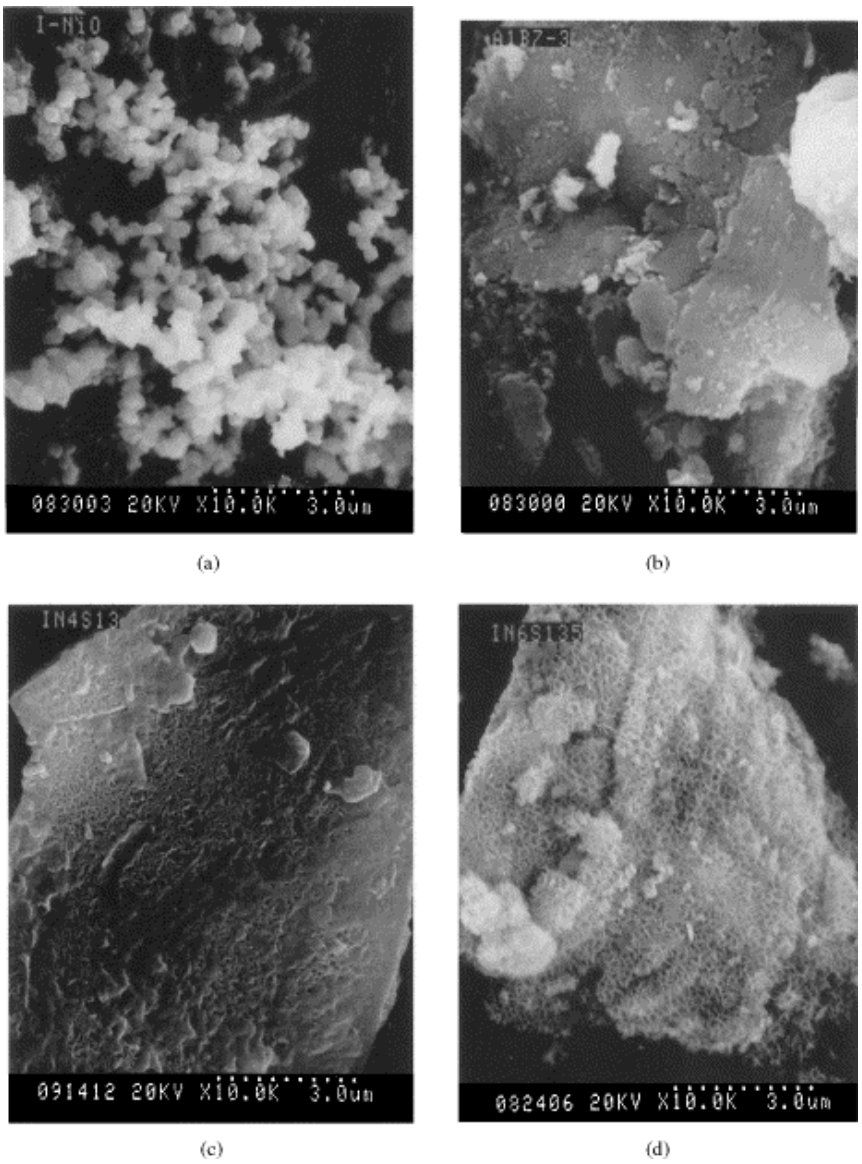

Figure 2.3 **SEM images of (a) unsupported NiO (10,000 X); (b) RHA-Al_2O_3 support (10,000 X); (c) 15 wt. % Ni/ RHA-Al_2O_3 catalyst precursors after drying at 110 ˚C (10,000 X); (d) 25 wt. % Ni/ RHA-Al_2O_3 catalyst precursors after calcinations at 500 ˚C (10,000 X) [12].**

B. Adsorption from Solution and Ion Exchange

The principles of adsorption from solution and ion exchange are based on the amphoteric properties of the support-surface hydroxyl groups that generate surface charges depending on the pH value. Figure 2.4 is a schematic showing the surface hydroxyl groups that are formed on a alumina surface obtained by cutting a groove on a (100) face of a spinel crystal of alumina [13]. I_a, I_b, III_a, and III_b represent different kinds of surface hydroxyl groups.

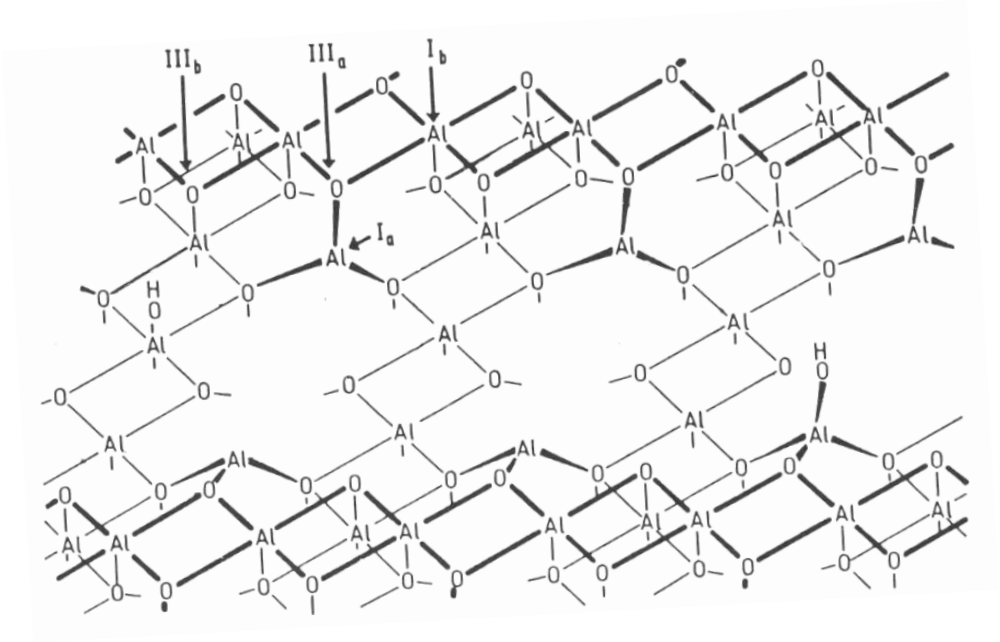

Figure 2.4 Surface hydroxyl groups on a (100) face of a spinel crystal of alumina [13].

The surface charges generated by the surface hydroxyl groups attract ions of the opposite charge, and these ions become electrostatically fixed to the support surface. The isoelectric point, *IEP*, is defined as the pH of a solution or dispersion at which the net charge on the macromolecules or colloidal particles is zero. At pH above the isoelectric

point of the support, cations will be adsorbed because the surface carries a negative charge. Below the *IEP*, only anions will be adsorbed because the surface is positively charged. The surface of a support in the initial stage of adsorption acts like a capacitor plate on which the ions stick. Consequently, the metal loading on ion-exchange catalysts depends on the properties of the support, as well as the metal salt concentration. In many cases, this technique is limited to catalysts with relatively low metal loading, as well as to certain pairs of metal salt-support.

In practice, the methods of ion exchange and adsorption from solution are fairly simple. The support is agitated in the metal precursor solution at room temperature until equilibrium has been reached. After filtration, the support is washed with deionized water to remove excess solution, while the exchange ions remain attached to the surface of the support. The final filter cake is dried and calcined to produce the active metal crystallites.

Chang et al. [14] also prepared nickel catalysts on SiO_2-RHA using the ion exchange method. In Figure 2.5, a scanning electron micrograph of their catalyst is shown. From Figures 2.5a and b, one can notice the smooth and clean surface of SiO_2-RHA in comparison with the surface of SiO_2-gel, which is another catalytic support. Figures 2.5c and d show the surface of Ni/SiO_2-RHA catalysts after reduction. They reported that the metal crystals on the surface were relatively small at low nickel content as shown in Figure 2.5c. The size distribution of the crystallites was quite uniform, but an average diameter was not reported. At higher nickel content, as shown in Figure 2.5d, the entire surface of the support was covered with crystallites. A uniform size distribution was reported, but an average crystallite size was not included in their results.

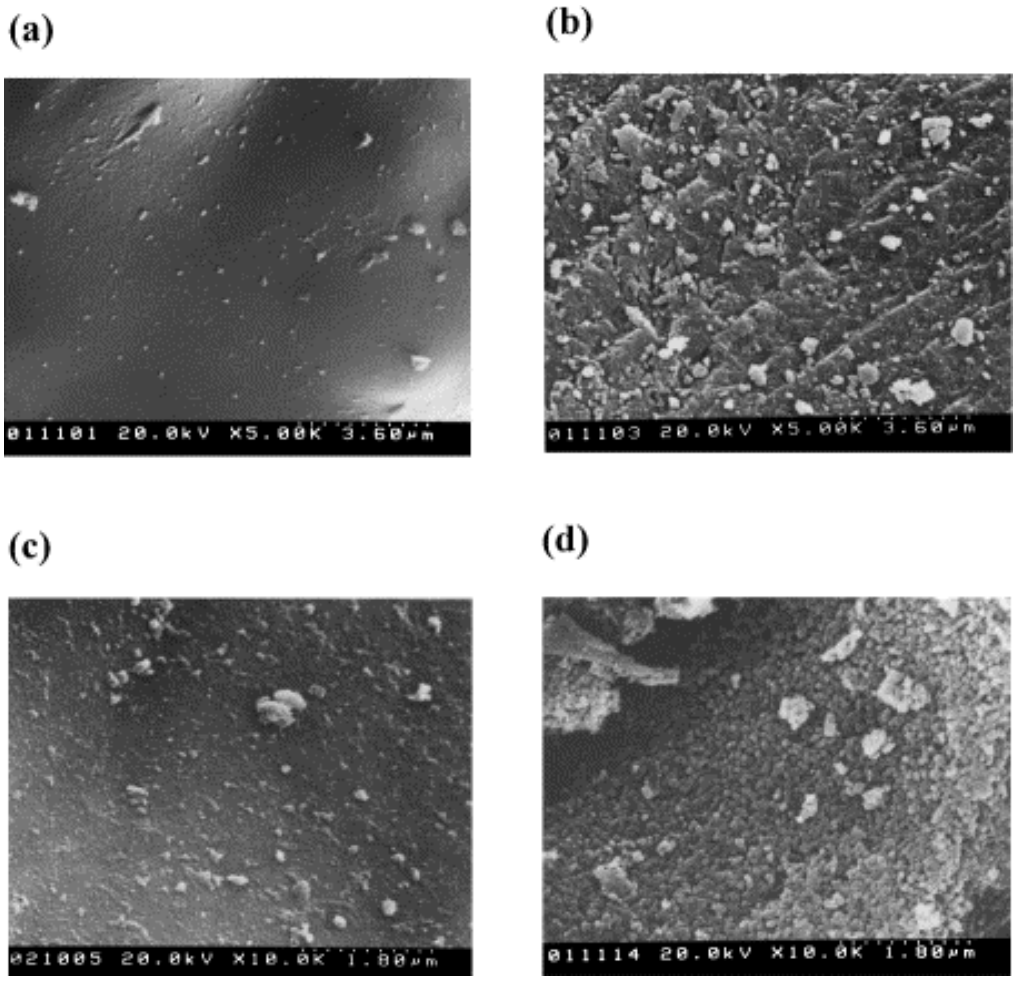

Figure 2.5 SEM images of SiO_2-RHA and catalysts prepared by ion exchange. (a) SiO_2-RHA (5 K X); (b) SiO_2-gel (5 K X); (c) 4.29 wt. % Ni/ SiO_2-RHA after reduction (10 K X); (d) 19.2 wt % Ni/ SiO_2-RHA after reduction (10 K X) [14].

C. Deposition-Precipitation and Co-Precipitation

Other forms of catalyst preparation that are limited to the base metals of Groups II-VIII are known as deposition-precipitation and co-precipitation. In deposition-precipitation, the support is suspended in the precursor solution, and the metal ion is deposited as a solid on the surface of the support. In contrast to ion exchange, a slow and homogeneous increase in OH^- at the support surface is required to carry out deposition precipitation. Often, the hydrolysis of urea under controlled-pH conditions provides the source of the hydroxide ions.

Figure 2.6 is an image of Ni/SiO_2-RHA catalyst precursors prepared by Chang et al. [15] using the deposition-precipitation technique. In Figure 2.6a, one can notice the smooth surface of the SiO_2-RHA support. Figures 2.6 b and c display the surface of the support after deposition-precipitation. The surface is covered with a layer of Ni compounds having a sheet-like structure. They later concluded that the metal support interaction between Ni and rice husk ash results in the nucleation of nickel hydrosilicate on the surface of the support during deposition-precipitation. The surface profiles of the catalysts after calcination are presented in Figures d and e. By comparing profiles before and after calcinations, it was found that the layer decomposed to form a network structure. The meshes of the network were found to be denser on the surface of the reduced Ni/SiO_2-RHA (Figure 2.6f) than those before reduction. Using temperature-programmed desorption (TPD), they found that at high nickel loading, the adsorption of Ni ions on the support results in the formation of multilayers. The nickel ions in the outer layer cannot make contact with the support and remains in the hydroxide form. The nickel hydroxide decomposes to nickel oxide during the calcination process. Their work

also showed that rice husk ash was preferable over silica gel as a catalyst support due to the higher conversion, yield, and selectivity of Ni/SiO_2-RHA in the hydrogenation of CO_2.

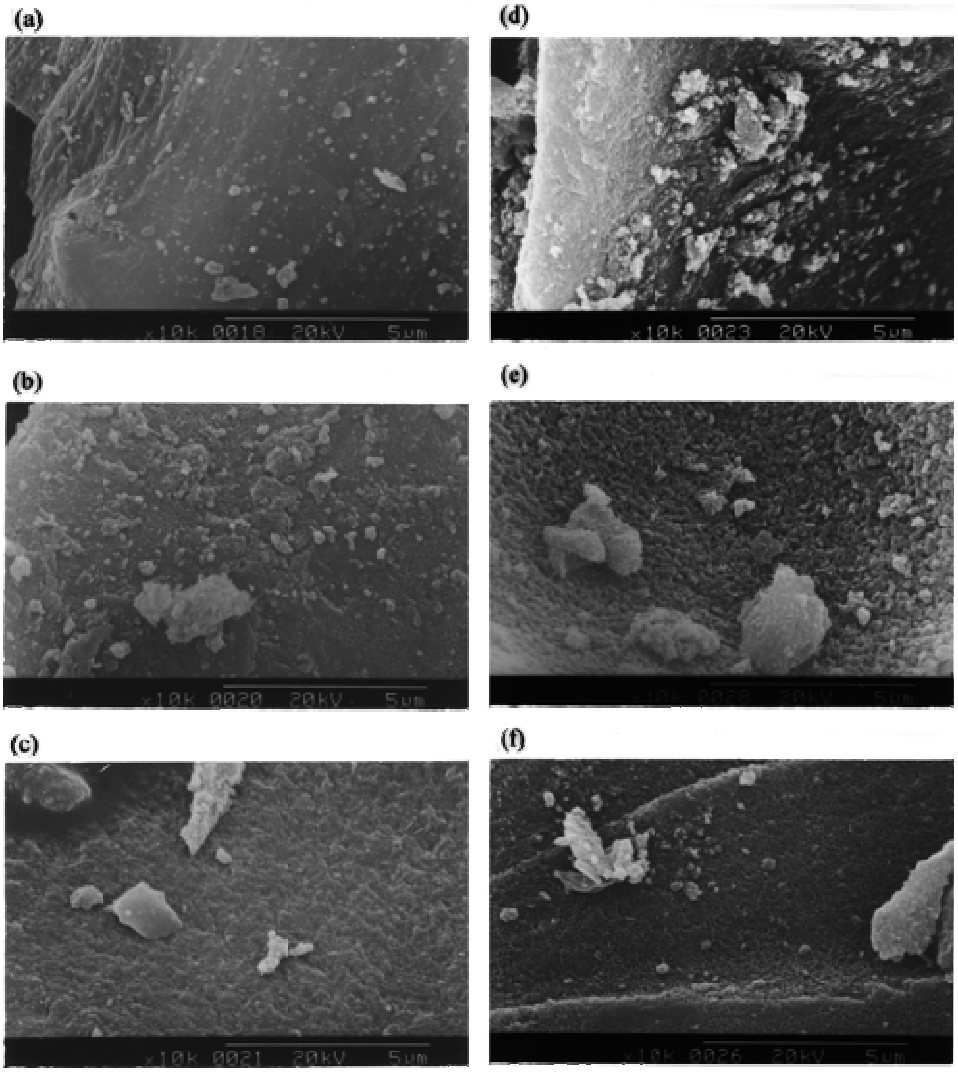

Figure 2.6 Scanning electron micrograph of specimen. (a) SiO_2-RHA (10 K X); (b) Ni/SiO_2-RHA (10 K X); (c) Ni/SiO_2 gel after precipitation (10 K X); (d) Ni/SiO_2-RHA after calcinations (10 K X); (e) Ni/SiO_2 gel after calcinations (10 K X); (f) Ni/SiO_2-RHA after being reduced and passivated (10 K X) [15].

Co-precipitation differs from other catalyst preparation methods because it does not begin with a preformed support. Alternatively, precursors to the support and the metal are precipitated simultaneously. For example, from a solution of $Ni(NO_3)_2$ and $Al(NO_3)_3$, a binary hydroxide can be obtained. After calcination and reduction, a nickel/alumina catalyst is formed [1].

In summary, traditional catalyst preparation techniques provide varying degrees of metal dispersion on catalytic supports. Impregnation due to incipient wetness often leads to poor dispersions. On the other hand, the ion exchange method frequently yields high and homogeneous dispersions, but the metal content of these catalysts are low. Deposition-precipitation of metal precursors on supports is recognized to yield high and homogeneous dispersions, even at high metal content. In all three preparation methods, the agglomeration of particles into meshy network structures has been observed.

The main focus of the research of Chang et al. [12, 14-15] was to use rice husk ash, which is a predominant by-product in the milling process of domestic agriculture, as a commercial catalyst support in order to reduce environmental pollution produced when the substance is discarded. Likewise, in the past, the focus of commercial catalyst preparation has primarily been the use of the before-mentioned preparation techniques to prepare high-performance catalysts. However, in recent years, many catalysis researchers have been investigating new catalyst preparation methods that result in the formation of mono-dispersed catalysts. The preparation of mono-dispersed catalysts is important in ascertaining the role of metal crystallite size in catalytic activity. The traditional techniques do not provide an adequate means of controlling the size of the active metal crystallites. Therefore, the focus of many catalysis researchers has shifted to

developing model catalysts that can be used to investigate structure-reactivity relationships using demanding and facile reactions.

2.2 EMULSIONS IN CATALYSIS

The preparation of colloidal metal particles has been studied extensively in the early history of colloidal science because of their unique properties, such as quantum size, surface, and interfacial effects. Because of the wide potential use of these colloidal metal particles in a number of industries, much work in the field has been concentrated on the preparation of small particles of platinum, iron, nickel, and cobalt metals. Because the preparation of small catalytic particles is important in catalysis, these colloidal metal particles have received considerable attention in the field of catalysis in recent years. Among the metals listed previously, nickel-based catalysts are of great interest because of their low cost and relatively high activity. Using emulsions, researchers have been able to find methods of preparing catalytic particles that coincide with the following guidelines:

1) The particles should be uniform in size and shape.
2) The particles should be adsorbed onto the support in a uniform way without clumping.
3) The adsorption onto the support should be performed in such a way that the catalyst particles are readily available to the reactants [16].

2.2.1 Basics of Emulsions

An emulsion is defined as a stable dispersion of droplets of liquid of a certain size within a second, immiscible liquid [17]. The dispersed liquid droplets are known as micelles. Emulsions can be distinguished between three different categories based upon the particle size: macroemulsions, miniemulsions, and microemulsions. Macroemulsions

are opaque emulsions with particles greater than 400 nm (diameter) in size. Miniemulsions are blue-whitish solutions, with particle sizes between 100-400 nm. Lastly, microemulsions are thermodynamically stable and optically isotropic solutions having particles with diameters ranging from 10-100 nm or less.

Over the years, research involving the preparation of metal particles 20 nm or less in size has used microemulsions due to their stability, small micelle size, and uniform particle distribution [3]. Therefore, nanoparticle size and shape can be better controlled using microemulsions as compared to the other methods of catalyst preparation discussed in Section 2.1.5. In particular, since metal salts are commonly soluble in water, water-in-oil microemulsions are employed to prepare nano-scale metal particles. The basic chemistry governing microemulsion formation from two immiscible liquids, commonly known as water and oil, is summarized in the following sections.

A. The Role of Surfactant

For the suspension of one immiscible liquid into another, a surfactant (or emulsifying agent) must be added to stabilize the solution. The surfactant stabilizes the system by adsorbing at the liquid-liquid interface as an interfacial film. The interfacial film has two roles: (1) It reduces the interfacial tension between the two immiscible liquids and thus reduces the thermodynamic instability of the system resulting from the increased interfacial area in the emulsion, and (2) The interfacial film also decreases the rate of coalescence of the dispersed liquid droplets by forming mechanical, steric, and/or electrical barriers around them [16]. Figure 2.7 shows a general schematic of the role of surfactant in producing an emulsion containing liquid droplets.

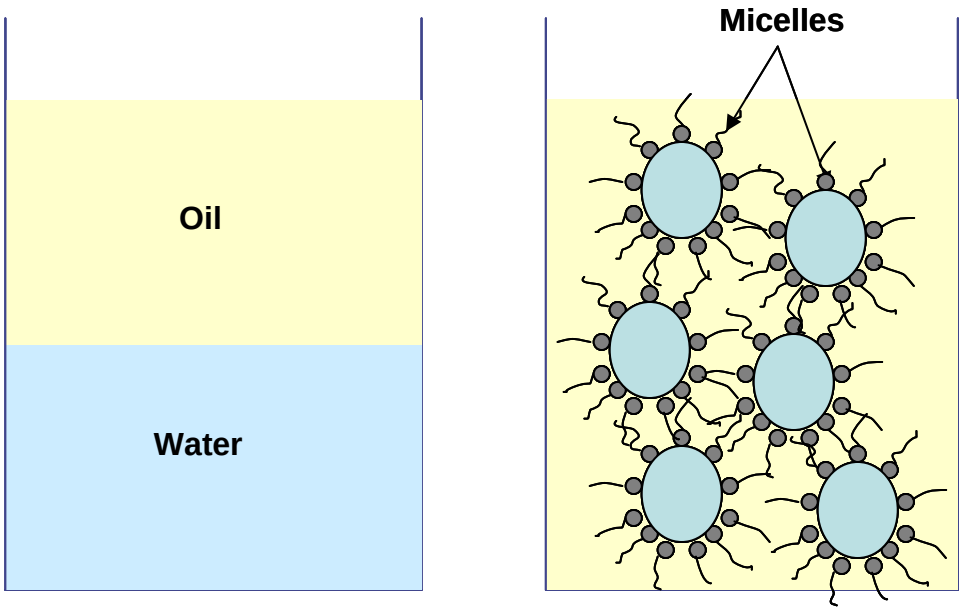

Figure 2.7 Schematic showing a) two immiscible liquids forming separate layers and b) formation of micelles upon the addition of surfactant in *W/O* emulsion.

B. *O/W* and *W/O* Emulsions

When referring to the nature of the dispersed and continuous phases in emulsions, the solutions can be categorized into either oil-in-water (*O/W*) or water-in-oil (*W/O*) emulsions. *O/W* emulsions are created when the surfactant is more soluble in the water phase than in the oil. *W/O* emulsions are produced when the emulsifying agent is more soluble in the oil than in water. In *W/O* microemulsions, the hydrophobic end of the surfactant molecule, the "tail", aligns toward the continuum oil phase, while the hydrophilic end, "the head", aligns toward the water droplets [17]. The reverse micelles created within *W/O* microemulsions can be 50 nm or smaller in diameter size. Figure 2.8 is a diagram of a reverse micelle within a *W/O* microemulsion.

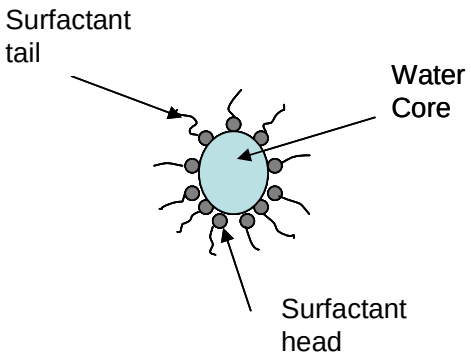

Figure 2.8 Components of a reverse micelle within a *W/O* microemulsion.

2.2.2 Preparation of Metal Particles

In the preparation of nano-sized metal particles, metal salts are dissolved in the aqueous phase in reverse micelles dispersed within the microemulsion. After adsorbing onto a support, the reverse micelles are calcined and reduced to produce nano-sized metal crystallites. The following sections give background information on the chosen microemulsion system and summarize the factors that affect the metal crystallite size and distribution.

A. Water-CTAB-Hexanol System

The three phase system of hexanol-CTAB (cetyltrimethylammonium bromide)-water has been thoroughly investigated by Ekwall et al. [18] and Ahmad et al. [19], and the phase equilibria of the system were determined through experimental procedures such as microscopy, phase centrifugation, and X-ray diffraction. The following figure shows the phase diagram for the water-CTAB-hexanol system.

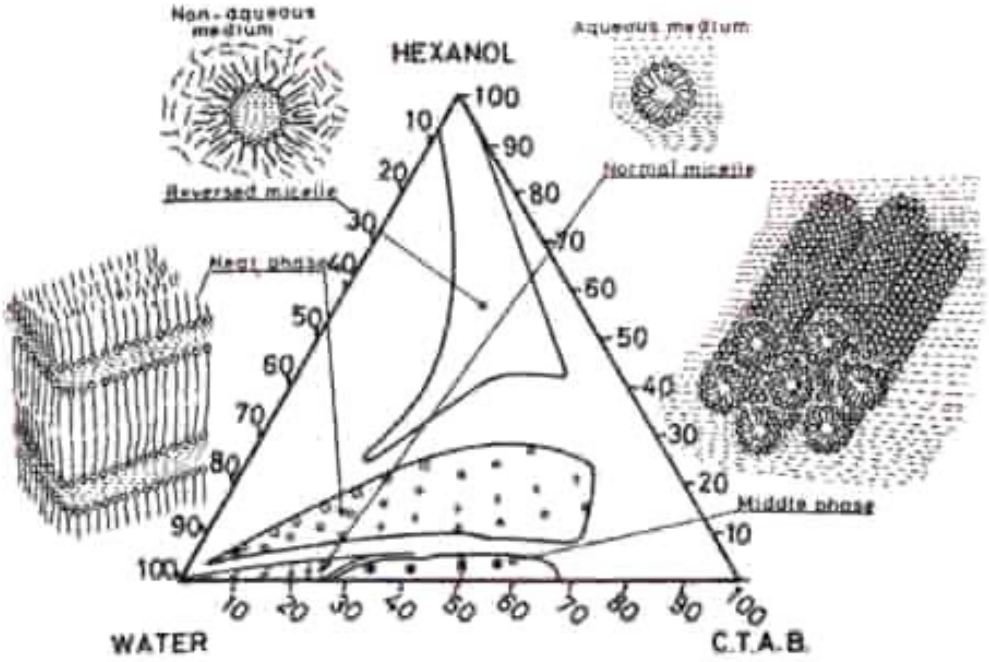

Figure 2.9 Phase diagram for the water-CTAB-hexanol system [19].

The compositions of each component needed to form reverse micelles can easily be determined using the phase diagram. Referring to Figure 2.9, the non-aqueous regime of the phase diagram is where reverse micelles are formed, and the phase diagram provides the compositions of the water-CTAB-hexanol system that fall under the reverse micelle region. Houyi et al. [20] also utilized the water-CTAB-hexanol system to prepare mono-dispersed nickel and cobalt boride catalysts using reverse micelles.

Besides the reverse micelle regime, several other phases can exist for the hexanol-CTAB-water system. The normal regime refers to the region where an *O/W* microemulsion exists at low hexanol concentrations. Basically, a homogeneous isotropic hexanolic solution is present in the corresponding portion of the phase diagram. The neat phase is a mesophase that has a typical lamellar structure with coherent layers of

surfactant molecules alternating with water layers. The middle phase consists of a homogeneous two-dimensional hexagonal mesophase in which rods of surfactant composed of CTAB ions orientate with the hydrocarbon tails inward, forming semi-liquid hydrocarbon cores, with the hydrophilic groups facing outwards towards the water. Because these different phases of the hexanol-CTAB-water system can be created, one has to use the phase diagram to ensure that they are working within their region of interest.

B. Factors Affecting Nanoparticle Size and Distribution

When using microemulsions to prepare nano-sized metal particles, researchers have discovered several factors that affect the particle size and size distribution. While preparing nanometer-sized Cu-Zn/Al_2O_3, Hu et. al. [21] concluded that the main factors affecting particle size were the following: 1) sol preparation and phase transfer, 2) removal of water and solvent, and 3) drying and calcinations. They also determined that the lowest limit of the particle size is decided by the size of single sol particles. That is, preventing micelles from aggregating into larger droplets will result in small particle formation and a more uniform particle distribution. Usually, a high amount of surfactant is used to reduce the interfacial tension of the micelles, which in turn prevents particle aggregation.

The size of metal particles formed using microemulsions can also be altered by varying the water to surfactant ratio, W_o. Barnickel et al. [2, 22] formed silver particles of different diameters by varying the micelle size of the microemulsion, which is dependent on W_o. The silver particles had an average diameter of 8.8 nm, with a standard

deviation of 3.4 nm. They assumed that primary reduction within micelles is confined to the dimensions of the droplets. Thus, one would expect larger micelles to produce larger particles and smaller micelles to produce particles of lower dimensions. Furthermore, previous work done by Qiu et al. [3] has shown that nanoparticles possess good monodispersity at lower W_o values at around 5 or 10, but at higher W_o the particles are characterized by a broad size distribution.

Likewise, Qiu et al. [3] determined that the size and polydispersity of Cu nanoparticles were greatly affected by the concentration of precursor salt. Their work stated that the process of particle formation from dissolved ions can be represented in the following order: ions-monomers-nuclei-particles. When the ion occupancy number in a water core is greater than the critical number of monomers, N_c, a stable nucleus must be formed. The nucleus then grows by incorporating ions and monomers into previously formed nuclei or particles to form larger particles. If growth occurs through intramicellar interaction, the particle size can be controlled by the inner core. Alternatively, through intermicellar interactions, the particle size may be greater than the diameter of the water core.

At high values of W_o ranging from 15 to 40, Qiu et al. [3] noticed that their particles were characterized by a broad size distribution in the range of 24-43 nm. They believe that the broad size distribution is a result of the aggregation of nuclei and primary particles via intermicellar interaction. Ultimately, taking heed to the results of the research discussed above, the research presented here attempts to fine tune the metal particle size by the varying the concentration of the precursor salt, after finding an optimal value of W_o that would lead to micelles with lowest polydispersity.

2.3 CATALYTIC REACTIONS

Supported metal catalysts generally have a strong tendency for the chemisorption of hydrogen, oxygen, carbon monoxide, and light hydrocarbons. Therefore, they are often used in catalytic reactions involving such reactants. These heterogeneously catalyzed reactions can be split into two major categories: structure-sensitive (demanding) and structure-insensitive (facile) reactions [4]. The following sections introduce two examples of structure-sensitive and insensitive catalytic reactions.

2.3-1 Ethane Hydrogenolysis

Ethane hydrogenolysis is an example of a very structure-sensitive reaction. The activity of a metal catalyst for this reaction depends heavily on the spacial coordination of the surface metal atoms [23]. Hydrogenolysis is sensitive to the availability of sites and the ensemble structure of metal atoms. The ensemble structure itself is sensitive to the spacing between the metal atoms (dispersion), the extent of crystal defects, and the presence of other metal types. The overall reaction is represented as follows:

$$C_2H_6 + H_2 \rightarrow 2CH_4 \qquad (2.1)$$

Using ethane hydrogenolysis as a test reaction, significant research has been done to elucidate the effects of nickel crystallite size on the catalytic activity of nickel supported on various supports [7-11, 24]. Varying the nickel crystallite size by sintering in H_2 at different temperatures, Carter et al. [7] found that the catalytic activity of the nickel catalyst supported on SiO_2-Al_2O_3 decreased with increasing crystallite size to a

larger extent than could be accounted for by the corresponding decrease in nickel surface area. Later, using model Ni catalysts composed of metal clusters supported on metal oxide thin films, St. Clair and Goodman [8] determined that the Ni activity increased with particle size up to a maximum of 2.5 nm, and a decrease in activity was noticed with increasing particle size. At particles greater than 4.0 nm, a constant activity was reached. Figure 2.10 shows the formation rate of ethane hydrogenolysis over model and conventional Ni/SiO_2. As one can see, the structure-sensitivity over both model and commercial catalysts is quite clear.

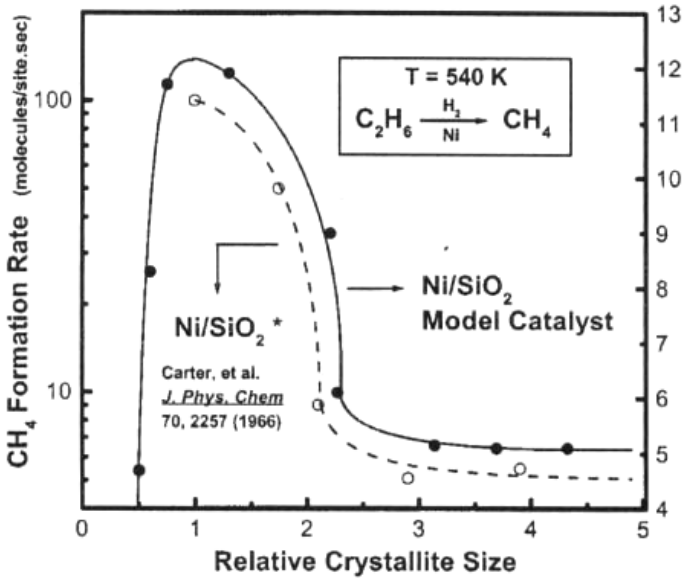

Figure 2.10 CH_4 formation rate from ethane hydrogenolysis over model and conventional Ni/SiO_2 catalysts. Data from Carter et. al. [7] is included [8].

Additionally, Rainer et al. [9] noticed a similar trend when using planar model oxide-supported catalysts to investigate intrinsic particle size effects and metal support interactions beyond the scope of single crystal studies. In Figure 2.11, the correlation between activity data acquired for single Ni crystals with those from supported catalysts are plotted in Arrhenius form.

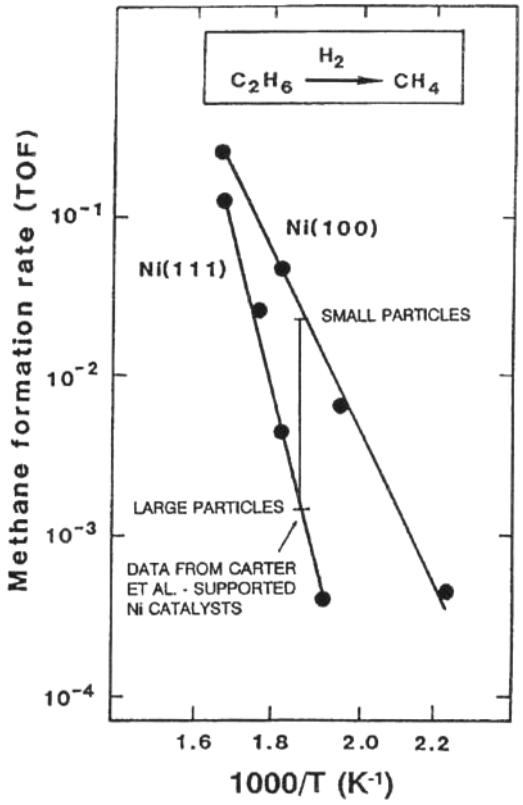

Figure 2.11 Arrhenius plots for the hydrogenolysis of ethane over Ni(100) and Ni(111) surfaces for a total reactant pressure of 100 torr and an H_2:C_2H_6 ratio of 100:1 [9]. Data from Carter et. al. [7] for supported Ni catalysts also included.

Referring to the figure directly above, one can see that smaller Ni particles display activities similar to the Ni(100) surface, while larger crystallites demonstrate the activity

of the Ni(111) surface. The activation energy of 24 kcal/mol displayed by the (100) surface is significantly lower than that associated with the (111) surface, implying a different reaction mechanism for the two planes.

Furthermore, Rainer et al. [9] also used the activity data given in Figure 2.11 to calculate theoretical activities as a function of particle size and R, which is the ratio of Ni(100) surface area to Ni(111) surface area. These results are shown in Figure 2.12.

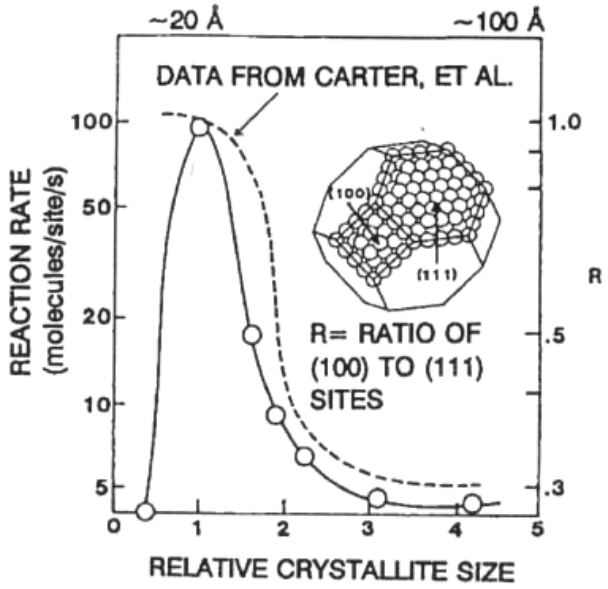

Figure 2.12 Calculated activities for a hypothetical supported catalyst consisting of regular polyhedra fully comprised of (100) and (111) facets, based on the single crystal data presented in Figure 2.10 [9]. The dashed line represents activity data for supported Ni catalysts taken from Carter et al. [7].

As one can see, the theoretical activity based upon single crystal studies agrees well with the data collected by Carter et al. for high surface area Ni catalysts. These trends suggest that the size dependence for ethane hydrogenolysis over supported Ni catalysts is closely

related to the relative percentages of (100) and (111) facets comprising the crystallite surfaces.

Additionally, Coulter et al. [10] discovered the same trend in particle size effects on catalytic activity for ethane hydrogenolysis at several reaction temperatures. Figure 2.13 shows the specific reaction rate or turnover frequency (*TOF*) for methane formation at different temperatures as a function of particle size.

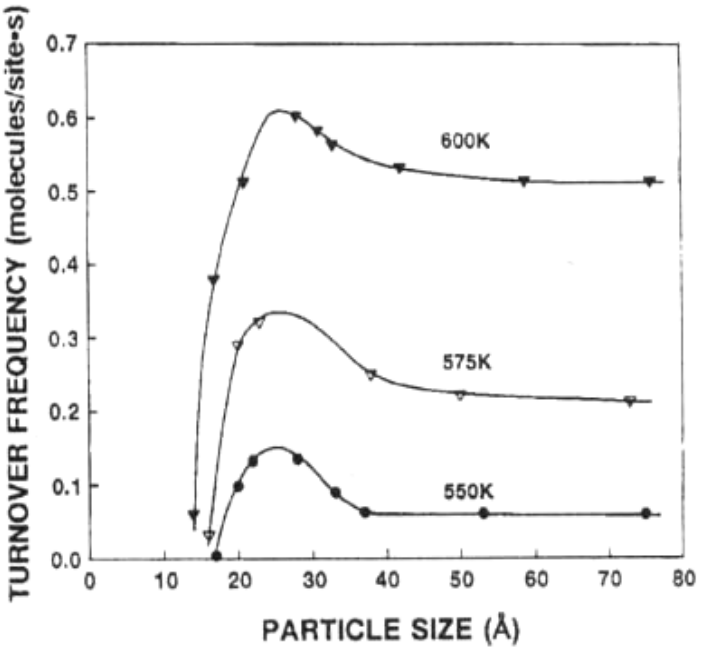

Figure 2.13 Ethane hydrogenolysis turnover frequencies at various temperatures (550, 575, 600 K) as a function of nickel particle size. P_{ethane}=1.0 Torr, P_{H2}=20 Torr, and t=10 min. [10].

In agreement with the previous research presented, the activity initially increases with particle size to a maximum of 2.5 nm. At particle sizes larger than 2.5 nm, the rate decreases to a constant value independent of particle size.

In addition to the variation of the turnover frequency with particle size, Coulter et. al. [10] also noted that the apparent activation energy was found to vary with particle size as well. In Figure 2.14, the activation energy for ethane hydrogenolysis as a function of particle size is shown.

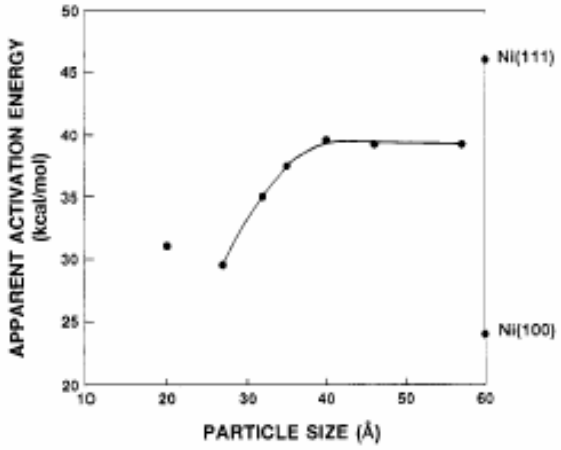

Figure 2.14 Activation energy for ethane hydrogenolysis as a function of particle size. Activation energies were calculated from the data in Figure 2.13 [10].

The lowest apparent activation energy (30 kcal/mol) for ethane hydrogenolysis on 2.5 nm particles is similar to the reported value on Ni(100), which is 24 kcal/mol. The apparent activation energy then increases from a low of 30 kcal/mol for the 2.5 nm particles to a high of approximately 40 kcal/mol for the larger particles. The activation energy for the larger particles is similar to the value associated with that of the Ni(111) surface, which is 46 kcal/mol.

Lastly, infrared reflection absorption spectroscopy (IRAS) was used to investigate the surface structure of nickel particles [11, 24]. Infrared spectroscopy is well-suited for

the characterization of adsorbents and eventual products of a catalytic reaction on mono-dispersed clusters. From studies of how mono-dispersed nickel clusters interact with carbon monoxide (CO), one can compare data obtained from IRAS spectra with surface science studies on single crystals and larger-sized nickel particles to determine if an intrinsic particle size effect is present.

Figure 2.15 shows the correlation between the *TOF* for ethane hydrogenolysis and the percentage of total bridged bound CO obtained from IRAS spectra data.

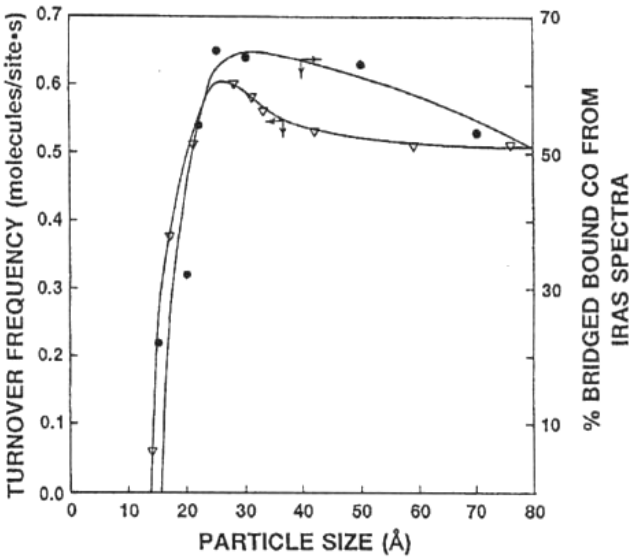

Figure 2.15 Correlation between the TOF for ethane hydrogenolysis (reaction conditions same as in Figure 2.12, 600 K) and the percentage of total bridge bound CO from IRAS spectra [11].

As one can see, ethane hydrogenolysis reactivity parallels the relative intensity change of the bridge-bound CO on the small particles. As shown in Figure 2.15, the percentage of bridging CO increases with particle size to a maximum of about 2.5 nm and then

decreases. Coulter et al. [11] states that the agreement between these data indicates a similarity in the nature of bridging CO adsorption and ethane hydrogenolysis. Both mechanisms require at least two metal atoms.

The distance between and the orientation of the surface Ni atoms have been proposed to give rise to the kinetic differences observed for hydrogenolysis over the Ni(100) and Ni(111) faces. The more open Ni(100) surface exhibits a mechanism for ethane hydrogenolysis that is comparable to the steps observed for CO methanation, which is a reaction insensitive to structure. It has been proposed that the Ni-Ni distance on the (100) surface facilitates an easy C-C bond scission for the adsorbed ethane [25]. This results in the hydrogenation of the carbonaceous deposits, and the overall apparent activation energy (24 kcal/mol) is very similar to the activation energy of CO methanation, which is reported to be 25 kcal/mol [26].

In summary, two factors may contribute to the activity for ethane hydrogenolysis: an intrinsic size effect for small clusters and a change of surface structure for the larger particles. Referring to Figure 2.15, the initial increase in activity for ethane hydrogenolysis and a similar increase in the percentage of bridging CO adsorption suggest an intrinsic particle size effect. The supported nickel particles must be a certain size in order to exhibit the necessary chemical properties for higher activity. A component of the size effect may be due to metal-support interactions. The smaller the metal particles, the higher the fraction of total atoms contacting the support surface. Therefore, for smaller particles, the effects of metal-support interactions could be significant. The effects of MSI would decrease as the particle size increases because a

lower fraction of the total atoms would be in contact with the support. This may result in the constant activity value observed for particle sizes of 4.0 nm or greater.

2.3-2 Ethylene Hydrogenation

Ethylene hydrogenation represents an example of a reaction that is relatively insensitive to metal catalyst structure [27, 28]. The activity of the metal catalyst used in this reaction is not affected by the orientation of the surface metal atoms and thus the particle size. The hydrogenation reaction, also known as catalytic reforming, proceeds on a single site of the metal atom and is thus insensitive to structure perturbations [27]. This chemical reaction proceeds in the following manner:

$$C_2H_4 + H_2 \rightarrow C_2H_6 \qquad (2.2)$$

Ethylene hydrogenation has been widely used as a test reaction in the investigations of structure sensitivity and insensitivity in catalytic reactions [27, 28]. Shaikhutdinov et al. [27] investigated the structure-reactivity relationships of palladium catalysts deposited on a thin, well-ordered alumina film grown on a NiAl(110) crystal. They designated this catalyst as $Pd/Al_2O_3/NiAl(110)$. Using this supported metal model catalyst, the adsorption and co-adsorption of ethylene (C_2H_4, C_2D_4) and hydrogen (D_2) on Pd particles were studied by temperature-programmed desorption (TPD). They reported two primary modes of ethylene adsorption on Pd: (i) weak bonds attributed to π-bonding, and (ii) strong di-σ-ethylene bonding. Figure 2.16 shows the structure of the different

reaction intermediates that can be observed on the Pd surface during ethylene hydrogenation.

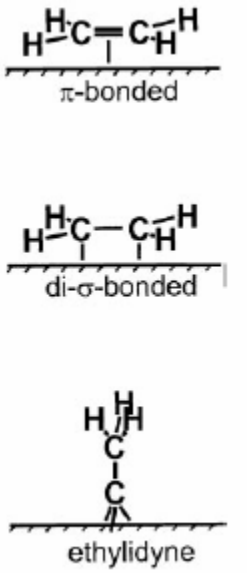

Figure 2.16 Different reaction intermediates that can be adsorbed on Pd particles during ethylene hydrogenation [27].

Additionally, Shaikhutdinov et al. [27] noticed that hydrogen atoms adsorb more strongly on the surface of smaller particles, while binding in subsurface sites is less strong and only weakly dependent on particle size. Hydrogen pre-adsorption shifts the distribution of ethylene states toward the weakly bound π-state, while adsorbed ethylene blocks the hydrogen adsorption. Upon co-adsorption, ethane is produced by the reaction of the π-bonded ethylene with those hydrogen atoms residing in the most weakly bound states. Therefore, as shown in Figure 2.17, ethylene hydrogenation activity of Pd is independent of particles size in the 1-3 nm range. This is the small particle range where

hydrogen adsorbs more strongly, and H_2 pre-adsorption promotes the formation of the π-state intermediate.

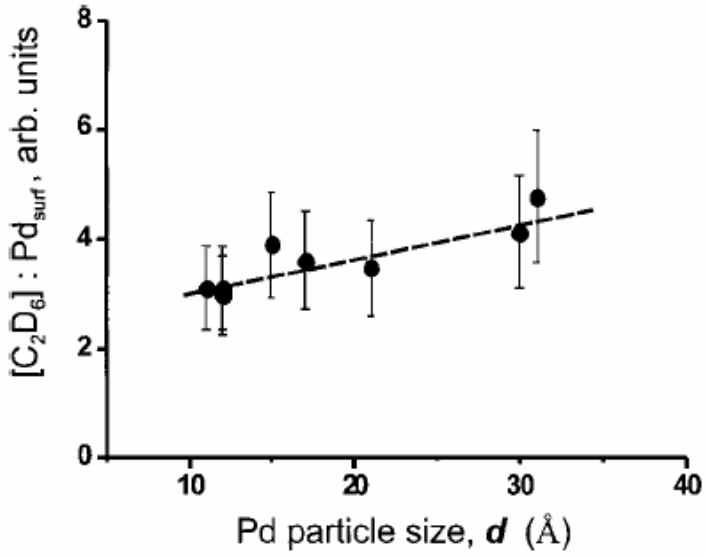

Figure 2.17 Integral TPD signal of ethane per Pd unit surface area as a function of particle size measured after identical co-adsorption conditions [27].

McCrea et al. [28] used the (111) and (100) crystal faces of platinum to monitor the rates of ethylene hydrogenation. They also used sum frequency generation (SFG) vibrational spectroscopy to monitor the surface species, some of which were the surface reaction intermediates displayed in Figure 2.16. They found that strongly bound ethylidyne and di-σ-bonded ethylene were not the active species which turnover during ethylene hydrogenation. Both ethylidyne and di-σ-bonded ethylene were present on both Pt(111) and Pt(100) under reaction conditions, although the ratio of the concentrations of the species was different. The reaction rate was found to be 11±1 and 12±1 molecules per site per second for Pt(111) and Pt(100), respectively, thereby, indicating the reaction

is structure-insensitive. Since the *TOF* was essentially the same on the two surfaces, McCrea et al. concluded that while the concentration of ethylidyne and di-σ-bonded ethylene are different, these species must not be the active ones directly participating in ethylene hydrogenation. Thus, the most likely candidate for the turnover species is the π-bonded intermediates; the concentrations of these species could not be identified because they were near the limit of SFG.

As one can see, both ethane hydrogenolysis and ethylene hydrogenation are commonly used to study the activity of supported metal catalysts, especially when structure-reactivity relationships are the primary focus. Both of these reactions were used to study particle size effects on the catalytic activity of the mono-dispersed nickel catalyst prepared in this research. Reactions results will be compared to earlier findings, some of which are presented above.

2.4 RESEARCH OBJECTIVES

It is well established that most reactions fall into one of the two categories: (i) facile or structure-insensitive, and (ii) demanding or structure-sensitive. Metal crystallite size would thus be a major parameter affecting the intrinsic activity and selectivity of catalysts. Different reaction types, including hydrogenation and hydrogenolysis reactions, may require metal ensembles of different sizes. Traditionally prepared supported metal catalysts, such as impregnation and precipitation techniques, often have metal crystallites distributed over a broad range of sizes (2-50 nm). It is thus difficult to ascertain the role of metal crystallite size on the activity and selectivity in these catalysts. Therefore, the preparation of mono-dispersed supported catalysts promises to be an important first step in determining how metal crystallite size affects the yield of catalytic reactions.

In conjunction with previous research done to determine particle size effects on catalytic activity, the objective of this research is to prepare a set of several batches of supported nickel catalysts such that each batch has a very narrow size distribution. It is desired that the average size from one batch to another can be varied between 2 and 10 nm, by following a catalyst preparation protocol determined from experimentation. Therefore, the overall research approach involves the following: 1) developing protocol for the preparation of supported mono-dispersed catalysts, 2) characterizing the metal crystallite size distribution using scanning electron microscopy, and 3) studying reactivity of various crystallite sizes for the two reaction classes: hydrogenation and hydrogenolysis.

CHAPTER 3

EXPERIMENTAL METHODS

This chapter outlines the experimental methods used in the preparation of mono-dispersed supported Ni catalysts. First, procedures used to prepare microemulsions and characterize the size and size distribution of reverse micelles will be presented. Second, the task of characterizing Ni crystallites using scanning electron microscopy (SEM) and energy dispersive X-ray microanalysis (EDS) will be introduced. The challenges encountered while trying to obtain satisfactory SEM and EDS results will be discussed. Lastly, the reactor setup used to run ethane hydrogenolysis and ethylene hydrogenation reactions is presented, along with the methods used to fine-tune the setup and determine optimal parameters for each reaction.

3.1 MICROEMULSION PREPARATION AND CHARACTERIZATION

3.1.1 Preparation Techniques

Microemulsion components hexanol, nickel chloride, and cetyltrimethylammonium bromide (CTAB) were obtained from Aldrich© chemicals. These chemicals were used as purchased. An aqueous solution of 0.1 M nickel chloride was prepared by dissolving the appropriate amount of $NiCl_2$ in a corresponding quantity of distilled water. Using a heating mantle, the solution was slightly heated to promote the dissolution of $NiCl_2$. Referring to Table 3.1, twelve samples were prepared. The quantities used for each component in the samples are given in Table 3.1. Samples 1-6 were prepared with the oil-to-aqueous phase molar ratio (*O/A*) fixed at 2, while the water-

to-surfactant molar ratio, W_o, was varied between 5 and 30. Samples 7-12 were made at O/A=5, and W_o was varied over the same range. All sample compositions were found to fall in the reverse micelle region of the phase diagram shown in Figure 2.9. It was expected that the microemulsions may become less stable at O/A = 5 because increasing the amount of oil in system moves the composition closer to the boundary of the reverse micelle regime. While varying W_o, the micelle size was expected to increase with W_o due to the presence of less surfactant in the system at higher values.

Table 3.1 Quantities used in microemulsion sample preparation.

O/A	Sample	W_o	Hexanol (mol)	Aqueous $NiCl_2$ (mol)	CTAB (mol)	Hexanol (ml)	Aqueous $NiCl_2$ (ml)	CTAB (g)
2	1	5	0.32	0.16	0.032	40	2.89	11.66
	2	10			0.016			5.83
	3	15			0.011			3.89
	4	20			0.0080			2.92
	5	25			0.0064			2.33
	6	30			0.0053			1.94
5	7	5	0.32	0.064	0.013	40	1.16	4.67
	8	10			0.0064			2.33
	9	15			0.0043			1.56
	10	20			0.0032			1.17
	11	25			0.0026			0.93
	12	30			0.0021			0.78

The desired amount of hexanol was poured into a 100 ml beaker. CTAB was added to the oil phase, and the solution was stirred until a white slurry formed. The solution was then placed on a magnetic stirrer, while the appropriate amount of aq. $NiCl_2$ was added in a drop-wise fashion using a glass pipette. After the addition of aq. $NiCl_2$,

the sample remained on the stirrer until the white slurry had become a transparent solution. The sample was then placed in an ice bath, and further agitation was applied using ultrasonication. The power level of the sonicator was kept constant at 70% for all samples, and the sonication time was 20 minutes. Previous research has shown that sonication of reverse micelles for 20 minutes resulted in a narrowing of the micelle size distribution [22]. During sonication, the samples were continually stirred so that the entire volume was in contact with the sonicator rod. Care was also taken to ensure that the rod of the sonicator was at a significant level below the surface of the sample. The purpose of these twelve trials shown in Table 3.1 was to choose a set of optimum values of *O/A* and W_o such that (i) the degree of polydispersity is lowest and the reverse micelle is in the range of interest for our studies and (ii) the emulsion and reverse micelles are stable.

Once the optimal values of *O/A* and W_o were determined using dynamic light scattering, another batch of microemulsions were prepared with the aqueous $NiCl_2$ concentration varied. The aqueous $NiCl_2$ concentration in the reverse micelles was varied between 0.1 and 0.001 M, with *O/A* and W_o being held constant at the optimal values. Table 3.2 lists the quantities of components used in the preparation of the aqueous $NiCl_2$ solutions. The aqueous $NiCl_2$ concentration within the reverse micelles was varied in order to determine any effects this may have on the size characteristics of the reverse micelles and the microemulsion stability. This information is important since one of our research goals is to vary the Ni crystallite size by changing the metal salt concentration. Also, the crystallite size can be calculated based upon the known aqueous $NiCl_2$ concentration and the reverse micelle size (see Appendix A.1).

Table 3.2 Quantities used in preparation of aqueous $NiCl_2$ solutions.

Concentration (M)	$NiCl_2$ (g)	H_20 (mL)
0.1	0.65	50
0.05	0.32	50
0.03	0.194	50
0.01	0.065	50
0.005	0.032	50
0.001	0.0065	50

3.1.2 Dynamic Light Scattering

The class of light scattering methods focusing on the time dependence of scattered light intensity is known as dynamic light scattering (DLS) [29]. Since the reverse micelles within the microemulsion are subjected to Brownian motion, if a laser beam is directed at the sample, the micelles in the sample will scatter light into a random pattern of varying size, shape, and intensity similar to that shown in Figure 3.1.

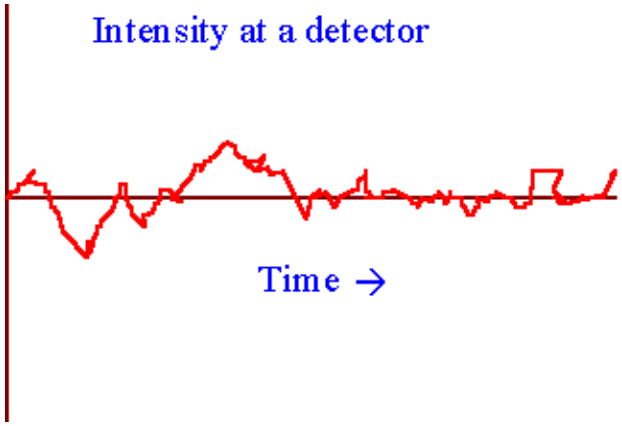

Figure 3.1 Example of scattered intensity vs. time measurement for DLS particle size determination [30].

The time variation of the scattered intensity is analyzed by examining its autocorrelation function, which is written in the following format:

$$C(\tau) = Ae^{-2\Gamma\tau} + B \tag{3.1}$$

where $C(\tau)$ is the autocorrelation function, τ is time, and A and B are constants [30]. For a monodispersed population of particle sizes, a unique autocorrelation function is produced consisting of a single exponential decay. Mixture of more than one size population produces a sum of exponentials. Figure 3.2 shows a graphical representation of a typical autocorrelation function.

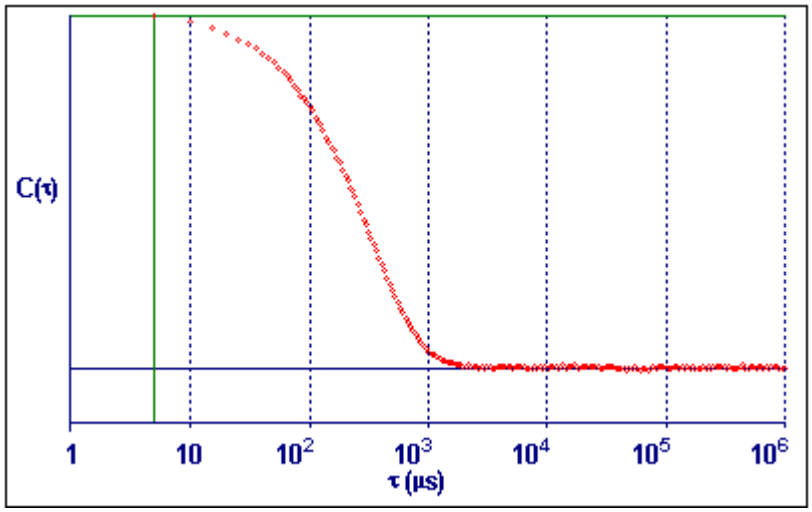

Figure 3.2 Graphical representation of a standard autocorrelation function [30].

Γ, the decay rate, is defined as follows:

$$\Gamma = q^2 D \tag{3.2}$$

where q is the scattering vector and D is the diffusion coefficient. They are defined in the following manner [30]:

$$q = \frac{4\pi n \sin(\theta/2)}{\lambda} \text{ and} \tag{3.3}$$

$$D = \frac{k_B T}{3\pi\eta d} \tag{3.4}$$

where n is the refractive index, θ is the scattering angle, λ is the laser wavelength, k_B is Boltzmann's constant, T is the temperature in Kelvin, η is the solvent viscosity, and d is the micelle diameter. Equation 3.4 is known as the Stokes-Einstein equation and can be used to calculate the micelle size once the diffusion coefficient and other pertinent system parameters are known.

3.1.3 DLS Sample Preparation and Testing

The DynaPro© Molecular Sizing Instrument with DYNAMICS© software was used to determine the size and size distribution of the reverse micelles in each microemulsion prepared. Figure 3.3 is an image of the DynaPro© light scattering device.

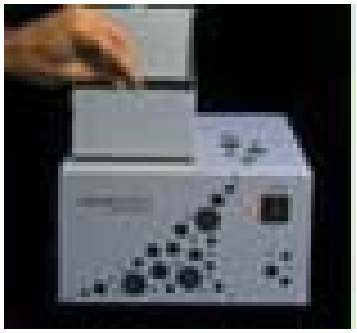

Figure 3.3 The DynaPro© Molecular Sizing Instrument [31].

Using glass pipettes, approximately 1 ml of each microemulsion sample was placed in a clear, four-sided polystyrene cuvette manufactured by Dynalon©. The cuvettes were rinsed with small portions of the sample before the 1 ml test volume was added. The cuvette, with sample volume, was then inserted into the light scattering instrument. For each sample, twenty measurements were taken with the autocorrelation function determined for each. At the conclusion of testing, an average micelle radius, distribution type, and polydispersity value was reported.

One major challenge during light scattering testing was preventing the presence of large sample impurities from affecting the micelle size results. Care was taken to ensure that the cuvettes were clean and as scratch-free as possible. Microemulsion samples were also carefully prepared in order to minimize the presence of impurities. However, the light scattering instrument frequently detected particles in the size range of 10^4 nm or higher. To ensure that these larger particles were simply sample impurities, distilled water was tested to see if any similar particles could be detected. Light scattering results showed that particles in the size of 10^4 nm were also detected in distilled water; thereby indicating that the larger particles detected in our emulsion samples were impurities and

could be discarded so that accurate micelle size results could be obtained. The reverse micelle diameter, in contrast, ranged between 25-264 nm.

3.1.4 Microemulsion Stability

The stability of a microemulsion can be determined by measuring its shelf life. As discussed in the Background, a stable microemulsion can be described as an isotropic, transparent homogeneous solution. Accordingly, the shelf life of an emulsion is defined as the time to visible phase separation [32]. After each microemulsion was prepared, the number of days in which no phase separation was detected was recorded. Furthermore, microemulsion samples were periodically tested using DLS to ensure that the micelle size characteristics did not change significantly over time. Figure 3.4 shows an example of a stable microemulsion, and one that is unstable as indicated by phase separation.

Figure 3.4 **Image showing phase separation in less than 24 hours for an unstable microemulsion (left) and homogeneity for over 3 months for a stable microemulsion (right).**

3.2 NICKEL CRYSTALLITE PREPARATION

After a preparation method for forming microemulsions with the micelle size of interest and lowest polydispersity was developed, nickel crystallite particles were prepared by evaporating the organic solvent, hexanol, and decomposing the surfactant, CTAB, after adsorption unto an inert support. The following sections outline the methodology used to form the nano-sized nickel particles.

3.2.1 Use of Supports

As discussed in Section 2.1.4, nano-sized metal particles are firmly attached to a catalytic support in order to reduce the particles' instability by preventing coalescence. In order to form stable nickel nano-particles, portions of the microemulsion samples were deposited on α-alumina (Aldrich©, 200-325 mesh, 99+%) and silica powder, granules, and plates. α-alumina was chosen because it is less porous than other alumina types. The absence of pores would simplify SEM analysis by making it easier to find the nickel nano-particles on the support surface. Ultimately, the type of supports used was determined by limitations of the SEM analysis and reactor setup. These limitations are discussed in Sections 3.3.1 and 3.3.2.

For deposition onto alumina plates, which were 1 cm x 1 cm (0.1 cm thick), approximately one drop of the microemulsion was positioned at the center of the plate. When using 2.5 cm x 2.5 cm silica plates (0.4 cm thick), drops were positioned at the corners and center of the plate. This method was utilized to eliminate the amount of void surface space, making the process of finding nickel particles easier when using SEM. When powder, granules, or pellets were used as supports, a pre-determined portion of the

microemulsion was deposited throughout the support material. The amount of microemulsion deposited onto the supports was dictated by the results from SEM characterization and the desired wt. % Ni catalyst to be formed. Initial SEM testing showed that particle aggregation became more prominent when higher Ni loadings were deposited on granular supports. This may be due to the presence of more particles coalescing during the calcination process. Therefore, the amount of emulsion used was minimized in order to prevent aggregation. After depositing emulsion on the support, the samples underwent drying and calcination in order to remove hexanol, CTAB, and other compounds not desirable in the final product.

3.2.2 Drying and Calcination

Once microemulsion drops were deposited on the alumina or silica supports, the samples were allowed to dry at room temperature for approximately 24 hours. Because of the small amounts of microemulsion deposited onto the support (i.e. 0.1 ml), this drying time and temperature was enough to allow the hexanol to evaporate, leaving residue of CTAB and nickel compound on the support surface. After hexanol removal, the samples were calcined in order to decompose the surfactant, CTAB and to remove any remaining hexanol and/or water. Calcination was carried out at 400˚C for 4 hours. Air at a flow rate of 10 ml/min was passed over the samples. Figure 3.5 shows the Thermolyne© 79300 tubular furnace used in the calcination step.

Figure 3.5 The Thermolyne© 79300 tubular furnace.

At the conclusion of the 4 hr. calcination period, the samples were allowed to cool to room temperature under He flowing at a rate of 10 ml/min. During the course of experimentation, the calcination temperature and time were varied in hopes of finding the optimal conditions that would prevent or significantly reduce particle aggregation due to surface migration. However, calcination temperatures less than 300 ˚C did not result in the complete decomposition of surfactant or other unwanted compounds. This was evident from the presence of a crystal-like substance, presumably due to the presence of surfactant. It also interfered with the SEM analysis, due to charging of the sample. Therefore, calcination for all catalyst samples was done at 400 ˚C for 4 hours.

3.3 NICKEL CRYSTALLITE CHARACTERIZATION

After the nickel nano-particles were formed, scanning electron microscopy, SEM, and energy dispersive X-ray microanalysis, EDS, were used to characterize the supported crystallites. SEM was used to obtain images of the nickel nano-particles at high magnifications so that the particle size distribution could be viewed, while EDS was used to confirm that the particles were indeed nickel. The following sections outline the operating principles of SEM and EDS, as well as outline the difficulties encountered during this stage of experimentation.

3.3.1 Scanning Electron Microscopy

Scanning electron microscopy (SEM) is one of the most versatile and well-known analytical techniques. Compared to conventional optical microscopy, an electron microscope offers many advantages including high magnification, large depth of focus, better resolution, and simplicity for sample preparation and observation. In this study, the LEO© 1530 field emission electron microscope (Figure 3.6) was used to obtain the images of supported nickel nano-particles.

Figure 3.6 The LEO 1530 Field Emission SEM.

When using SEM, electrons generated from an electron gun enter the surface of a sample and generate many low energy secondary electrons. The intensity of these secondary electrons is governed by the surface topography of the sample. Therefore, preparing a conductive sample is advantageous because this results in a high intensity of secondary electrons. Hence, an image of the sample surface is constructed by measuring secondary electron intensity as a function of the position of the scanning primary electron beam.

Though SEM sample preparation is relatively easy, the use of non-conductive supports made the task of gaining clear images at high magnifications challenging. As previously mentioned, conductive samples produce higher secondary electron intensity, and this in turn results in clearer images at higher magnifications. Alumina and silica, which were used to support the nickel nano-particles, are relatively non-conductive. When attaching deposited alumina and silica supports to the SEM sample plate with carbon tape, it was observed that clear images at higher magnifications were difficult to obtain. Therefore, the nickel nano-particles could not be observed due to a lack of image clarity at magnifications of 25 K and higher.

In order to obtain clear SEM images, several attempts were made to achieve a better conducting sample surface. Both gold and carbon coatings were used to increase sample conductivity. This method only slightly increased the quality of the micrographs at magnifications of 25 K and above due to the larger size of the nonconductive supports when compared to the thin coating layer. In order to make the deposited samples more conductive for SEM purposes, alumina particles, after undergoing the deposition, drying, and calcination stages, were pressed into indium foil. This sample preparation method

was successful in obtaining higher quality micrographs at magnifications of 25 K and higher. As a result, the nano-sized nickel particles could be characterized by visual analysis.

3.3.2 Energy Dispersive X-Ray Microanalysis

In addition to secondary electrons imaging, back-scattered electron imaging and energy dispersive X-ray (EDS) microanalysis are also useful tools widely used for chemical analysis. The intensity of backscattered electrons generated by electron bombardment can be correlated to the atomic number of the element within the sampling volume. Therefore, qualitative elemental information can be obtained. The characteristic X-rays emitted from the sample serve as fingerprints and give elemental information of the samples including semi-quantitative analysis, quantitative analysis, line profiling, and spatial distribution of elements. Figure 3.7 is a schematic diagram showing the construction of an EDS detector.

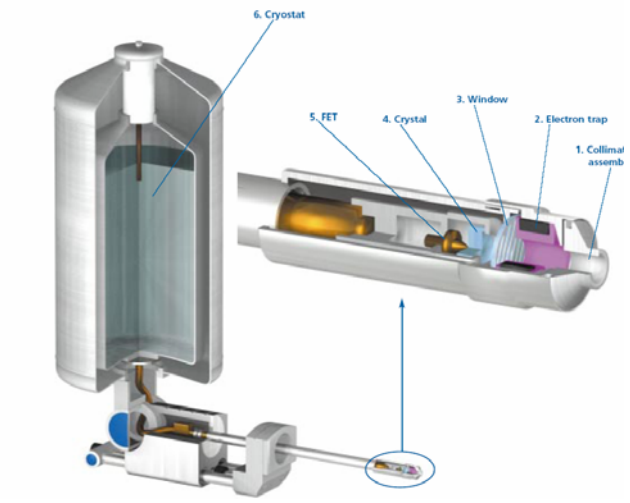

Figure 3.7 Cut-away diagram showing the construction of a typical EDS detector [33].

Referring to Figure 3.7, the X-ray detector detects and converts X-rays into electronic signals. The collimator provides a limiting aperture through which X-rays must pass to reach the detector. This ensures that only X-rays from the area of the sample being excited by the electron beam are detected, and stray X-rays from other parts of the microscope chamber are not included in the analysis. The electron trap is a pair of permanent magnets that strongly deflect any passing electrons

When using EDS, the resolution performance at low energies is critical to good performance for all elements. The identification and quantification of closely spaced X-ray peaks becomes easier and more accurate as the separation between them increases. At low energy levels, the X-ray lines get closer together. When small features less than one micron are being analyzed, the beam voltage needs to be reduced to avoid electron scattering outside the feature. However, at small kV only low energy lines are available for analysis. Thus, gaining both high-quality micrographs and accurate EDS analysis at low energy and high magnification was a challenge. For instance, when using a beam voltage of 3 kV, SEM images were of better resolution, but EDS analysis was difficult due to the close proximity of X-ray lines at the low energy level. As a result, most SEM and EDS analysis was done at a beam voltage of 5 kV because both SEM and EDS results were accurate at this value throughout a wide magnification range. However, at magnifications of 100K X and above, EDS analysis was not accurate due to lower resolution performance.

3.4 REACTOR STUDIES

As discussed in Section 2.3, ethylene hydrogenation and ethane hydrogenolysis reactions were conducted in a fixed bed reactor in order to determine the activity of the supported nickel catalyst. During initial reactor testing, a commercial Ni catalyst, Ni-0750, manufactured by Engelhard was used to fine-tune the reactor setup before using the emulsion-prepared catalysts. The following sections discuss the reactor setup, the conditions of the reaction trials, and the experimental challenges encountered.

3.4.1 Reactor Setup

A fixed bed packed reactor was used to conduct ethylene hydrogenation and ethane hydrogenolysis reactions. Figure 3.8 is a schematic of the reactor that was used during experimentation.

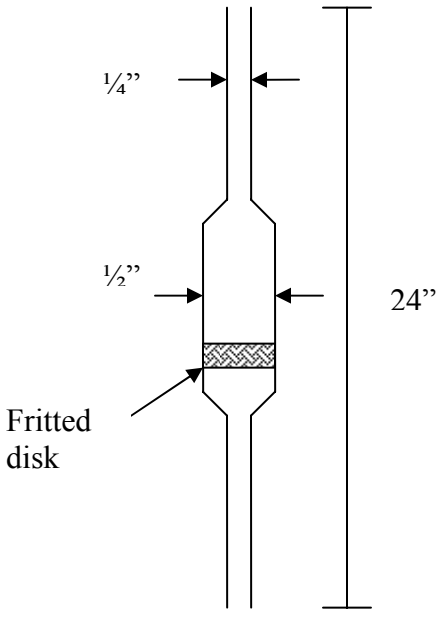

Figure 3.8 Schematic of fixed-bed reactor.

The reactors were composed of Pyrex, which can withstand temperatures up to 550 ˚C. The center of the reactor included a porous, fritted disk that supported the catalyst while allowing the reactor gas stream to continuously flow. In order to supply heat to reach reaction temperatures, the reactor was placed inside a Lindberg© vertical furnace. The temperature was controlled using an OMEGA© CN8500 temperature controller, and an OMEGA© DP 460 temperature readout instrument was attached to a thermocouple inserted inside the glass reactor in order to get a direct reading of the reaction temperature. Figure 3.9 is an image of the reactor setup used for experimentation.

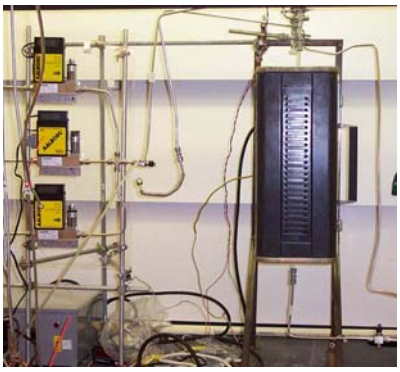

Figure 3.9 Reactor setup used for hydrogenation and hydrogenolysis reactions.

Mixtures of the reactant gases were purchased from Airgas©. A certified mixture of 10 mole % C_2H_6/balance H_2 was used for both gas chromatograph calibrations and as the reactant stream for the ethane hydrogenolysis reactions. Helium, also purchased from Airgas©, was added to the feed stream in order to vary its composition. A certified mixture of 10 mole % C_2H_4/balance H_2 was used for gas chromatograph calibration, but this mixture was not used for the ethylene hydrogenation reaction due to eventual catalytic activity caused by the active metal of the tank walls. Pure ethylene was

purchased from Airgas, and the reactant stream was formed by mixing ethylene with the appropriate amounts of pure hydrogen and helium to get a desired feed concentration. The flow of gas entering the reactor was controlled using Aalborg© flow meters. The flow meters were calibrated using a bubble flow device to ensure that accurate measurements of flow rates were obtained.

The Hewlett-Packard HP 6890 gas chromatograph, shown in Figure 3.10, was used for the gas analysis of the inlet and outlet reactor streams.

Figure 3.10 The HP 6890 gas chromatograph used for gas analysis.

A Carbosieve S-II (60-80 mesh) packed stainless steel column (1/8" x 4 ft) was used to separate the hydrocarbons. Figure 3.11 shows a sample chromatogram displaying the separation of various gases using a stainless steel column packed with Carbosieve S-II. The GC was also equipped with a thermal conductivity detector.

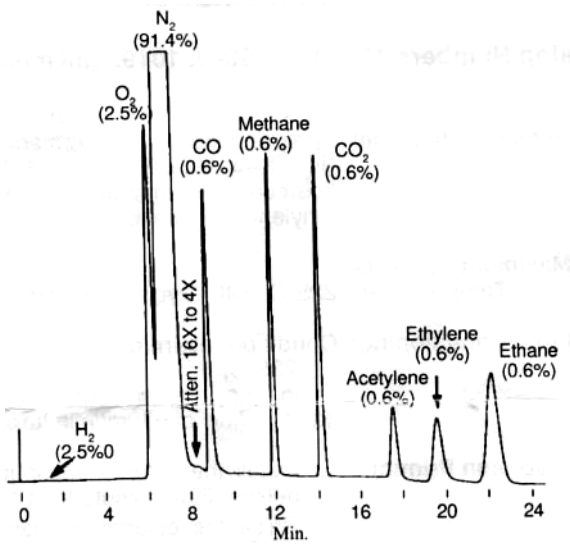

Figure 3.11 A sample chromatogram showing the separation of various gases using a Carbosieve S-II packed, stainless steel column [34].

Calibration curves showing the peak area vs. concentration for ethane, ethylene, and methane were developed. For C_2H_6 and C_2H_4, the previously mentioned mixture tanks were used in the calibration, and concentrations of both gases were varied between 0 and 8 mol. % by adding He to the mixture. A standard gas consisting of 5.17 mol. % CH_4, 1.93 mol. % CO_2, 0.991 mol. % CO, and the balance He was used to develop the methane calibration curve. Once again, He was used to dilute the concentration of methane between 0 and 3 mol. %. Table 3.3 gives the flow rates of each gas used to achieve the desired concentration of ethane, ethylene, and methane for calibration purposes. Also, Figure 3.12 shows the calibration curves developed for ethane, ethylene, and methane.

Table 3.3 Flow rates used in obtaining gas calibration curves.

Desired Concentration (mol%)	Corresponding Mixture Gas Flow (ml/min)	He Flow (ml/min)
0% C_2H_6, C_2H_4, CH_4	0	10
2% C_2H_6, C_2H_4	10	40
4% C_2H_6, C_2H_4	10	15
6% C_2H_6, C_2H_4	10	7
8% C_2H_6, C_2H_4	10	2.5
10% C_2H_6, C_2H_4	10	0
1% CH_4	10	41.5
3% CH_4	10	7
5% CH_4	10	0

a. Ethane Calibration Curve

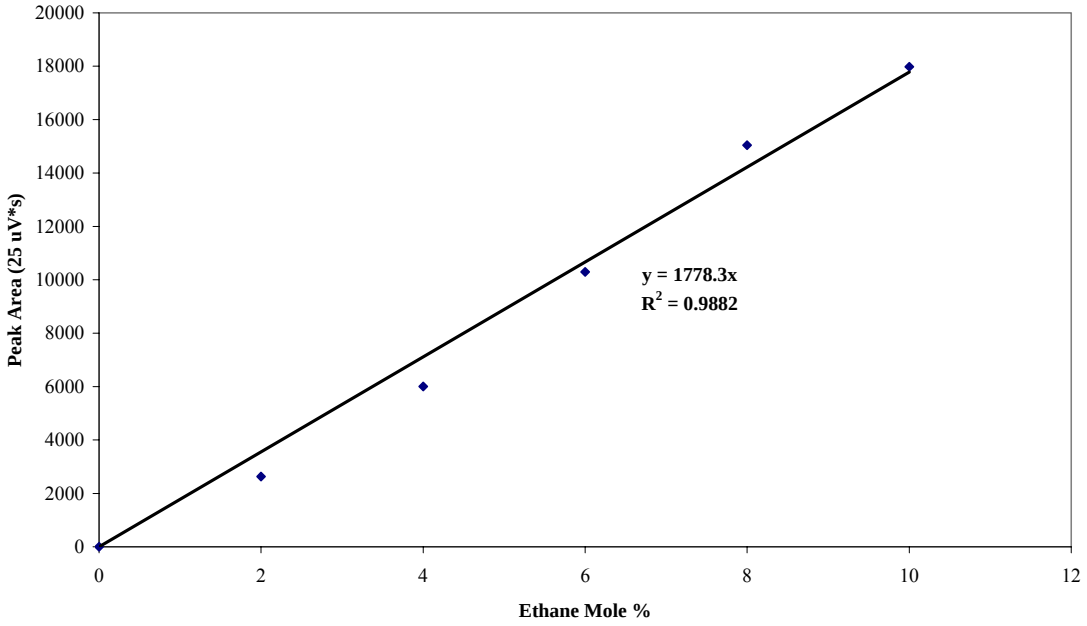

b. Ethylene Calibration Curve

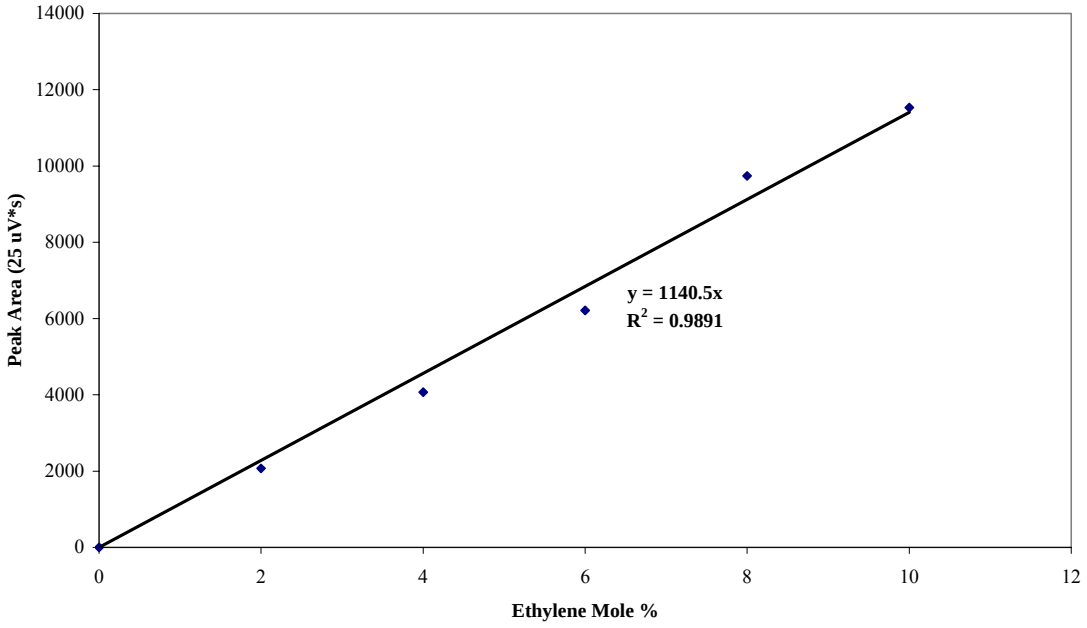

Figure 3.12 Gas calibration curves for a) ethane, b) ethylene, and c) methane.

c. Methane Calibration Curve

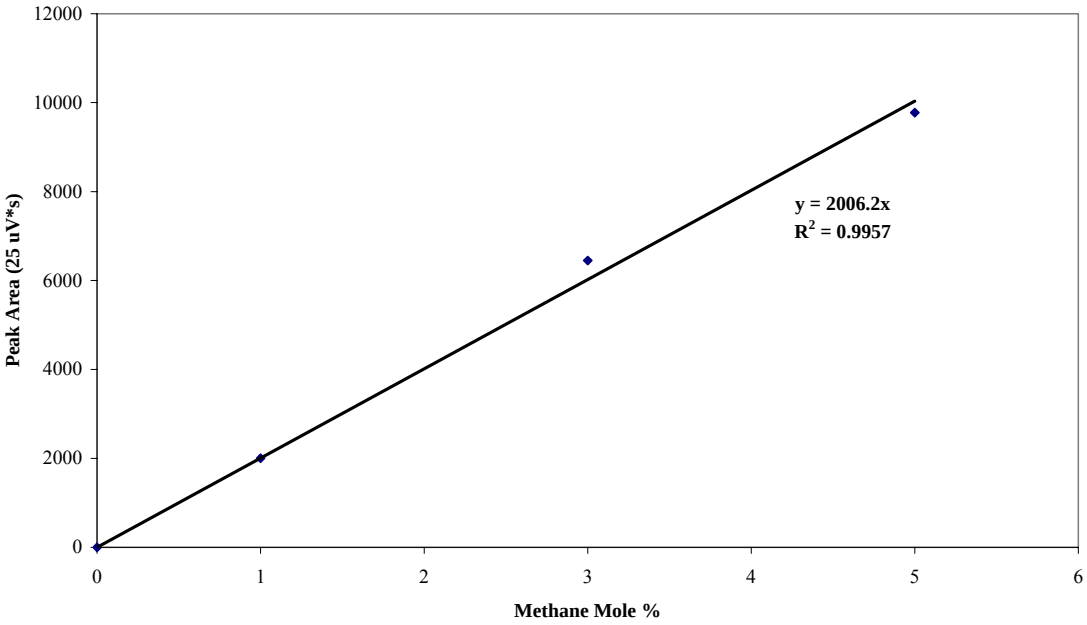

Figure 3.12 Continued.

As previously mentioned, test reactions were run using a commercial nickel catalyst sample obtained from Engelhard©. Engelhard's Ni-0750 catalyst was in 1/8" extrusion form. This catalyst was reduced and stabilized, and the catalyst is considered to be ideal for fixed bed hydrogenation reactions. The physical and chemical properties of the Ni-0750 catalyst are listed in Table 3.4.

Table 3.4 Physical and chemical properties of the Ni-0750 catalyst.

Surface area, m^2/g	175
Average crush strength, kgs	6.8
Total pore volume, cm^3/g	0.5
Packed A.B.D., g/cm^3	0.8
Nickel content, wt%	47.5

Using the Ni-0750 catalyst, ethane hydrogenolysis and ethylene hydrogenation reactions were conducted in order to fine-tune the reactor setup so that optimum reactor performance could be obtained and operating limitations could be determined. Flow rates were varied between 17-153 ml/min, and reaction temperature was varied between 80-100 ˚C for ethylene hydrogenation and 340-400 ˚C for ethane hydrogenolysis. Ultimately, these runs using the commercial Ni catalyst allowed the experimenter to: (i) debug the feed, reactor, and GC system, (ii) learn how to operate all reactor components simultaneously, (iii) learn how to analyze the date, and (iv) learn how to vary the operation parameters.

At the lowest limitations of reaction temperature and flow rates, a significant conversion was obtained using the Ni-0750 catalyst. Figure 3.13 shows conversion data for ethane hydrogenolysis at a reaction temperature of 340 ˚C, with the total flow rate varying and the amount of catalyst at 180 mg. As expected, the ethane conversion decreases with increasing flow rate due to lower residence time and external mass transfer limitations at the higher total flow.

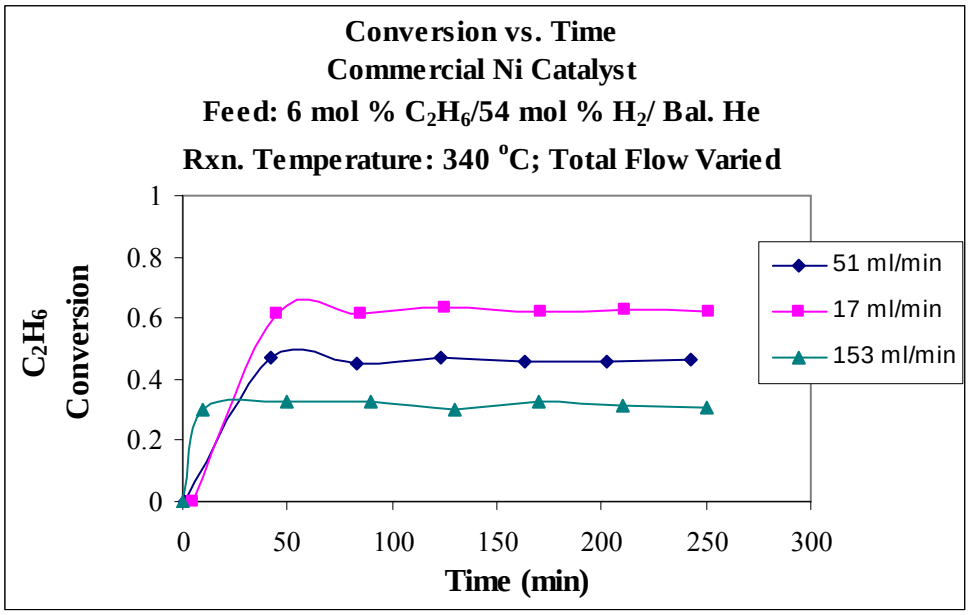

Figure 3.13 Plot showing conversion vs. time data for ethane hydrogenolysis using the Ni-0750 commercial catalyst.

From these preliminary reaction results using Ni-0750, the reactor performance was evaluated and determined to be satisfactory. However, because the commercial catalyst has a much higher active metal content at 47.5 wt. % Ni than the emulsion-prepared catalysts, it was not surprising that a significant conversion was noticed at all reaction conditions. When using our laboratory-prepared Ni catalysts, reaction conditions such as reaction temperature, amount of catalyst, and total flow rate had to be varied again in order to determine the optimum operating conditions.

3.4.2 Operational Considerations Due to Low Active Metal

The mono-dispersed catalyst samples prepared using microemulsions have a significantly lower nickel content than the typical commercial catalysts. This trade is necessitated by the desire to characterize the catalysts using the SEM/EDS technique. In this research, the highest concentration of aqueous $NiCl_2$ used was 0.1 M. This concentration was achieved by applying a heat source to promote the dissolution of $NiCl_2$. Higher concentrations could not be obtained due to the solubility constraints of $NiCl_2$ in water. Furthermore, the phase diagram restricts the amount of the aqueous metal salt solution that can be added to the microemulsion. For our purposes, it was desirable to keep the water-to-surfactant ratio, W_o, constant at the value that resulted in micelles with the lowest polydispersity. Due to these experimental considerations, the metal loadings were kept very low.

Due to the low Ni loadings of the emulsion-prepared catalysts, the amount of catalyst used, reaction temperature, and total flow rate had to be reconfigured in order to achieve a measurable reactor performance. Due to the structure-sensitivity of the ethane hydrogenolysis reaction, it was important to find conditions within the operating limitations of the reactor setup. As previously stated, the temperature limitation of 550 ˚C was imposed due to the use of Pyrex reactors. Because low total flow rates result in a higher residence time and thus a higher conversion, which is shown in Figure 3.13, it was advantageous to run both reactions at the lowest possible flow rate. Therefore, it was decided to keep the total flow at 17 ml/min. The amount of catalyst added to the system was limited by pressure drop concerns. In order to incorporate more space for gas flow in the catalyst bed, 0.5 g of sand was mixed with the loaded catalyst samples. For ethane

hydrogenolysis reactions conducted using the lowest wt. % Ni catalyst prepared, a significant conversion was noticed at a reaction temperature of 500 ˚C, total flow of 17 ml/min, and 1 g of catalyst. Because ethylene hydrogenation is a structure-insensitive, larger conversions were obtained well within the operating limitations of the reactor setup. The final set of operating conditions chosen for ethylene hydrogenation was a reaction temperature of 120 ˚C, total flow of 83 ml/min, and 1 g of catalyst. For both reactions, activity data were also obtained at ± 25˚C of the before-mentioned reaction temperatures for activation energy analysis.

3.4-3 Reactor Trials

In order to determine the effects of metal particle size on catalytic activity, ethane hydrogenolysis and ethylene hydrogenation reactions were conducted in the fixed bed reactor. Reactions were run using nickel catalysts of different metal particle size, and the activity of these catalysts were compared in order to determine crystallite size effects on activity. The particle size of the catalysts was varied by altering the $NiCl_2$ concentration within the reverse micelles.

For the ethane hydrogenolysis reactions, the catalyst samples were reduced in a stream of H_2 at a flow rate of 50 ml/min in a step-wise treatment to 500 ˚C over a period of 4.5 hours. Starting at 100 ˚C, the temperature was increased in 50 ˚C increments every 30 minutes until 500 ˚C was reached. The catalyst was then reduced at 500 ˚C for 30 minutes. The step-wise reduction treatment was chosen to minimize the sintering of the nano-sized nickel crystallites. After reduction, the hydrogen stream was cut off, and the desired reactant stream concentration was obtained through a bypass line. Afterwards,

the reactor line was opened, and the reaction was allowed to run for approximately 3.5 hours. GC samples of the product stream were analyzed in 30-minute intervals.

For ethylene hydrogenation, the catalyst samples were reduced in an identical manner to that described for the ethane hydrogenolysis studies. After reduction, the reactor bypass line was opened, and desired feed concentration was obtained while the reactor was cooled down to the reaction temperature. Once the reaction temperature was reached and the feed concentration set, the reactant stream was introduced into the reactor, and the same sampling process as used for the ethane hydrogenolysis reaction was followed.

CHAPTER 4

RESULTS AND DISCUSSION

This chapter presents the experimental results and their interpretations. First, micelle characterization results obtained from dynamic light scattering will be discussed. Second, SEM and EDS analyses of supported Ni crystallites are included, and from these results the size characteristics of Ni/Al_2O_3 catalysts with different Ni loadings were determined. Lastly, the activity of the emulsion-prepared Ni/Al_2O_3 catalysts was determined using ethane hydrogenolysis and ethylene hydrogenation reactions. These results are presented, along with the effects of crystallite size on catalytic activity.

4.1 MICELLE CHARACTERIZATION

Using dynamic light scattering, information about the size characteristics of the micelles within the microemulsions was obtained. The average micelle diameter, polydispersity, and distribution type were determined, and this information provided the basis for an estimate of the nickel crystallite size. This allows one to estimate which micelle size, along with the appropriate aqueous $NiCl_2$ concentration within the droplets, would lead to nano-particles in the size range of 2-10 nm. The following results were used to determine the optimal values of W_o and O/A for achieving micelle size of interest and lowest polydispersity.

4.1.1 Dynamic Light Scattering

Using DLS, intensity spectrums showing the size distribution curves for micelles were obtained for each microemulsion. Figure 4.1 is the intensity spectrums for the microemulsions with the following characteristics: $W_o = 10$, $O/A = 2$ and $W_o = 25$, $O/A = 5$. The aqueous $NiCl_2$ concentration used in both samples was 0.1 M. Referring to Figure 4.1a, the larger peak between 10^3-10^4 nm is due to the presence of sample impurities, as discussed in Section 3.1.3. The narrowness of the intensity peak around the average micelle diameter of 65.6 nm provides evidence of the size uniformity of the micelles. The polydispersity value of this sample was lowest at 0.023. The intensity spectrum shown in Figure 4.1b depicts a bimodal size distribution, with each peak being significantly wider than the one shown in Figure 4.1a. Thus, a broader size distribution is reported at less surfactant and higher oil content. It was thought that the first peak at 0.1 nm may be attributed to solvent noise, but it does not appear for every sample tested. Also, when the pure solvent was tested, this peak did not appear. Therefore, it is not clear what the first peak represents. The average reverse micelle diameter reported for this microemulsion was 107 nm (based upon the second peak). The shelf-lives for these samples were more than 3 months.

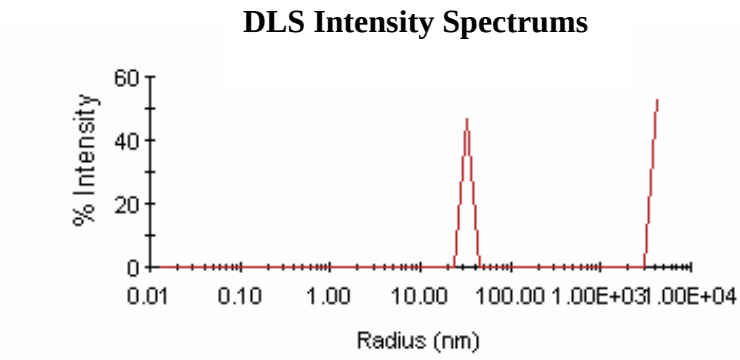

(a)

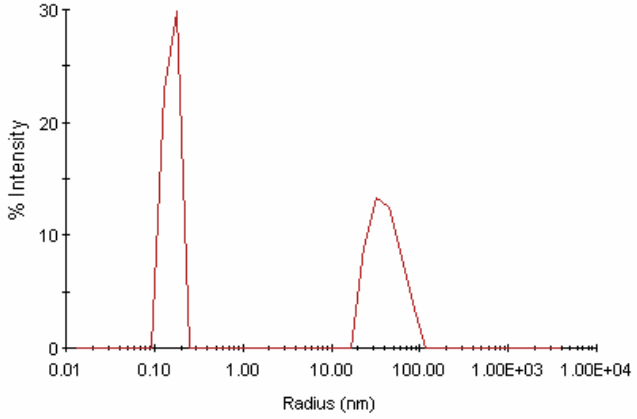

(b)

Figure 4.1 **DLS spectrum for microemulsion samples with a) W_o = 10, *O/A* = 2 and b) Wo = 25, O/A = 5. The aq. $NiCl_2$ concentration was 0.1 M for both samples.**

Table 4.1 gives a consolidated format of the micelle characterization results, including the micelle polydispersity, *Pd*, and shelf-life of each microemulsion. The polydispersity index is the ratio of the weight average molecular weight to the number average molecular weight. Though common in polymerization, the polydispersity index basically indicates the distribution of individual molecular weights. The weight average molecular weight is determined by weighing a number of molecules, adding the squares of these weights, and then dividing by the total weight of the molecules. The number average molecular weight is the common average of the molecular weights of individual molecules. It is determined by measuring the molecular weight of *n* molecules, summing the weights, and dividing by *n*. The value for polydispersity given in Table 4.1 is the absolute value of the molecular weight ratio subtracted from one. Therefore, the closer the values of *Pd* to zero, the more uniform the micelle size distribution. Note that the *Pd* value was given for microemulsions whose micelles exhibited a mono-dispersed distribution.

The shelf-life of each microemulsion is also presented in Table 4.1. As discussed in Section 3.1-4, the shelf-life is the time at which no visible phase separation is detected in the microemulsion. The shelf-life is important because it serves as a checkpoint in determining emulsion stability. As one can see, most of the emulsions are stable for more then 3 months.

Table 4.1 Micelle size characteristics and shelf life of microemulsions.

O/A	Sample	W_o	Distribution Type	Average *d* (nm)	*Pd*	Shelf life
2	1	5	Bi	24.6	-	< 24 hr.
	2	10	Mono	65.6	0.023	> 3 mon.
	3	15	Mono	97.8	0.36	> 3 mon.
	4	20	Mono	124	0.043	> 3 mon.
	5	25	Mono	136	13	> 3 mon.
	6	30	Mono	153	10	> 3 mon.
5	7	5	Mono	264	9.8	> 3 mon.
	8	10	Mono	117	11	> 3 mon.
	9	15	Bi	123	-	> 3 mon.
	10	20	Mono	86	5.8	> 3 mon.
	11	25	Bi	107	-	> 3 mon.
	12	30	Bi	160	-	> 3 mon.

4.2.1 Micelle Size vs. Nano-particle Size

Using the calculation described in Appendix A.1, a crystallite size estimate was obtained based upon the reverse micelle size obtained from DLS and the known Ni loading. Figure 4.2 shows the relationship between particle and micelle size for microemulsions prepared with different values of W_o, but with *O/A* constant at 2 and the aqueous $NiCl_2$ concentration within micelles at 0.1 M.

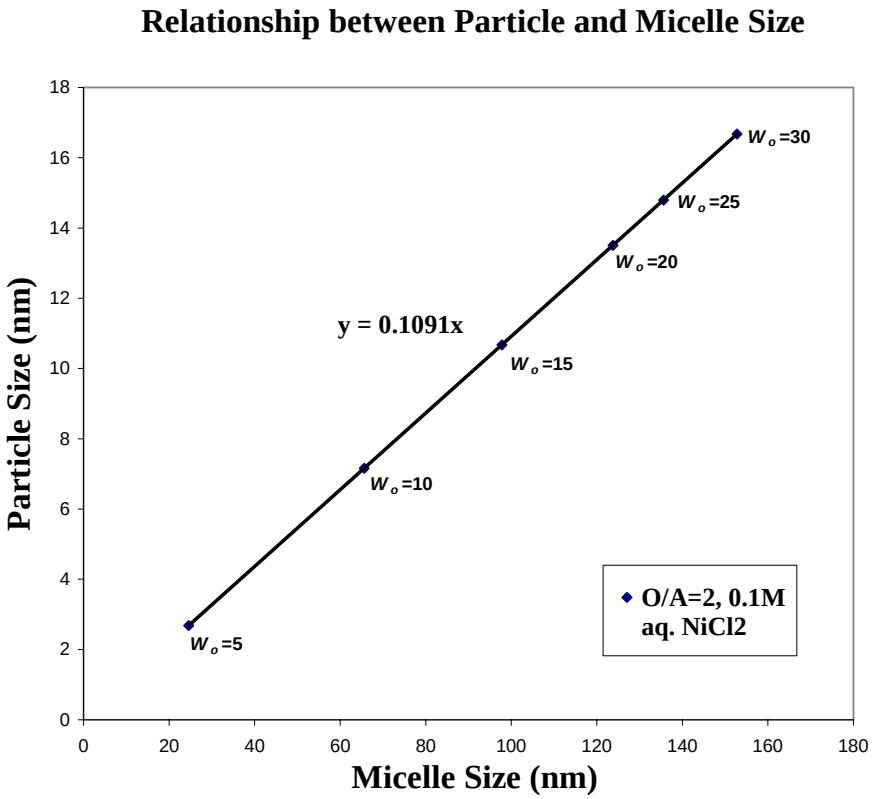

Figure 4.2 Correlation between micelle and particle size.

Figure 4.3 gives the micelle size and corresponding nickel crystallite size estimate as a function of the aqueous $NiCl_2$ concentration within each micelle at W_o = 10 and *O/A* = 2. The purpose of this graph is to elucidate any effects that the metal salt concentration may have on the micelle size, and in turn to determine whether these size effects or the salt concentration will potentially have the biggest influence on the size-tailoring of the nickel crystallites.

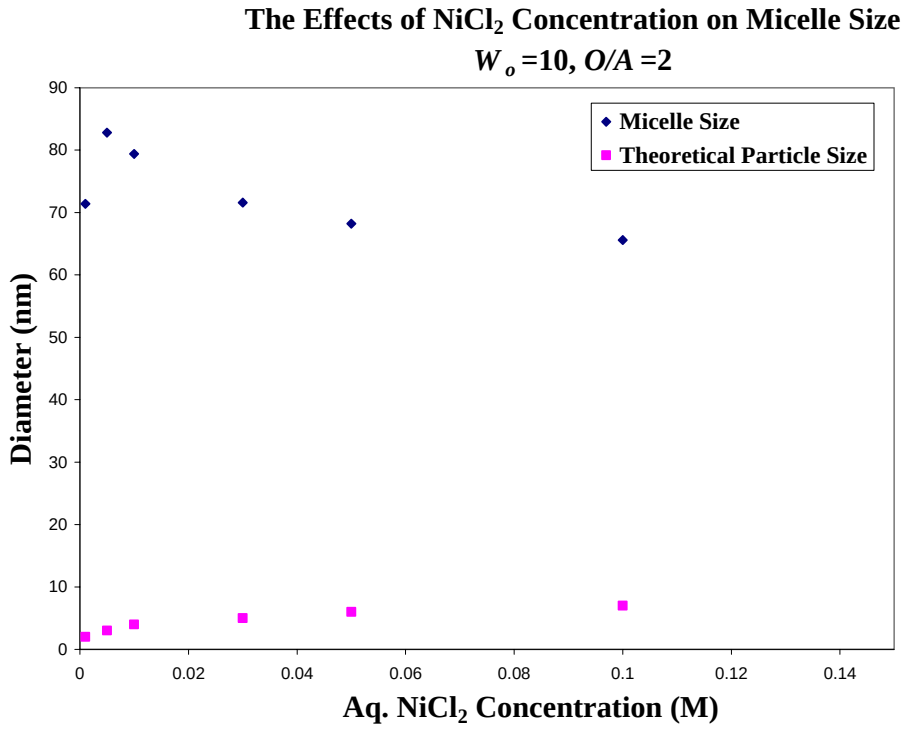

Figure 4.3 Aqueous $NiCl_2$ concentration effects on micelle diameter.

4.1.3 Effect of Preparation Variables on Micelle Characteristics

Figure 4.4 illustrates the micelle diameter dependence on the water-to-surfactant molar ratio, W_o. At oil-to-aqueous phase molar ratios, O/A, of 2 and 5, the value of W_o was varied between 5 and 30. Figure 4.4 reports the average micelle diameter, in nm, as a function of W_o.

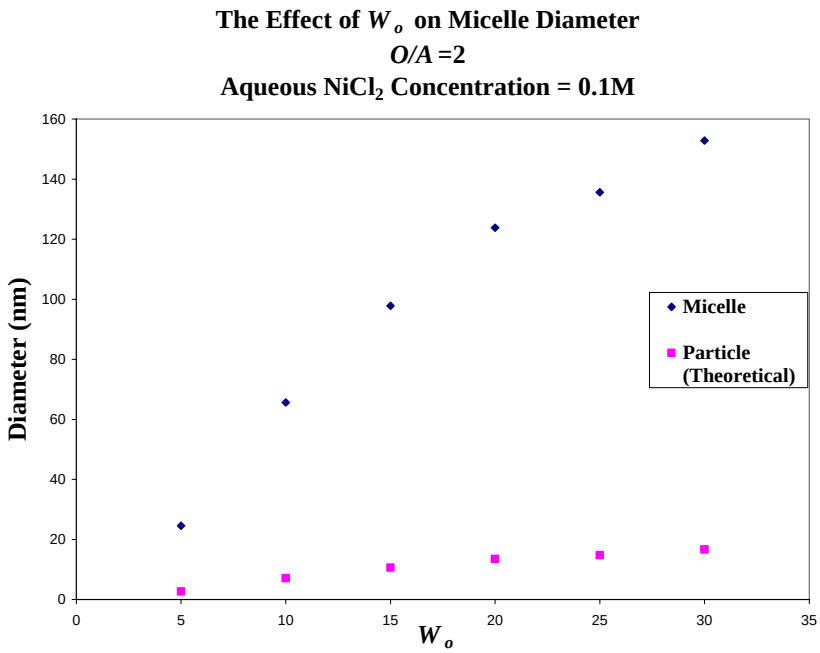

(a)

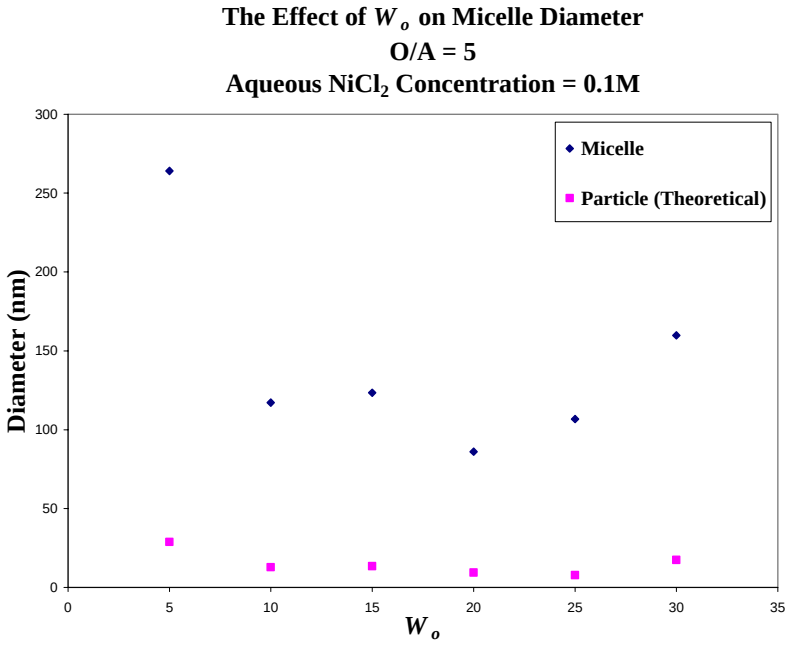

(b)

Figure 4.4 Micelle diameter and particle diameter estimation as a function of W_o at a) O/A = 2 and b) O/A = 5.

As shown in Figure 4.4a, the micelle size increases linearly with W_o at an *O/A* value of 2. A linear relationship between the diameter of reverse micelles and W_o was also noticed by Qiu et al. [3] when using sodium dodecyl sulfate (SDS)/isopentanol/cyclohexane/water microemulsions to produce Cu nanoparticles. It is expected that micelle size would increase with W_o because lower values of W_o indicate the presence of more surfactant in the microemulsion system. Using larger amounts of surfactant is advantageous in microemulsion preparation because this results in a stronger mechanical barrier around the liquid droplets. As a result, the barrier prevents the micelles from coalescing upon colliding into one another. At higher values of W_o, less surfactant is present in the system. Consequently, the barrier is weaker and the stability of the emulsion is reduced as more micelles are able to coalesce together after colliding, forming larger, unstable droplets.

From Figure 4.4b, one can see that the micelle size does not increase with W_o at *O/A* = 5. Instead, the micelle size fluctuates with W_o. Basically, this increase in *O/A* can be interpreted as an increase in the amount of oil in the microemulsion. From experimental results, it has been noticed that increasing the amount of oil in the system results in less stable microemulsions. Referring to Table 4.1, for *O/A* = 5 at W_o = 15, 25, and 30, bimodal size distribution curves were noticed. This indicates the presence of a very broad micelle size distribution, which is not indicative of a stable microemulsion. This instability may be due to the shifting of the phase diagram position when increasing the amount of oil in the system. This increase in oil corresponds to a composition farther from the center of the reverse micelle regime and closer to the boundary. The closer the composition of the microemulsion to the reverse micelle region boundary, the more

unstable the microemulsion becomes [18]. Therefore, one would expect a more broad size distribution and higher values of polydispersity, which are reported in Table 4.1, as more oil is added to the system. For these reasons, $O/A = 2$ was chosen as an optimal value for the ratio of oil-to-aqueous phase.

The theoretical particle size calculated based upon the reported average micelle diameter and known aqueous $NiCl_2$ concentration are also shown in Figures 4.2 and 4.3. At the optimal value of O/A=2, the particle size varies from 3-17 nm as W_o is altered from 5-30 with the aqueous $NiCl_2$ concentration constant at 0.1 M. Because particle nucleation is confined within the contents of the micelle, one would expect the particle size to exhibit the same trend as micelle size with respect to W_o. Figure 4.2 shows that theoretical crystallite size increase linearly with micelle size at O/A=2. The micelle size was varied by changing W_o. Figure 4.3 also shows that the theoretical particle size increases with the aqueous $NiCl_2$ concentration as well, despite slight fluctuations in the reported average micelle diameter. From aqueous $NiCl_2$ concentrations of 0.001 M to 0.005 M, the micelle size increases from 71 to 83 nm, but the theoretical particle size only increases from 2 to 3 nm. From an aqueous $NiCl_2$ concentration range of 0.001 M-0.1 M, the theoretical particle size ranges from 2-7 nm. Thus, results show that it would be ideal to vary the crystallite size by altering the aqueous $NiCl_2$ concentration because this can be done without significantly affecting the stability of the microemulsion system. Alternatively, varying the micelle size by changing W_o has a greater effect on the micelle stability, as evidenced by changes in the polydispersity and micelle size distribution type as the amount of surfactant is varied.

Based upon dynamic light scattering results, W_o=10 was chosen as an optimal condition because at this value micelles were produced that had a favorable size that led to an estimate of crystallite size in the range of interest. Furthermore, at W_o = 10, micelles with the lowest polydispersity at 0.023 nm were produced. Figure 4.1 is an image of the dynamic light scattering spectrums for the microemulsion samples with W_o=10, *O/A*=2 and W_o=25, *O/A*=5, with an aqueous $NiCl_2$ concentration of 0.1 M for both. The spectrum shown in Figure 4.1b shows the bimodal distribution reported for the microemulsion prepared at a lower surfactant and higher oil content. As expected, this spectrum depicts a broader size distribution than that shown for the microemulsion with a higher surfactant and lower oil content. As one can see in Figure 4.1a, this peak is very sharp, indicating a narrow size distribution around the average micelle diameter of 65.6 nm. The peak between 10^3 and 10^4 nm are from sample impurities, as discussed in Section 3.1.3. Additionally, the reported micelle size, along with the aqueous $NiCl_2$ concentration of 0.1 M, leads to a crystallite size estimate of 7 nm, which is in the range of 2-10 nm. By varying the $NiCl_2$ concentration, it is expected that the size will vary as shown in Figure 4.3. Research conducted by Qiu et. al. [35] for the preparation of CeF_3 nanoparticles has shown that the polydispersity of particles increased with the precursor salt solution concentration. Therefore, by lowering the aqueous $NiCl_2$ concentration from 0.1 M in order to change the crystallite size, one would expect the crystallites to become more mono-dispersed.

In comparison to previous research conducted using microemulsions to prepare nanoparticles, our experimental results are comparable with respect to choosing an optimal value of W_o. Qiu et. al. [3] noticed that their Cu nanoparticles possessed good

monodispersity, i.e. size 3-6 or 7-12 nm, at values of W_o at 5 and 10. At higher values of W_o, their particles were characterized by a much broader size distribution in the range of 24-43 nm. As previously discussed, the presence of large sized and polydispersed particles at higher values of W_o may be due to the aggregation of nuclei and primary particles because of the weaker barrier formed as a result of the lower quantity of surfactant molecules present. Additionally, Dadyburjor et. al [17] also used $W_o = 10$ as their optimal value when using reverse micelles to create small ferric sulfide catalytic particles. Therefore, the optimal value of $W_o = 10$ chosen in this research based upon experimental results is comparable with research done by others using reverse micelles to prepare nanoparticles.

4.2 NICKEL CRYSTALLLITE CHARACTERIZATION

Scanning electron microscopy and energy dispersive X-ray microanalysis were used to characterize the nickel catalysts. The SEM sample support, indium, and the catalyst support, alumina powder, were also analyzed to obtain a baseline for comparison. The alumina-supported Ni catalyst was analyzed both after calcination and calcination-reduction. For the images obtained with highest resolution, EDS was used to confirm the presence of nickel.

Based upon the nickel nano-particle size distribution viewed using SEM, the amount of Ni loading on the catalyst was reduced to prevent particle aggregation. Ni loading was reduced in two ways: (i) lowered amounts of emulsion added to a given amount of alumina powder, and (ii) reduced concentration of aqueous $NiCl_2$. The first would lead to a lower number of metal crystallites per unit surface area of alumina, thus minimizing the extent of particle aggregation. The second would reduce the size of the nickel crystallites. Experimental results verified this rationale for catalyst preparation. As previously stated, the ultimate goal was to prepare several batches of Ni catalysts with crystallite particles in the size range of 2-10 nm with a narrow size distribution. Table 4.2 presents a summary of the Ni metal loadings used in this study.

Table 4.2 Ni metal content of each catalyst sample.

Catalyst	Ni Metal Loading (wt. %)
A	0.039
B	0.0039
C	0.0013
D	0.00039

4.2-1 Surface Analysis of Sample Supports (In & Al_2O_3)

When using SEM, it is important to identify the surface characteristics of each component of a sample. For our SEM analysis, the catalyst samples were pressed into an indium foil in order to increase the overall conductivity of the sample so that SEM images at high magnification and clear resolution could be obtained. Therefore, it was important to develop a distinction between the surface of the indium foil and the deposited alumina particles. This should help differentiate between the alumina and the indium surface when trying to obtain micrographs of the supported active metal. As a result, SEM images of the plain and alumina-deposited indium surfaces were gathered, and these micrographs are shown in Figures 4.5 and 4.6. As one can see, the indium surface seems to have a lot of ridges and crevices, which is in contrast to the surface of the alumina mesh particle shown in Figure 4.7.

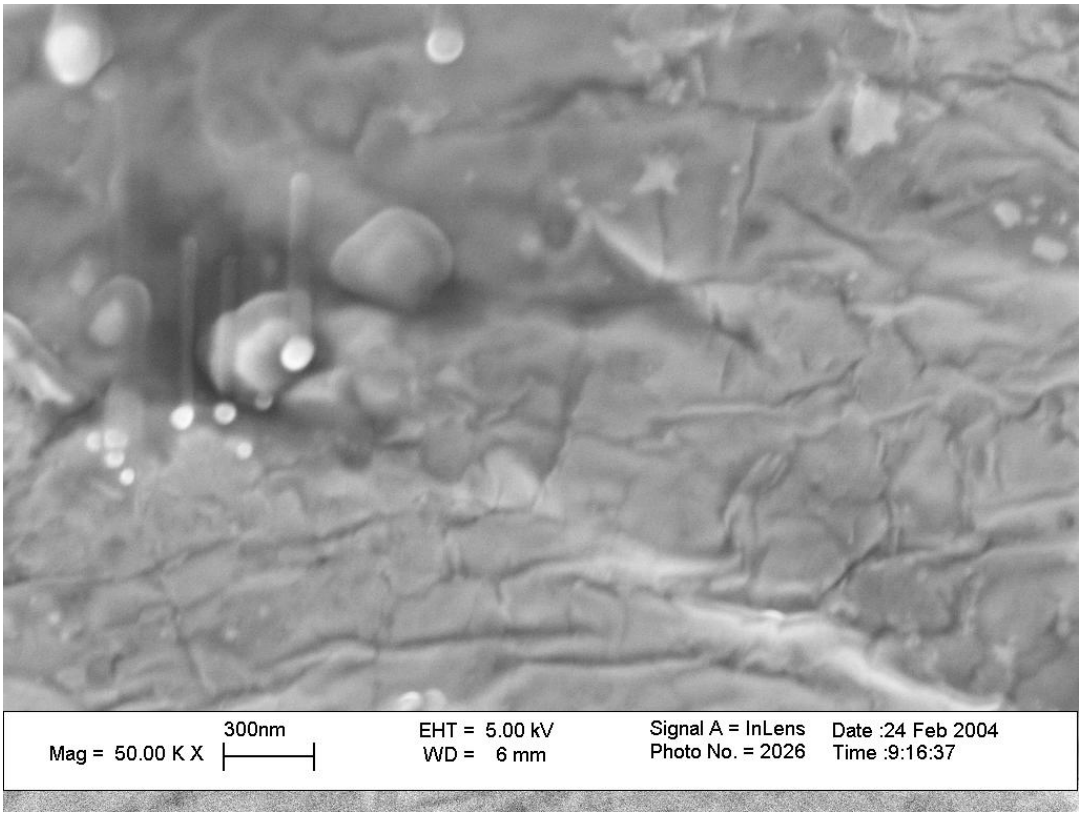

Figure 4.5 Scanning electron micrograph of indium surface at 50 K X.

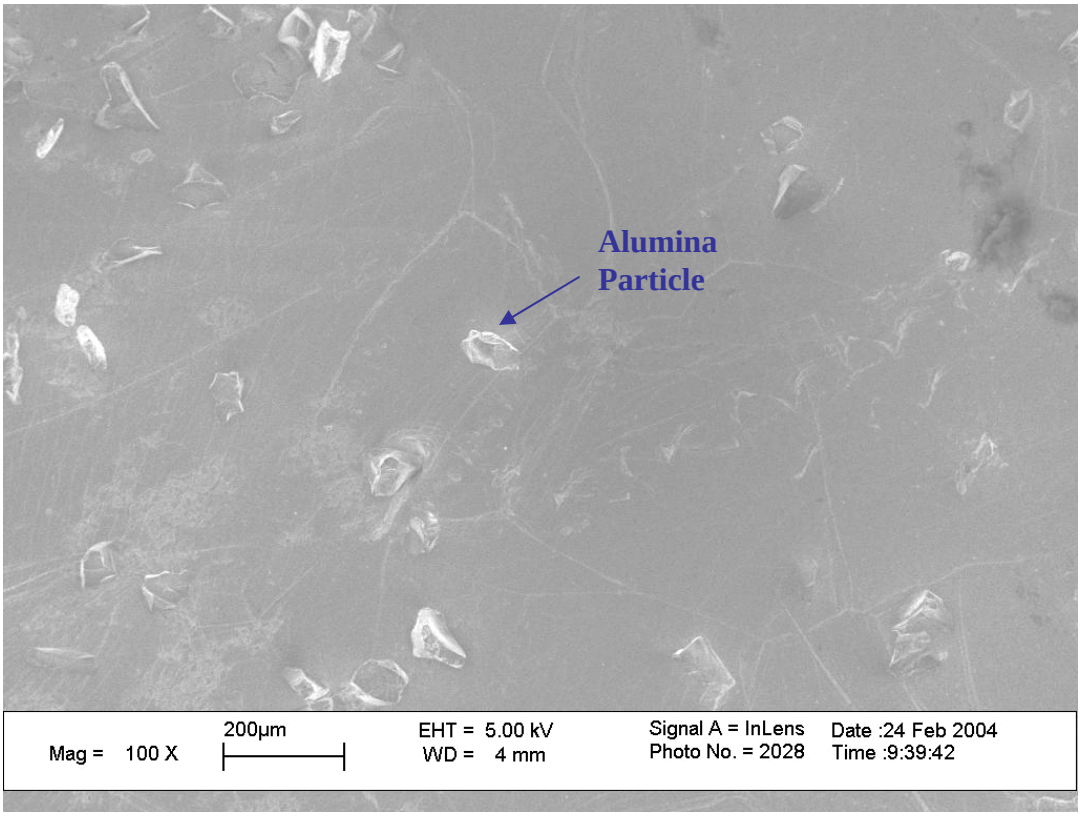

Figure 4.6 **Scanning electron micrograph of the alumina-deposited indium surface at 100 X.**

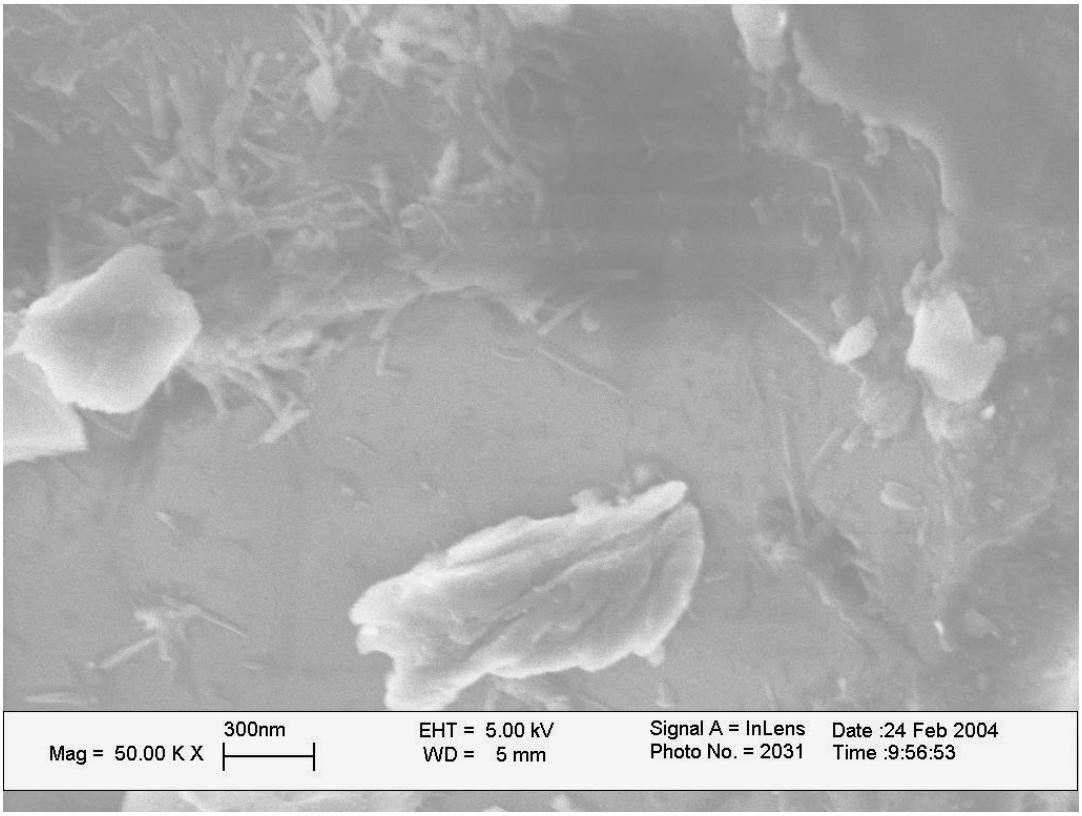

Figure 4.7 Scanning electron micrograph of an alumina particle at 50 K X.

Referring to Figure 4.7 above, the alumina particles can be characterized as having a smooth surface with nodular features. Using this image as a background, one can easily attribute changes in the alumina surface morphology to those caused by the presence of Ni crystallites. The next sections shows micrographs of the catalysts prepared using different Ni loadings.

4.2-2 SEM/EDS Analyses of Ni/Al_2O_3 Samples

Figures 4.8-4.10 show the scanning electron micrographs of .039 wt. % Ni catalyst after calcination at 400 ˚C. The purpose of the calcination step is to eliminate the volatile and unstable species that are not desired in the final catalyst, leaving only metal oxides on the support surface. As one can see from the SEM images, particles are dispersed upon the alumina surface in a manner not seen on the plain alumina surface shown in Figure 4.7. These images are presented at different magnifications and three different locations on the catalyst surface.

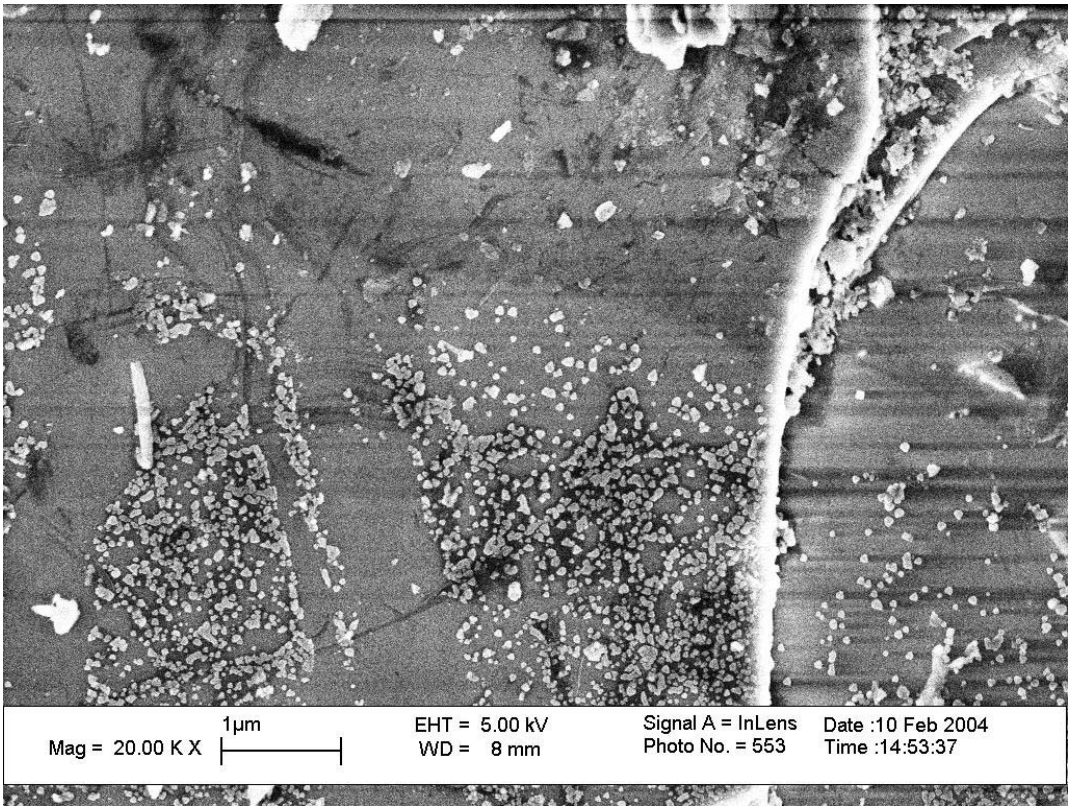

Figure 4.8 SEM image of .039 wt % Ni catalyst after calcination (20 K X).

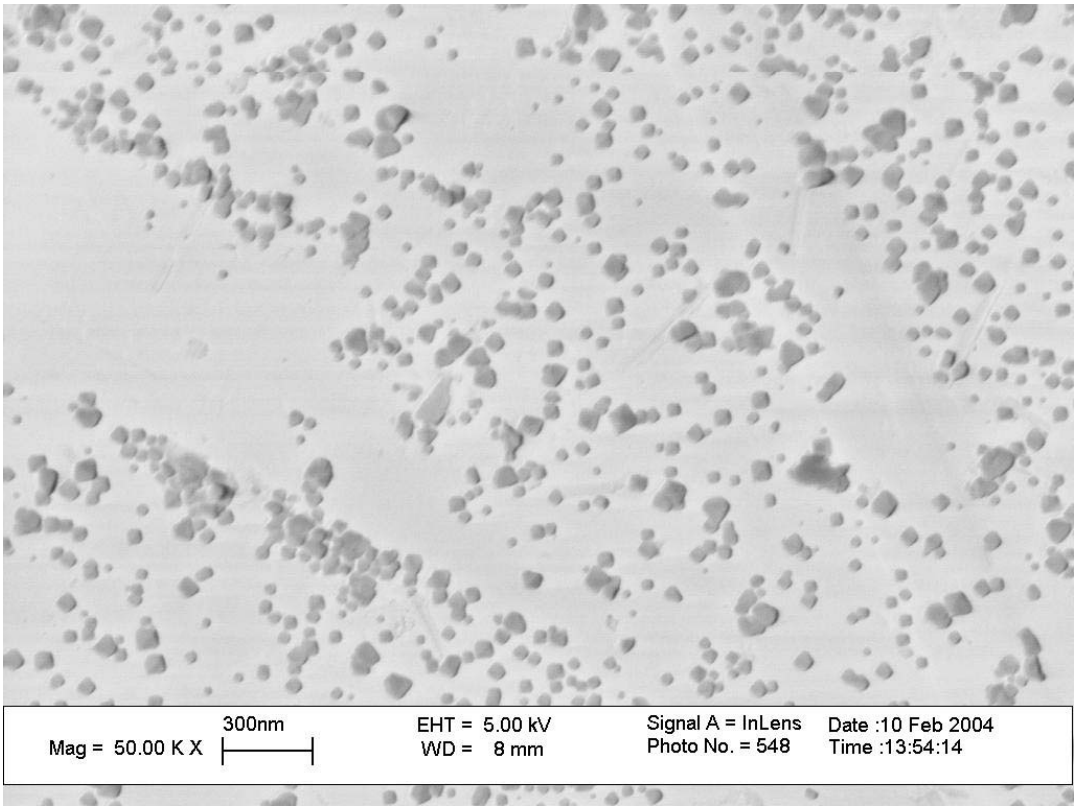

Figure 4.9 SEM image of .039 wt % Ni catalyst after calcination (50 K X).

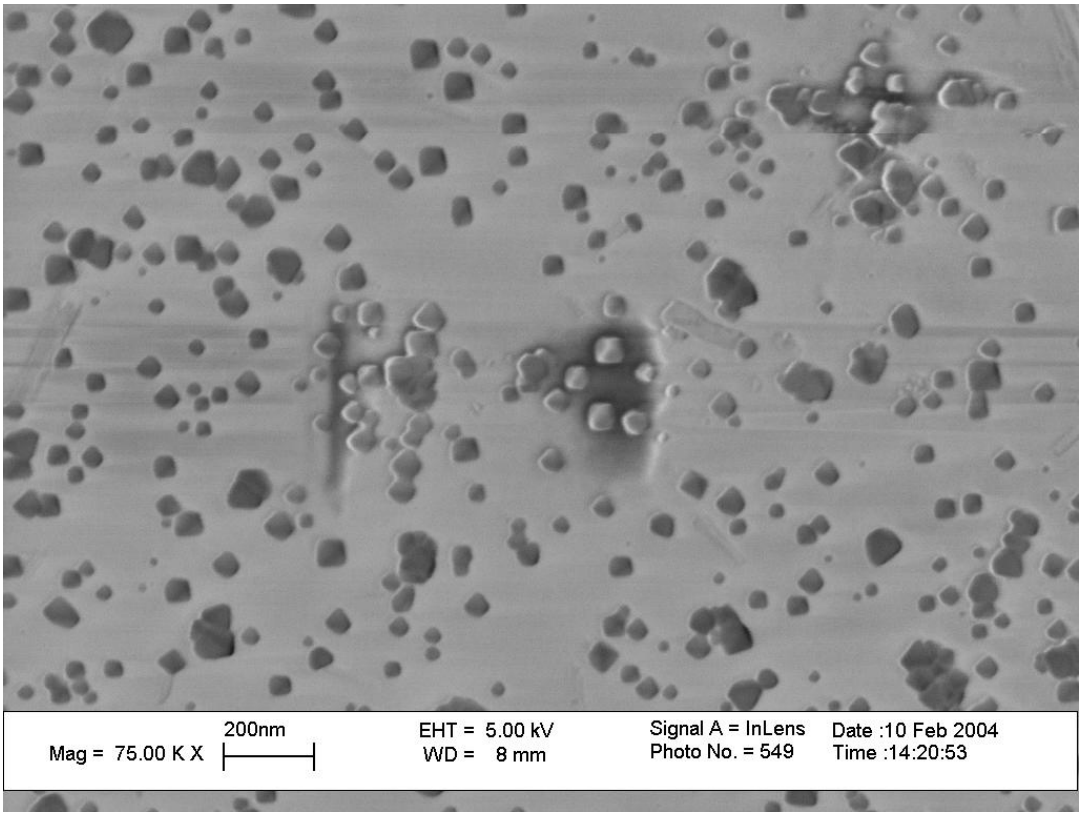

Figure 4.10 SEM image of .039 wt % Ni catalyst after calcination (75 K X).

EDS analysis was conducted on Location 1 at a magnification of 50 K in order to confirm the presence of nickel nano-particles on the support surface. Figure 4.11 is the EDS intensity spectrum obtained for the area shown in Figure 4.9. As one can see, the sharp Al and O peaks confirm that the support material is alumina. The Ni peaks confirms the presence of nickel in the scanned area.

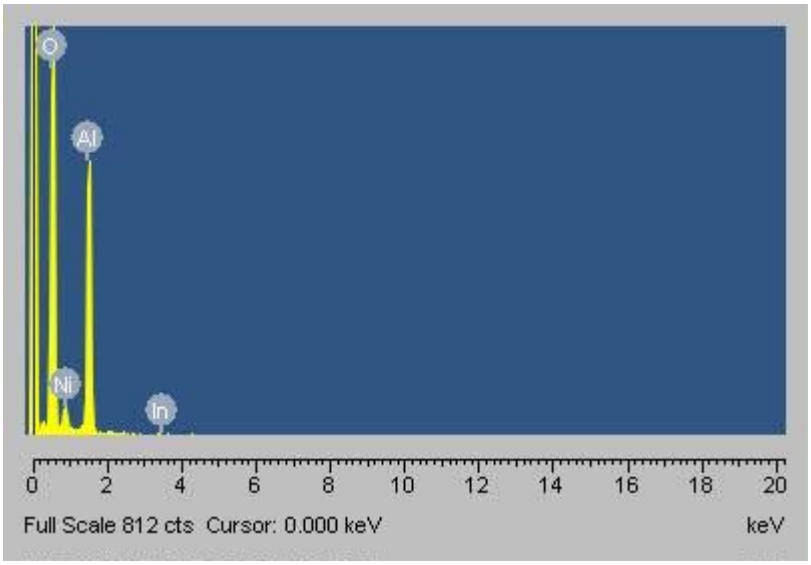

Figure 4.11 EDS intensity spectrum obtained for .039 wt. % catalyst after calcination for the area shown in Figure 4.9.

The EDS mapping tool was used to illustrate the dispersion of Ni over the area scanned at 50 K X for the .039 wt. % catalyst. Referring to Figure 4.12, the red spots on the image represent the nickel spacing. As one can see, the red spots overlap the particles that are shown. Therefore, the mapping analysis further confirms that the particles present are forms of nickel-containing compounds.

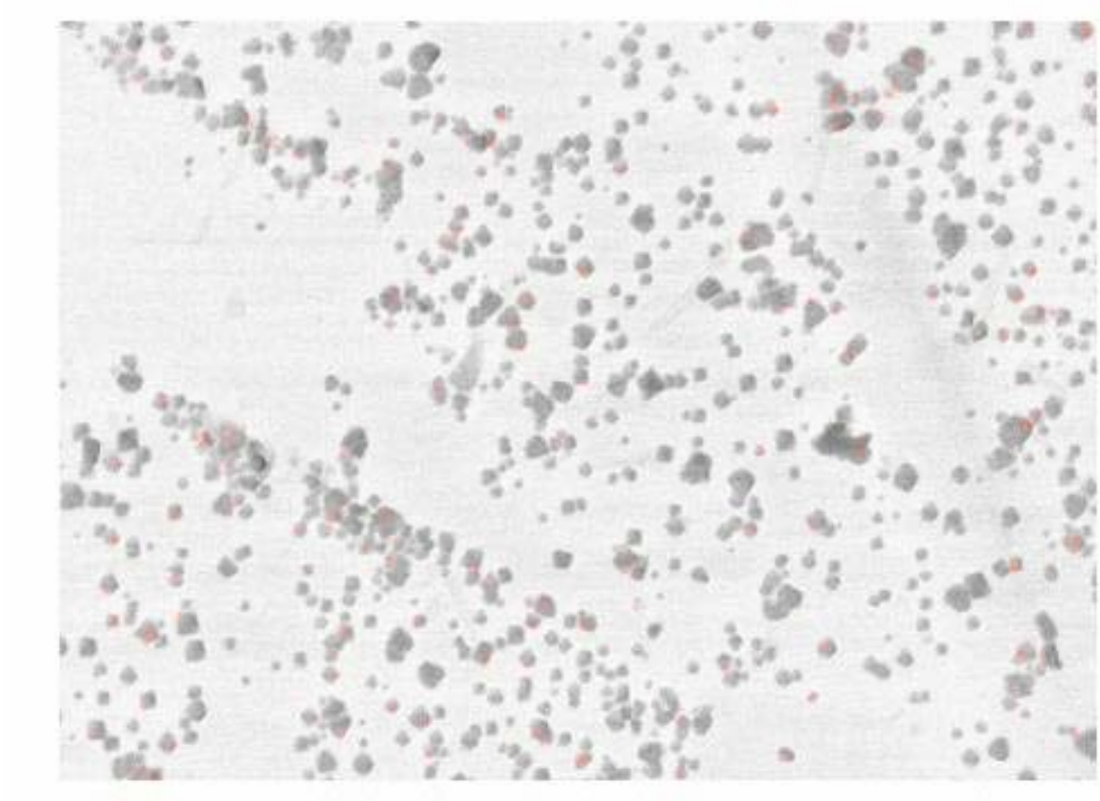

Figure 4.12 EDS nickel element map of .039 wt. % catalyst after calcination for the area shown in Figure 4.9 (50 K X).

In order to ensure that nickel compounds were present throughout the catalyst sample, scanning electron micrographs of the deposited active metal were obtained at other locations. The following images show nickel compounds at a second location in the .039 wt. % Ni sample. In contrast to the previous figures, the nickel compounds shown in these micrographs have aggregated together, possibly because of sintering.

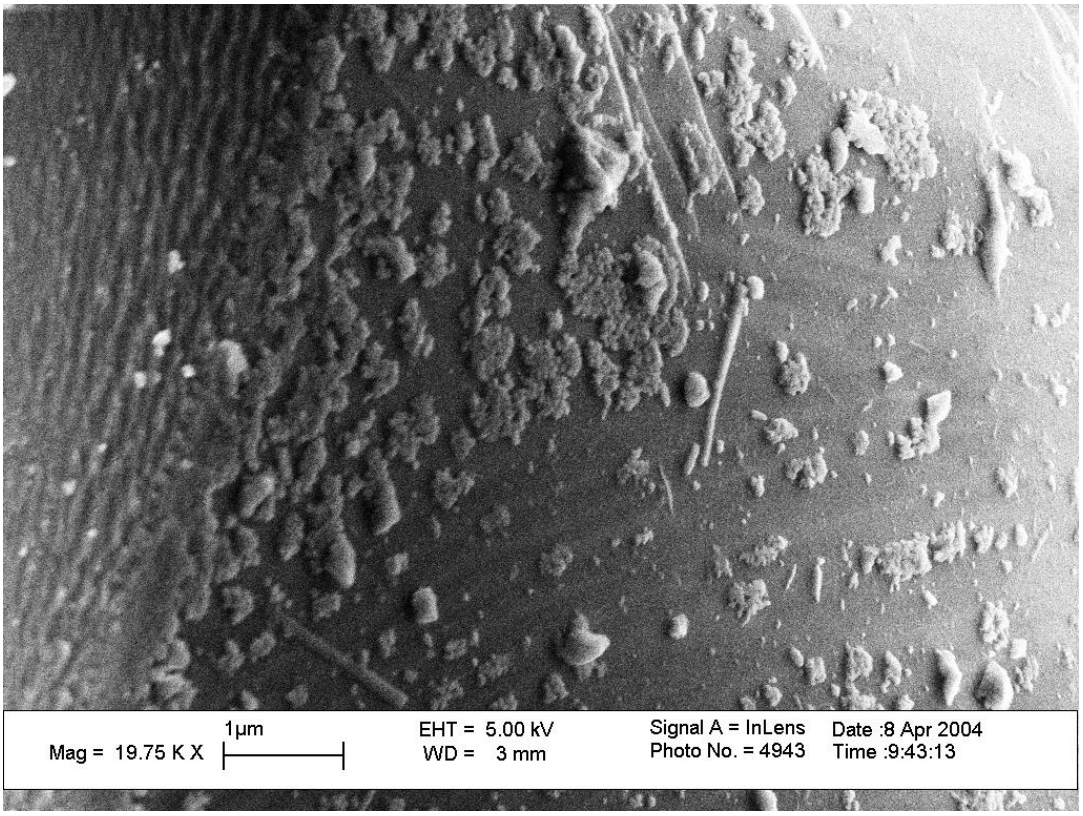

Figure 4.13 SEM image of .039 wt % Ni catalyst after calcination (20 K X).

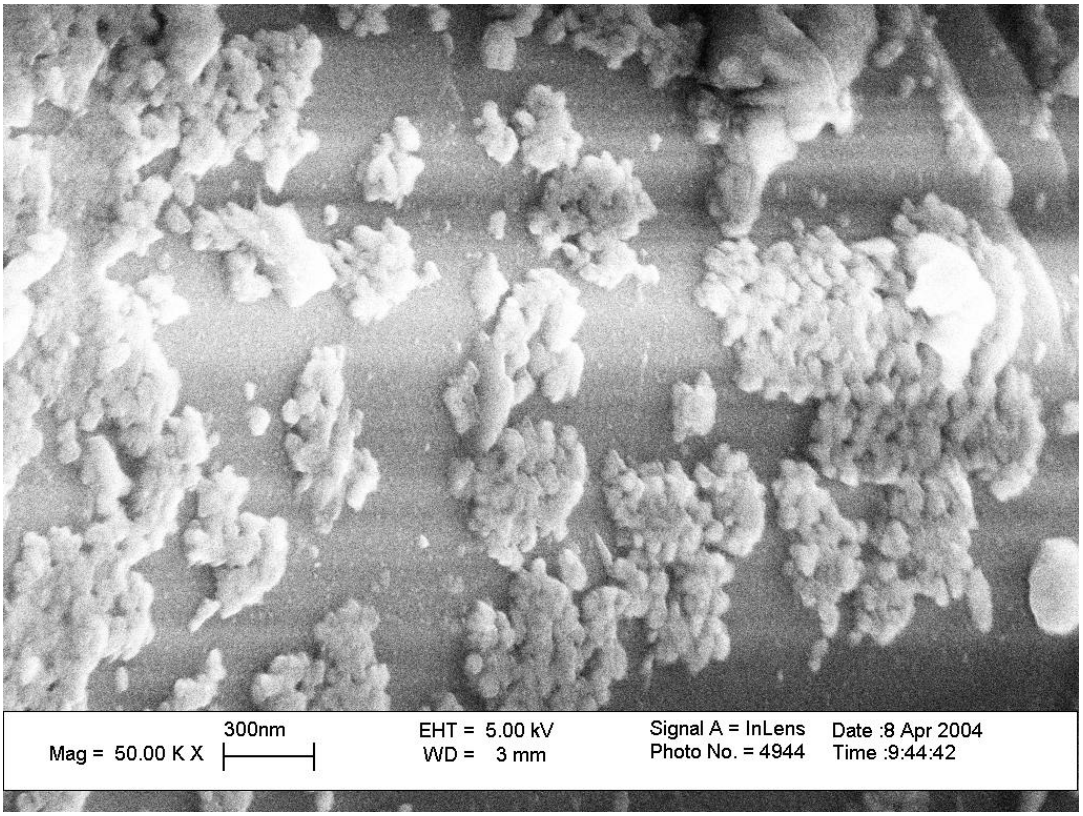

Figure 4.14 SEM image of .039 wt % Ni catalyst after calcination (50 K X).

EDS analysis was also conducted over the scanned area shown in Figure 4.14 in order to verify that nickel compounds were present. Figure 4.15 shows the EDS intensity spectrum that was obtained. The large Al and O peaks indicate the presence of the alumina support. The carbon (C) and indium peaks (In) are present due to the use of carbon tape and indium foil for sample conductivity purposes. Most importantly, the Ni peak confirms the presence of nickel compounds over the scanned areas.

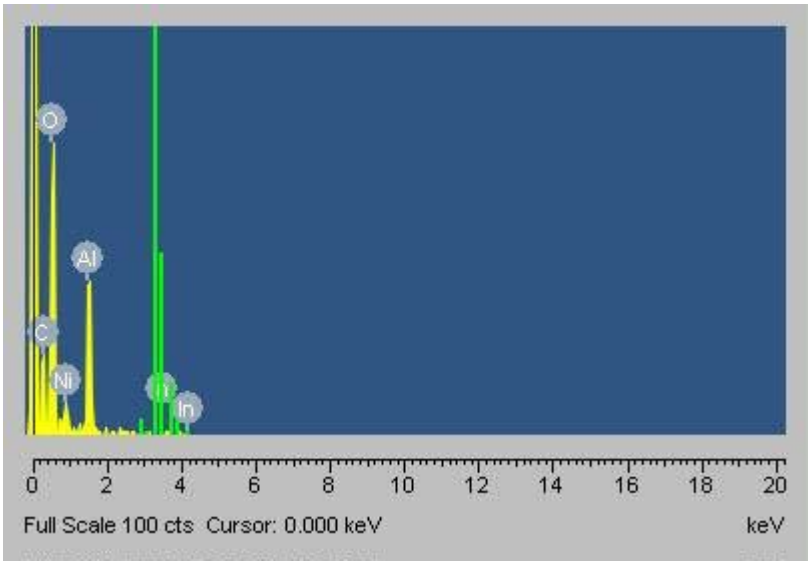

Figure 4.15 EDS intensity spectrum obtained for .039 wt. % catalyst after calcination for the area shown in Figure 4.14.

Lastly, a third location on the .039 wt. % Ni catalyst was chosen in hopes of detecting more nickel compounds. The next figure shows particles on the surface support that are dispersed in manner similar to the particles found in Location 1. EDS analysis was not undertaken at this location due to the extensive charging. When compared to the surface of plain alumina shown in Figure 4.7, one can infer that the particles shown in the

following micrograph are the result of emulsion deposition and may very well be active nickel-containing compounds.

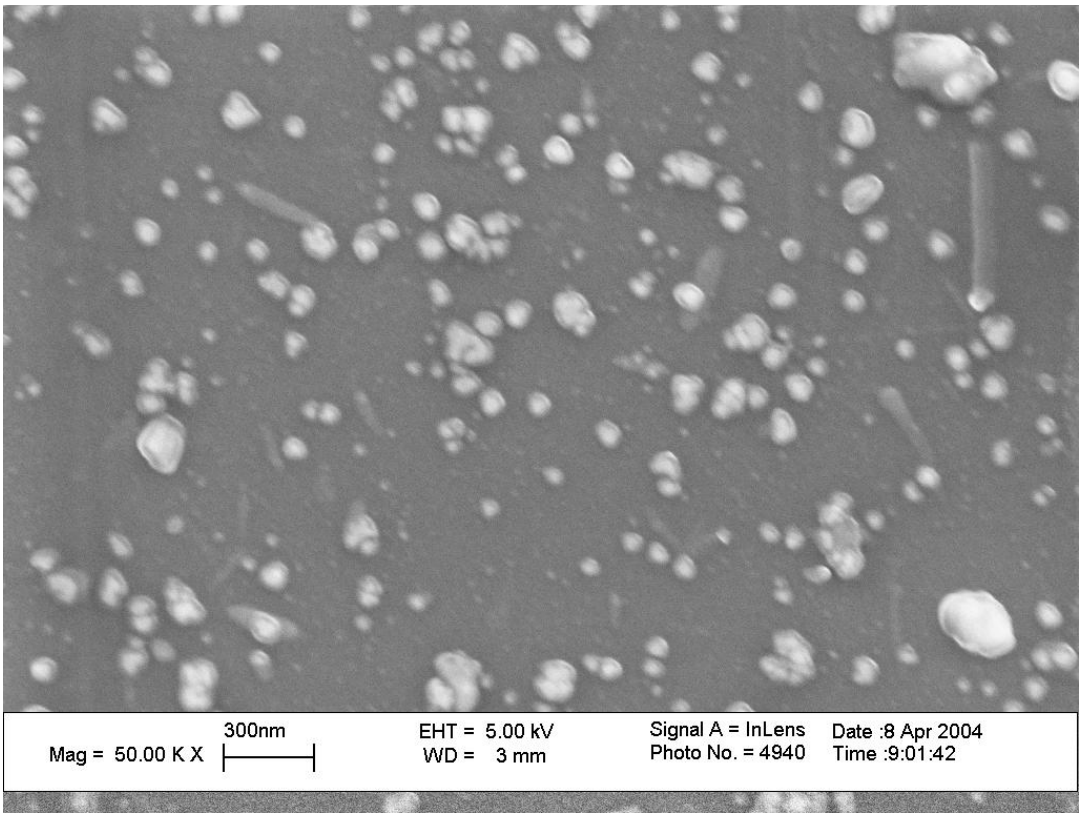

Figure 4.16 SEM image of .039 wt % Ni catalyst after calcination (50 K X).

Referring to the micrographs presented in this section, one can conclude that nano-sized nickel compounds are formed after the calcination stage. In comparison to work done by Chang et al. [12, 14-15] in the preparation of Ni/RHA-Al_2O_3 using traditional preparation techniques, nickel oxides are present on the support before the active metal is obtained upon reduction. These results confirm that the microemulsion preparation technique can be used to make nano-sized nickel particles. However, one can see from these images that the particle size distribution of the catalyst precursor at .039

wt. % Ni is very broad. The nickel oxide particle size varies from 10-90 nm, and from the images obtained at Location 1 it is clearly evident that particle aggregation is contributing to the formation of larger particles. Previous work done by Carter et. al. [7] has shown that increasing the treatment temperature used for Ni/SiO_2 catalyst results in a decrease in surface area due to the sintering of crystallites. More than likely, the calcination temperature of 400 ˚C may cause an increase in the surface migration of the crystallites on the support surface. Accordingly, the weight percentage of Ni in each catalyst sample was lowered from .039 wt. % in order to prepare smaller, more dispersed particles.

4.2-3 Nano-Sized Ni Particles

The following scanning electron micrographs show the supported Ni catalyst after calcination and reduction at various Ni loadings. As previously stated, the purpose of reducing the Ni content was to prepare smaller Ni particles with minimum agglomeration, thus resulting in a more uniform particle size distribution. The images in the following sections show how varying the Ni loading affects particle size.

A. .0039 wt. % Ni

Figures 4.17 and 4.18 show the .0039 wt. % Ni catalyst after calcination at 400 ˚C. The images were taken at several locations on the catalyst sample. When compared to the images of the .039 wt. % Ni catalyst after calcination, the nano-sized nickel compounds of the .0039 wt % Ni catalyst are smaller with a very uniform particle size distribution. Most of the particles are approximately 13-16 nm in size, and in contrast to the .039 wt. % catalyst precursor, particle aggregation does not seem to be occurring.

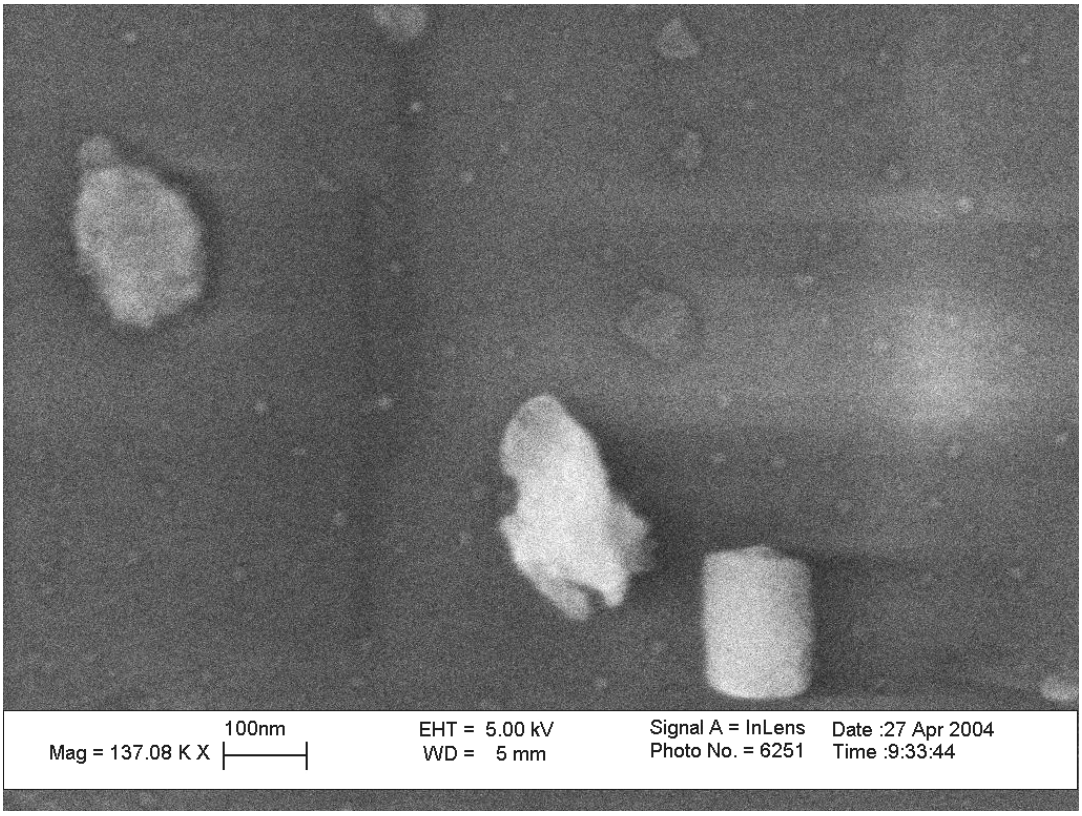

Figure 4.17 SEM image of .0039 wt % Ni catalyst after calcination (137 K X).

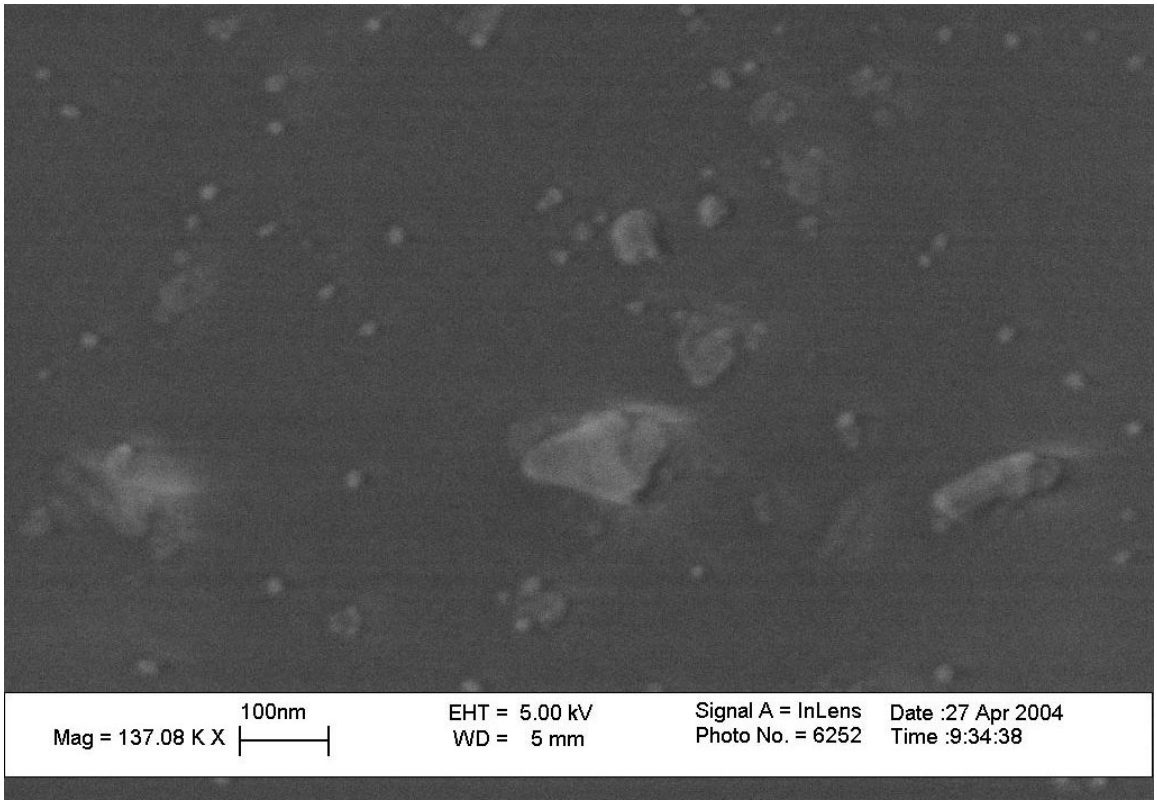

Figure 4.18 SEM image of .0039 wt % Ni catalyst after calcination (137 K X).

Scanning electron micrographs of the .0039 wt. % Ni catalyst at different locations after calcination-reduction at 500 ˚C were also obtained. Upon reduction, it was expected that the active Ni particle size would be smaller when compared to the nickel oxide compounds obtained after the calcination stage. Referring to Figures 4.19-4.22, the particle size ranges from 10-14 nm in size, indicating a uniform size distribution. From the reverse micelle size and amount of Ni loading, the crystallite size estimate was 7 nm. Although the particles detected are slightly larger than the estimate, the sizes viewed still fall into our range of interest. From Figure 4.19, one can see that locations on the catalyst surface are present where the crystallites seem to aggregate together and form clusters. This may be due to increased mobility for the small particles at the reduction temperature of 500 ˚C.

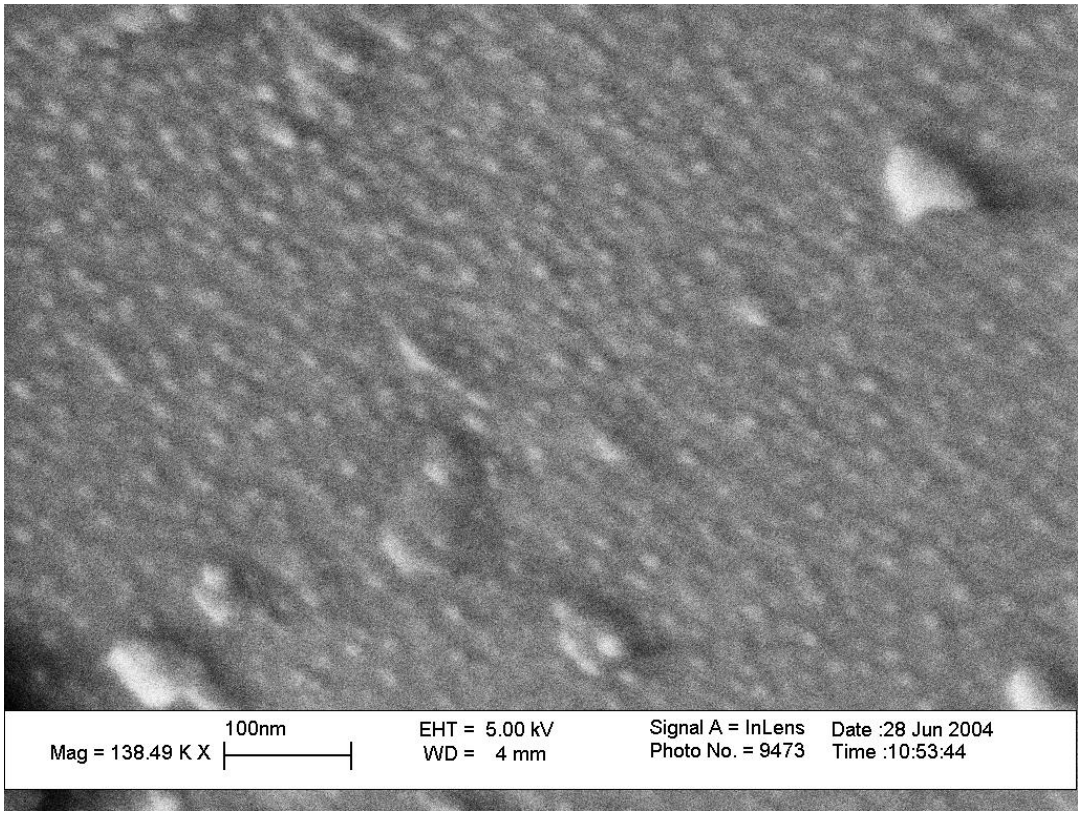

Figure 4.19 .0039 wt. % Ni after reduction to 500 ˚C (138 K X).

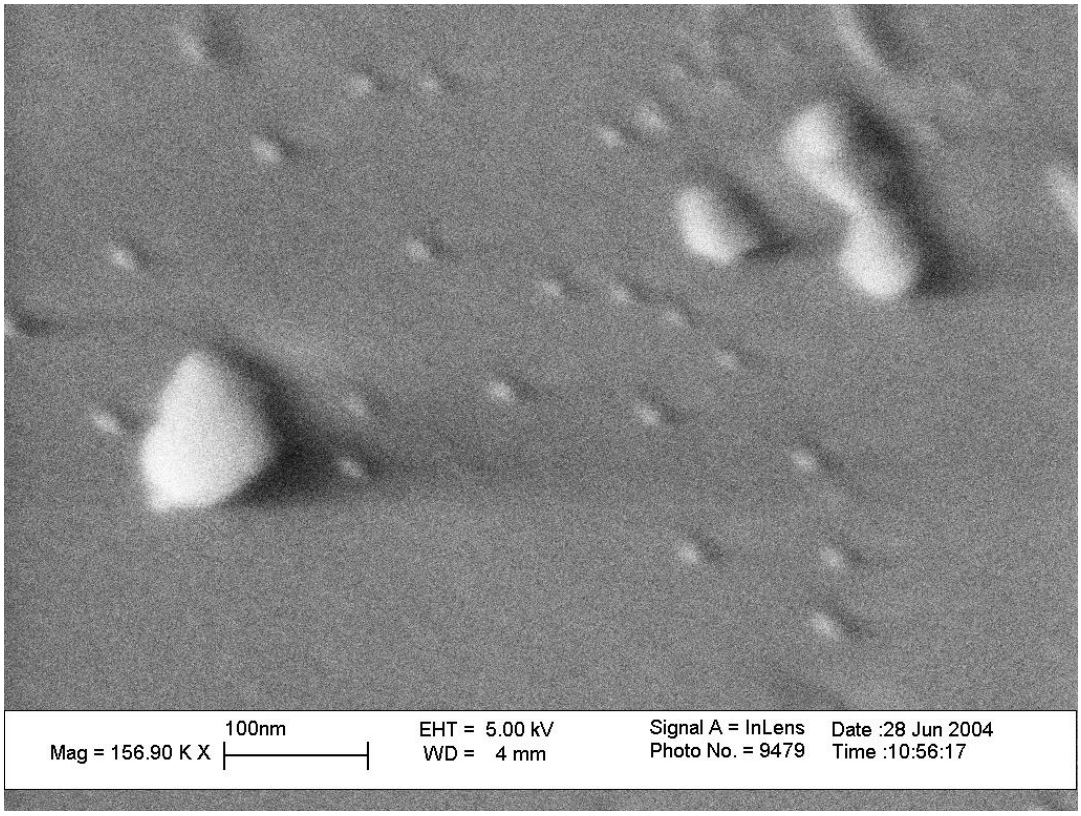

Figure 4.20 .0039 wt. % Ni after reduction to 500 ˚C (157 K X).

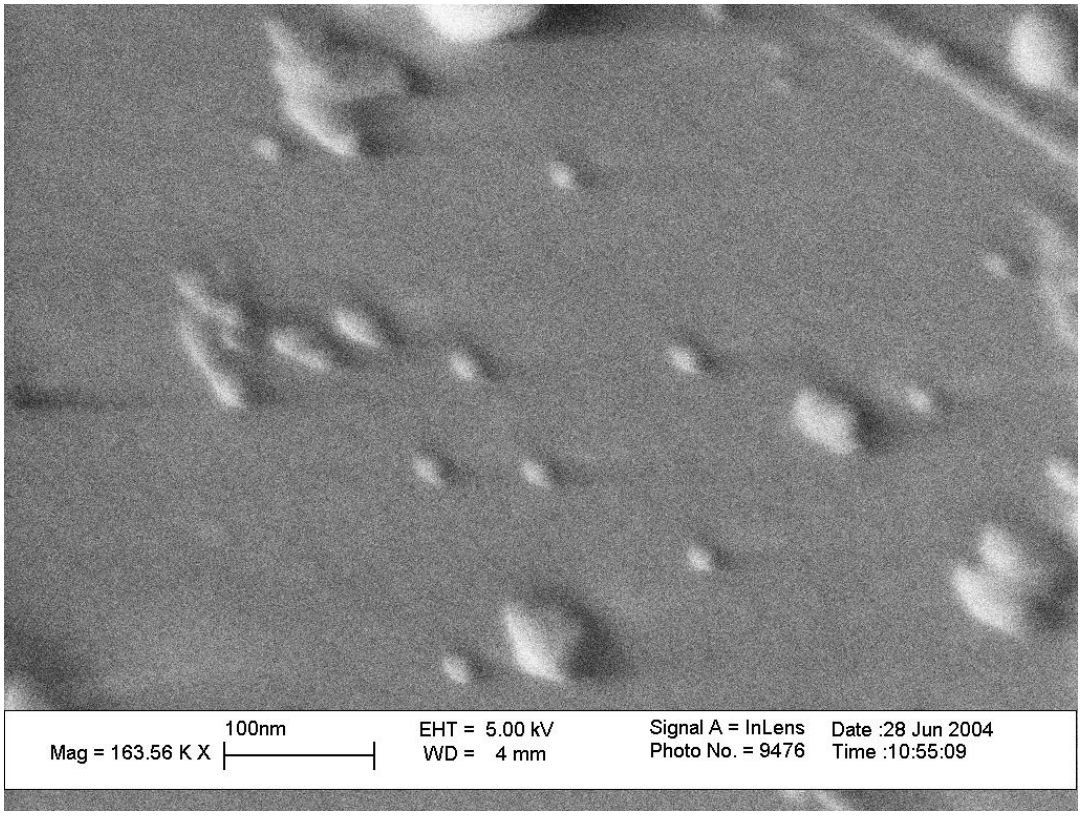

Figure 4.21 .0039 wt. % Ni after reduction to 500 ˚C (164 K X).

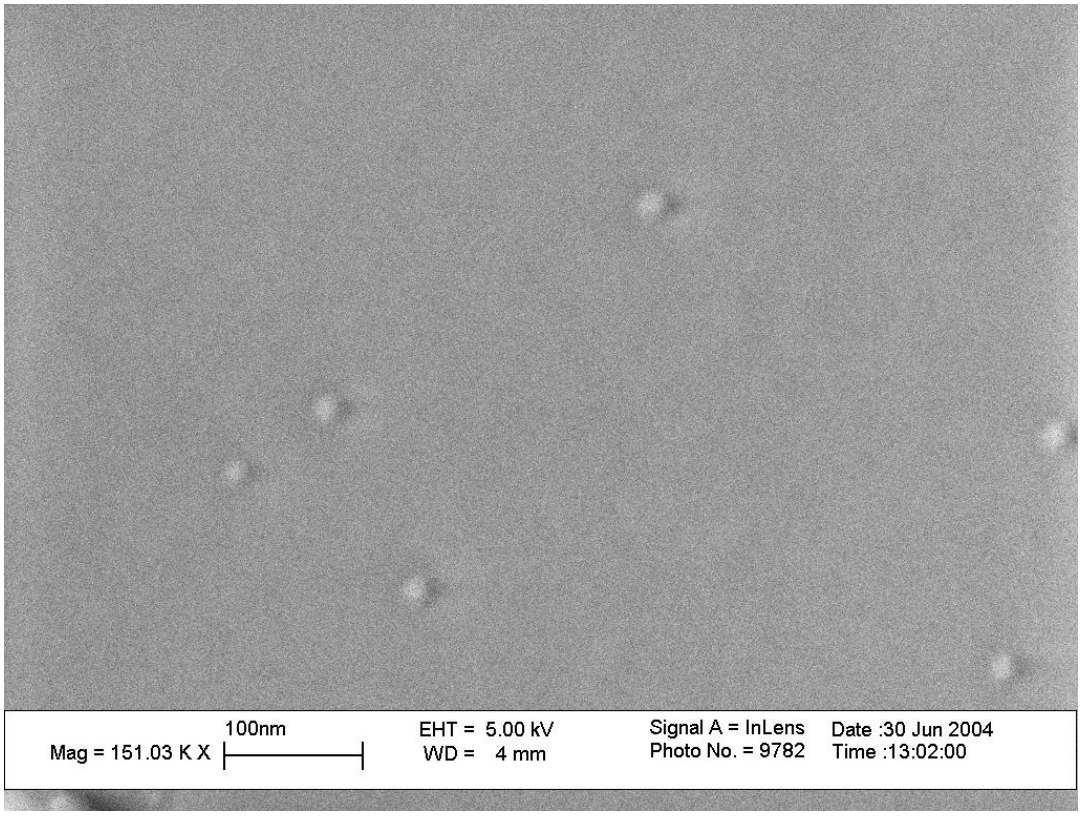

Figure 4.22 .0039 wt. % Ni after reduction to 500 ˚C (151 K X).

B. .0013 wt. % Ni

Catalyst samples were also prepared at .0013 wt. % Ni, and SEM was used to determine the crystallite size at various locations on the sample. Since this catalyst sample was made using a lower aqueous $NiCl_2$ concentration within the reverse micelles, it was expected that the nickel crystallites would be smaller than those of the .0039 wt. % catalyst due the lower number of Ni atoms available for nucleation. After the calcination stage, crystallites were found to have a size in the range of 8-12 nm. Therefore, good monodispersity was still observed for this sample. Figure 4.23 shows a micrograph of the .0013 wt. % Ni catalyst after calcination at 400 ˚C.

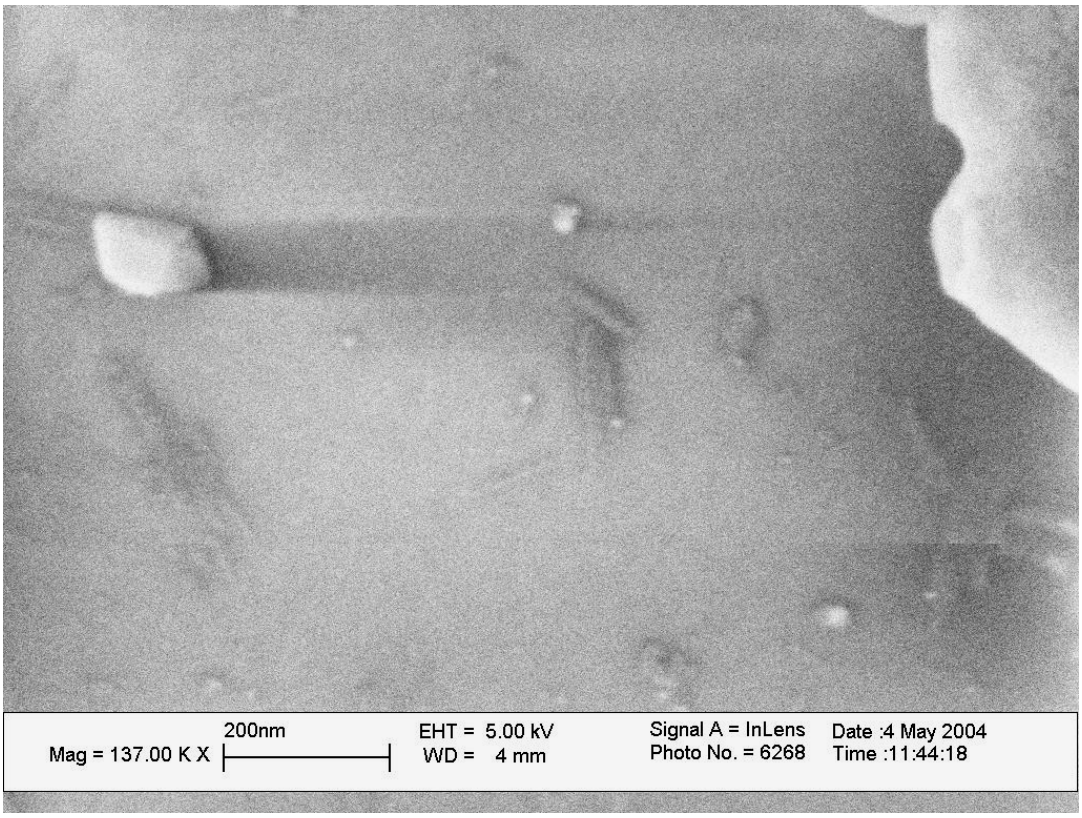

Figure 4.23 SEM image of .0013 wt. % Ni catalyst after calcination (137 K X).

Below are SEM images of the .0013 wt. % Ni catalyst after reduction to 500 ˚C. As can be seen, regions were found where the crystallites have clustered together. This same phenomena was also noticed for the .0039 wt. % Ni catalyst. In contrast to the catalyst precursor after calcination, the crystallites are in closer proximity to one another. Again, this may be caused by the occurrence of sintering at the higher reduction temperature of 500 ˚C. The crystallite size range is approximately 7-11 nm, with the estimate calculated from the reverse micelle size and Ni loading being 5 nm. Once again, a narrow particle size distribution is observed.

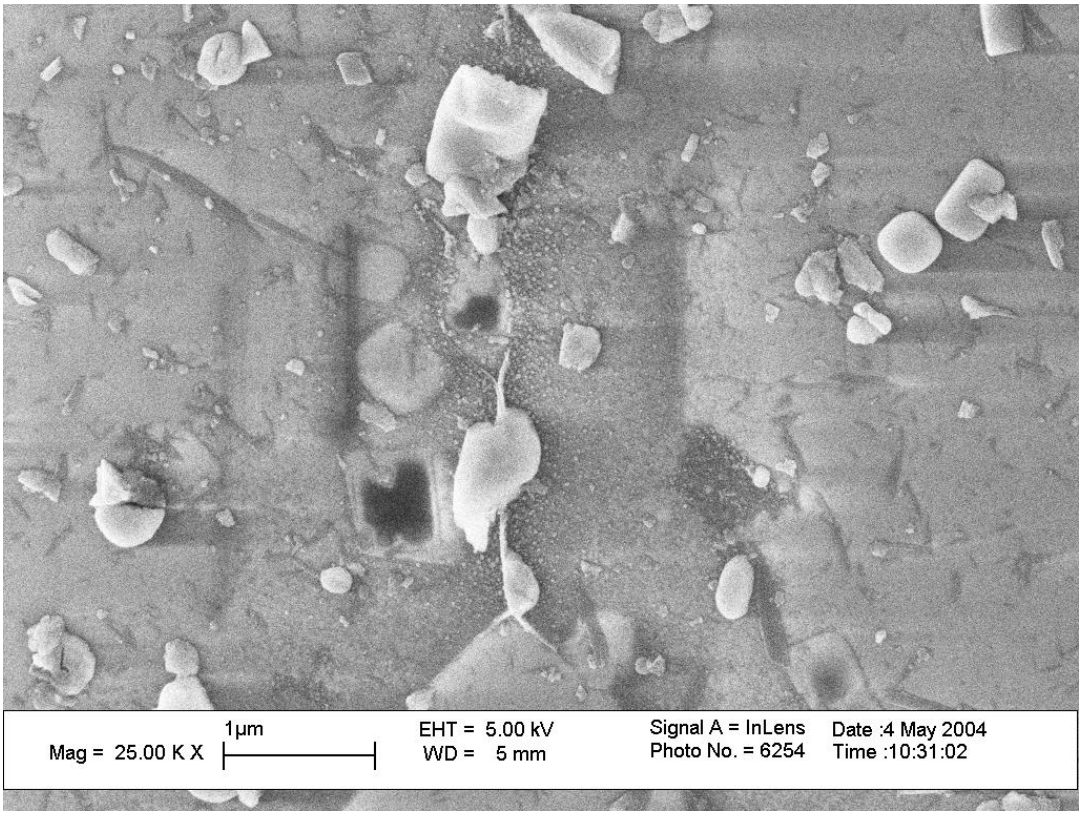

Figure 4.24 SEM image of .0013 wt. % Ni catalyst after reduction (25 K X).

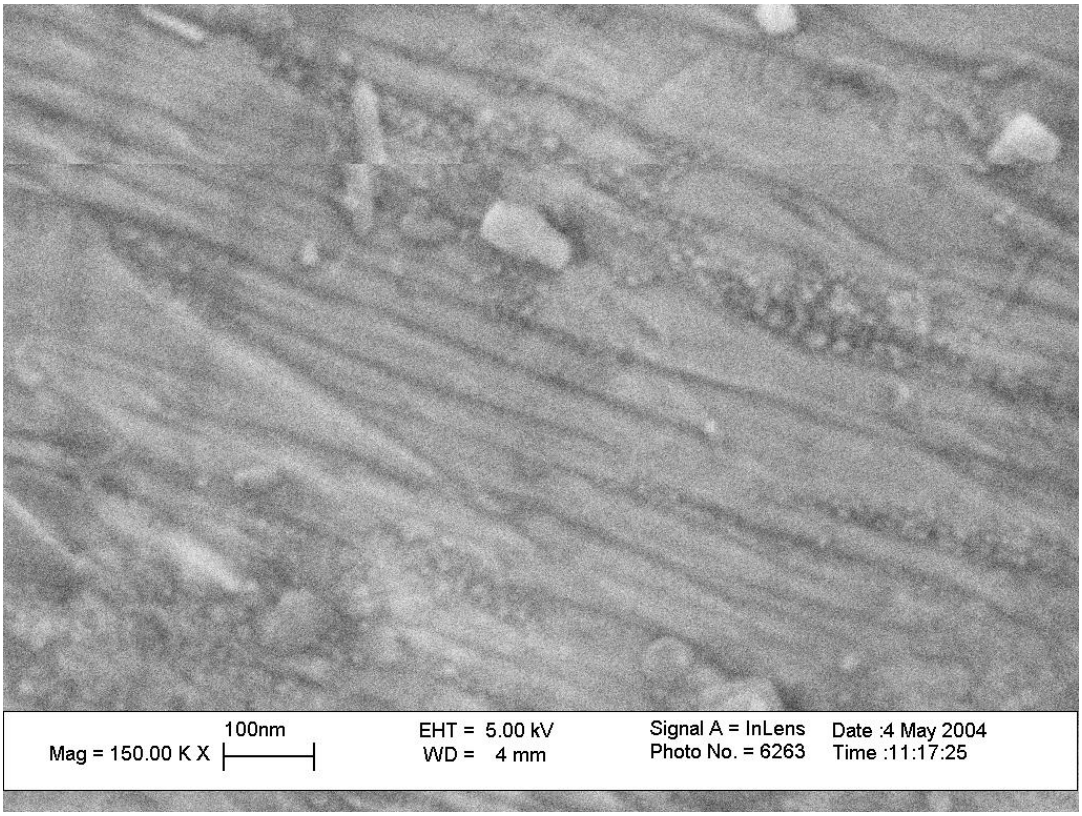

Figure 4.25 SEM image of .0013 wt. % Ni catalyst after reduction (150 K X).

C. .00039 wt % Ni

Lastly, catalyst samples prepared at .00039 wt. % Ni were analyzed using SEM. The following micrographs were taken after calcination at 400 ˚C and reduction to 500 ˚C. Although the size estimate for the crystallites based upon the reverse micelle size and Ni loading was 4 nm, SEM yielded a crystallite size of 8-12 nm after calcination and 5-9 nm after reduction, indicating good mono-dispersity. Once again, the images obtained after reduction show that the crystallites are closer together.

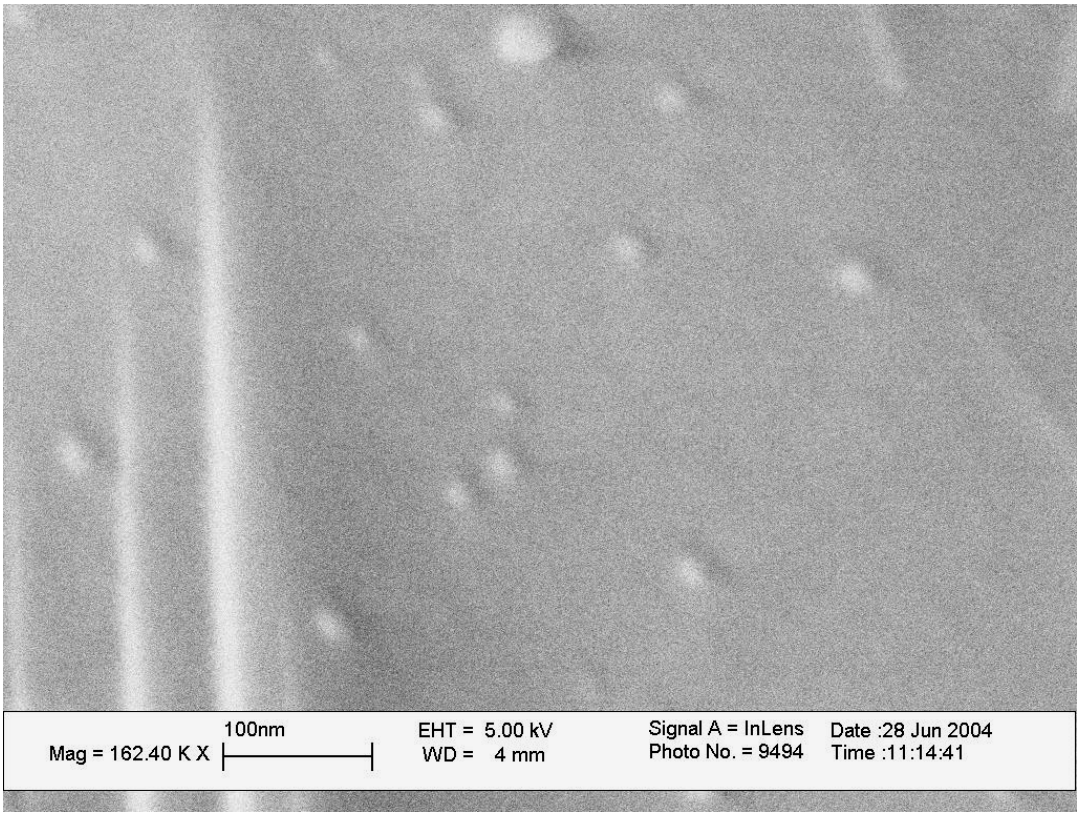

Figure 4.26 .00039 wt. % Ni after calcination (162 K X).

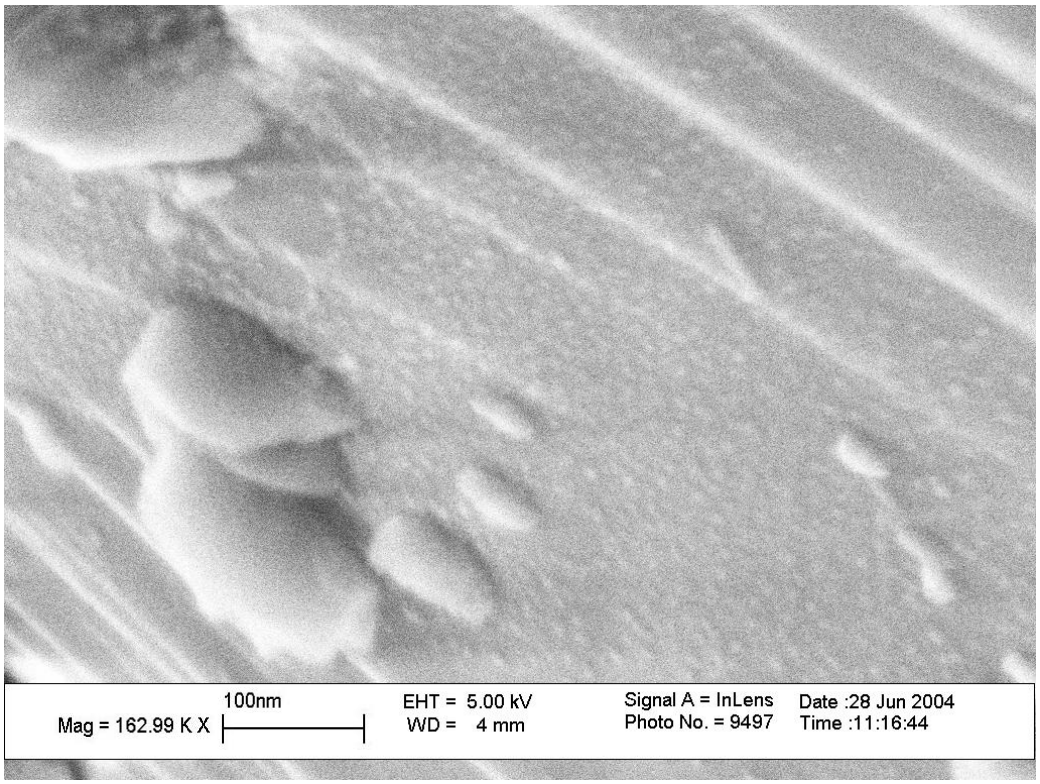

Figure 4.27 .00039 wt. % Ni after reduction (163 K X).

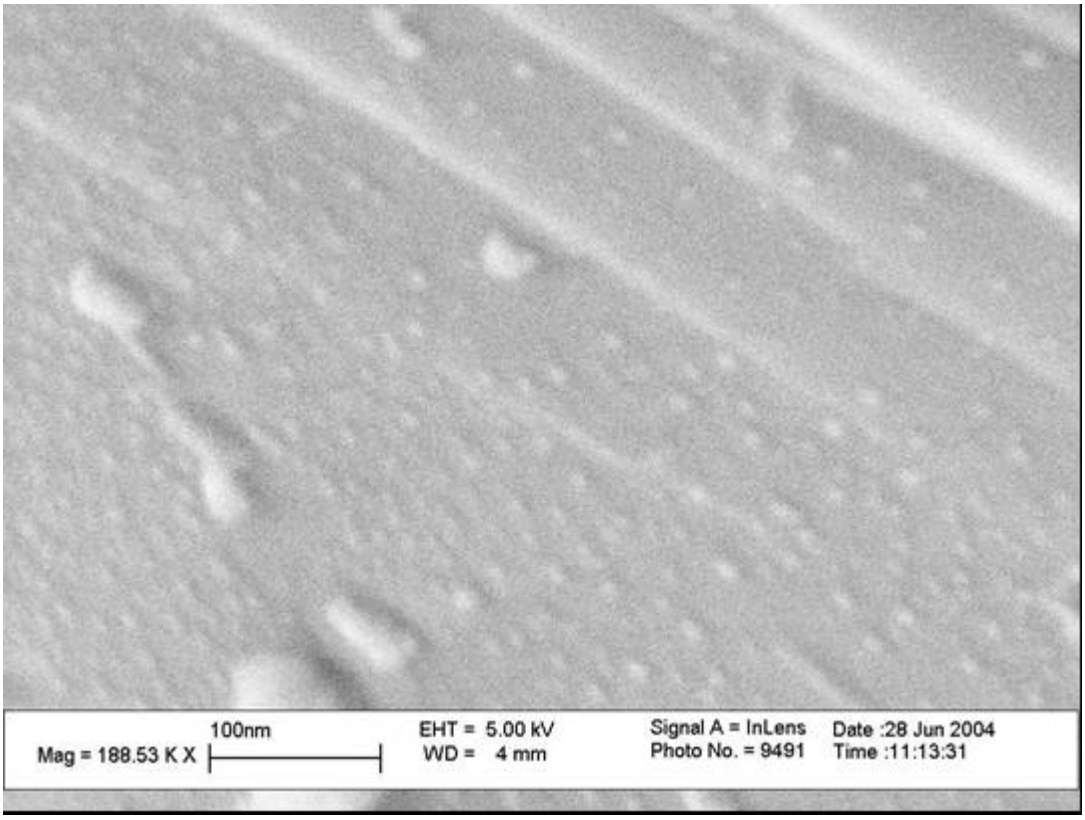

Figure 4.28 .00039 wt. % Ni after reduction (189 K X).

For the .039 wt. % catalyst precursor, SEM and EDS was used to verify that the microemulsion technique could be used to produce Ni nano-particles. This is shown by the Ni peaks shown in the EDS spectrums in Figures 4.11 and 4.15. In Figure 4.12, the Ni mapping overlaps most of the particles shown over the scanned area. Also, when comparing the Ni-deposited support to the plain alumina surface, one can see the addition of crystallites on the support surface. Furthermore, for the plain alumina surface, high quality images greater than 50 K X could not obtained due to the effects of charging. Solely due to the conductivity of the active metal deposited, the capability of gaining higher quality images at 100 K X and above for the catalyst precursors was greatly improved. This is evident in the images shown for the .0039, .0013, and .00039 wt. % Ni catalysts.

Using the reverse micelle size and known Ni loading, the crystallite size estimates provided a reliable basis upon which to gauge what the actual particle size would be when preparing Ni catalysts using the microemulsion technique. For the .0039 wt. % Ni catalysts, the estimate was 7 nm with SEM showing crystallite sizes in the range of 10-14 nm after reduction. SEM analysis revealed particle sizes in the range of 7-11 nm for the .0013 wt. % Ni catalysts, with the estimate being 5 nm. The .00039 wt. % Ni catalyst had crystallites in the size range of 5-9 nm, while the estimate was 4 nm. As discussed below, the discrepancy between the size estimate from micelle size and the size detected by SEM may be due to sintering effects. Table 4.3 gives the particle size results obtained for each catalyst.

Table 4.3 Crystallite sizes of the various catalyst samples.

Catalyst	Ni Metal Loading (wt. %)	Size Estimate (nm)	Size from SEM (nm)
B	0.0039	7	10-14
C	0.0013	5	7-11
D	0.00039	4	5-9

When compared to the images obtained for the catalyst precursors after calcination at 400 ˚C, it was noticed that the crystallites were closer together after reduction at 500 ˚C. Research done by Carter et. al. [7] has shown that in the temperature range of 370-700 ˚C the Ni surface area of a Ni/SiO_2 catalyst decreased because of the effects of sintering at elevated temperatures. From 370 ˚C to 700 ˚C, the crystallite size of their catalyst increased from 4 to 9 nm. Therefore, it is likely that the size discrepancy between the particle sizes detected by SEM and those estimated from preparation parameters may be due to sintering effects. This may also explain why particles after reduction are in closer proximity of one another.

Furthermore, one can see that microemulsion-prepared catalysts are better suited to study particles size effects than using catalysts prepared by incipient wetness or deposition-precipitation. Referring to Figures 2.3 and 2.6, a meshy network of crystallites is observed for catalysts prepared using traditional preparation techniques. Although these catalysts may be better suited for commercial purposes, the emulsion-prepared catalysts exhibit a better size distinction among batches of different Ni loading. Although the low wt. % of active metal for the emulsion-prepared catalysts would be

disadvantageous for commercial purposes, this catalyst seems to provide a model for studying catalytic structure-reactivity relationships.

4.3 REACTOR STUDIES

Ethane hydrogenolysis and ethylene hydrogenation reactions were conducted using the .0039, .0013, and .00039 wt. % Ni catalysts in order to determine particle size effects on catalytic activity. The following section gives the reaction results in terms of conversion, turnover number (*TON*) in molecules reacted/site/s and activation energy. The *TON* as a function of particle size was determined for both reactions and compared to the results obtained by other researchers.

4.3-1 Relation Between Particle Size and Dispersion

Dispersion is a measure of the fraction of metal atoms that comprise the surface of metal crystallites. Very small crystallites (< 1 nm) have all metal atoms as surface atoms and thus results in a dispersion of 1.0. Appendix A.2 presents the calculations for the dispersion of Ni crystallites of different sizes in the nano-range. Figure 4.29 shows the relationship between dispersion and particle size in the crystallite size range of 1-20 nm. Referring to Figure 4.29, one can see that the dispersion of a catalyst decreases as the particle size increases. Basically, the dispersion is equal to the inverse of the crystallite particle size of the catalyst. A catalyst with a high dispersion is advantageous in catalysis because a larger number of surface metal atoms are available as active sites during reactions. Therefore, the importance of crystallite size and its effects on the degree of metal dispersion are well known in the field of heterogeneous catalysis. Previous catalyst preparation research has shown that the amount of active metal loaded increases the crystallite size, thus decreasing the number of surface metal atoms [7]. The performance of catalysts is often expressed as *TON* because it normalizes the activity of catalysts on a

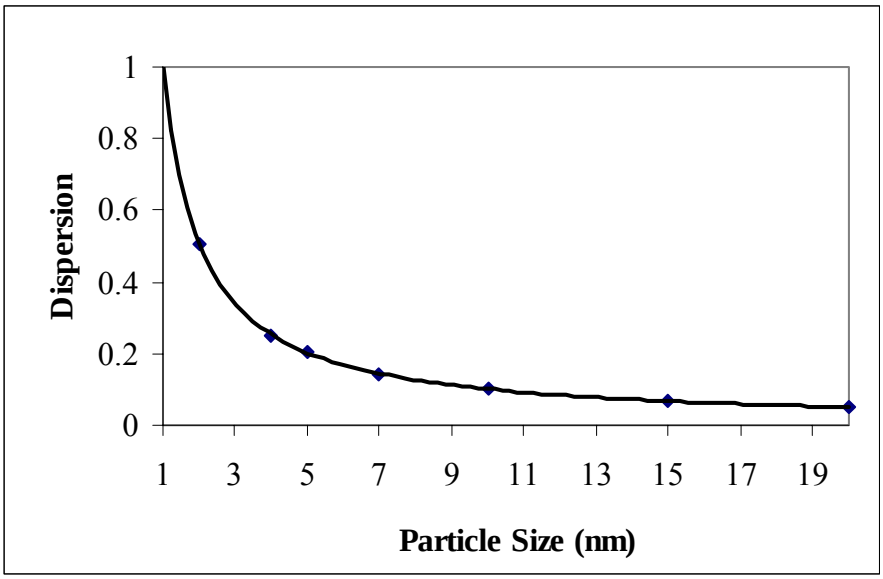

Figure 4.29 Dispersion as a function of particle size.

per unit metal surface atom basis. Thus, even though a catalyst may produce a higher conversion due to a higher wt. % of the active metal, it may not be efficient when compared to a lower wt. % Ni catalyst that has a higher degree of dispersion of the active metal. Since the goal of our research was to elucidate structure-reactivity relationships, the use of catalysts with a low active metal loading better suited our tasks of preparing nano-sized particles. These dispersion values were used to calculate the *TON* of the emulsion-prepared catalysts used for ethane hydrogenolysis and ethylene hydrogenation reactions.

4.3-2 Ethane Hydrogenolysis Studies

The three emulsion-prepared catalysts (.0039 wt. %, .0013 wt. %, and .00039 wt. % Ni) were studied for their ethane hydrogenolysis activity at 500˚C. The feed to the reactor consisted of 6 mole % C_2H_6, 54 mole % H_2, and balance He; a flow rate of 17 ml/min was used in all runs. Since the Ni metal loading was very small, several steps were undertaken to measure the catalytic activity: (i) the use of a larger catalyst bed, 1 gm, (ii) the use of a low feed flow rate to compensate for low activity as well as to minimize any pressure drop problems, and (iii) running at a higher temperature (500˚C) than those used in other literature studies. Figure 4.30 shows the transient profile for ethane conversion over a 3.5 hr. period for the .0013 wt. % Ni/Al_2O_3.

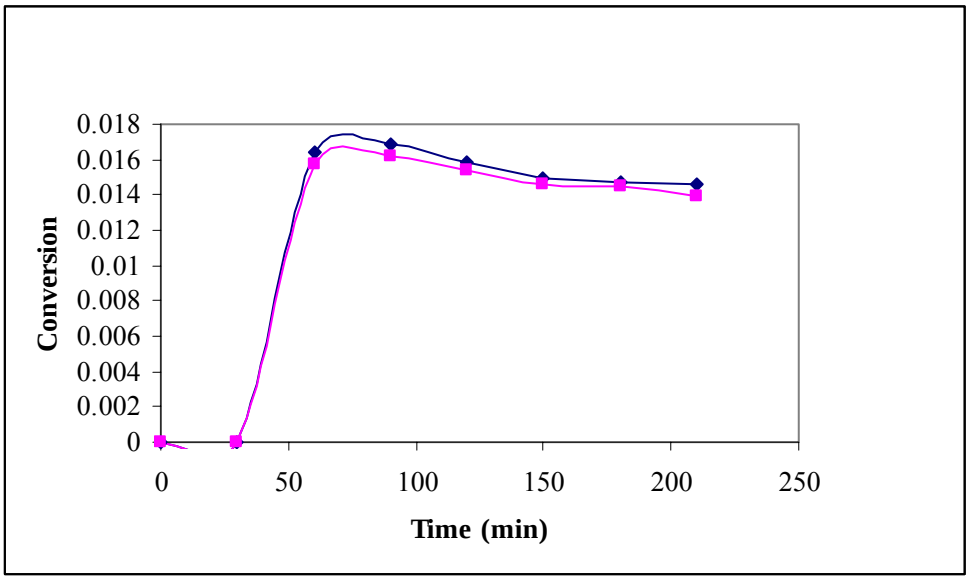

Figure 4.30 Transient profiles for ethane conversion over a 3.5 hr. period using the .0013 wt. % Ni/Al_2O_3. Two trials were run under the following conditions: feed – 6 mole % C_2H_6/54 mole % H_2/bal. He, total flow – 17 ml/min, and rxn. temperature - 500˚C.

There is not visible activity for the sample collected 30 min. after the reaction was initiated. It is not clear whether this induction period is an artifact of the low feed flow rate (and large volume of the gas flow lines), or whether it represents a true induction period for the surface reactions. The data presented in the literature for this reaction have omitted the initial activity behavior [8], and hence it remains a murky issue. The data points collected at 60 min. and 90 min. intervals show ~ 1.6-1.7 % conversion, and it can be considered to represent the activity of a fresh catalyst. In the following two hours, the ethane conversion dropped from 1.65 % to 1.5 %. This can be attributed to slow carbon buildup on the catalyst surface sites. Figure 4.31 shows the turnover number for the data shown in Figure 4.30

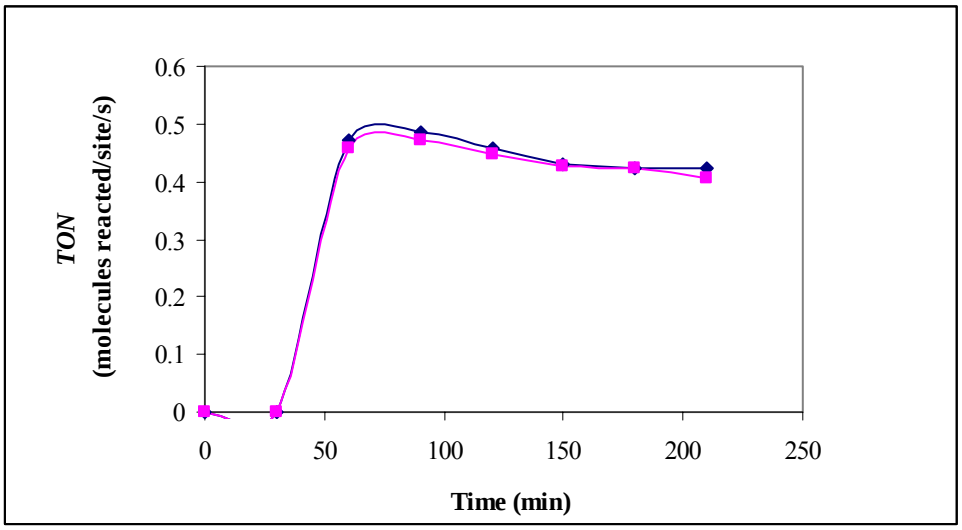

Figure 4.31 Transient profiles for TON over a 3.5 hr. period using the . 0013 wt. % Ni/Al_2O_3 during ethane hydrogenolysis. Two trials were run under the following conditions: feed – 6 mole % C_2H_6/54 mole % H_2/bal. He, total flow – 17 ml/min, and rxn. temperature - 500˚C.

The transient behavior for *TON* mimics that for the ethane conversion, as expected. In order to establish reproducibility of our experimental methods, all runs were repeated. Figures 4.30 and 4.31 show the data from two separate runs, conducted at identical conditions. Excellent agreement is seen between these two sets of data.

Figures 4.32 and 4.33 show the transient profiles for ethane conversion and *TON*, respectively, for all three catalysts used in this study. The transient profiles are qualitatively similar for the three catalysts, although the rate/extent of deactivation seems to vary from one catalyst to another. In general, at t = 90 min., the ethane conversion increases from 0.57% for 0.00039 wt. % Ni/Al_2O_3 to 2.3% for 0.0039 wt. % Ni/Al_2O_3 (Figure 4.32). However, as one looks at the activity in terms of *TON*, the *TON* is higher for the low Ni loading catalyst, which also happens to have the smallest Ni crystallites.

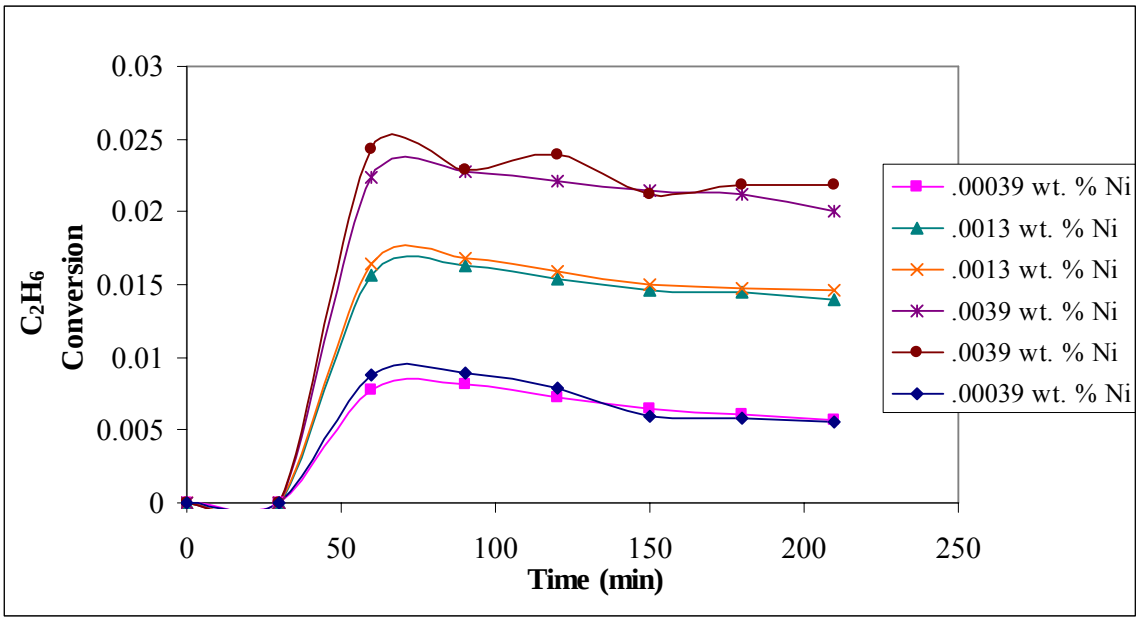

Figure 4.32 Transient profiles for ethane conversion over a 3.5 hr. period using all emulsion-prepared catalysts. Two trials were run for each catalyst under the following conditions: feed – 6 mole % C_2H_6/54 mole % H_2/bal. He, total flow – 17 ml/min, and reaction temperature - 500˚C.

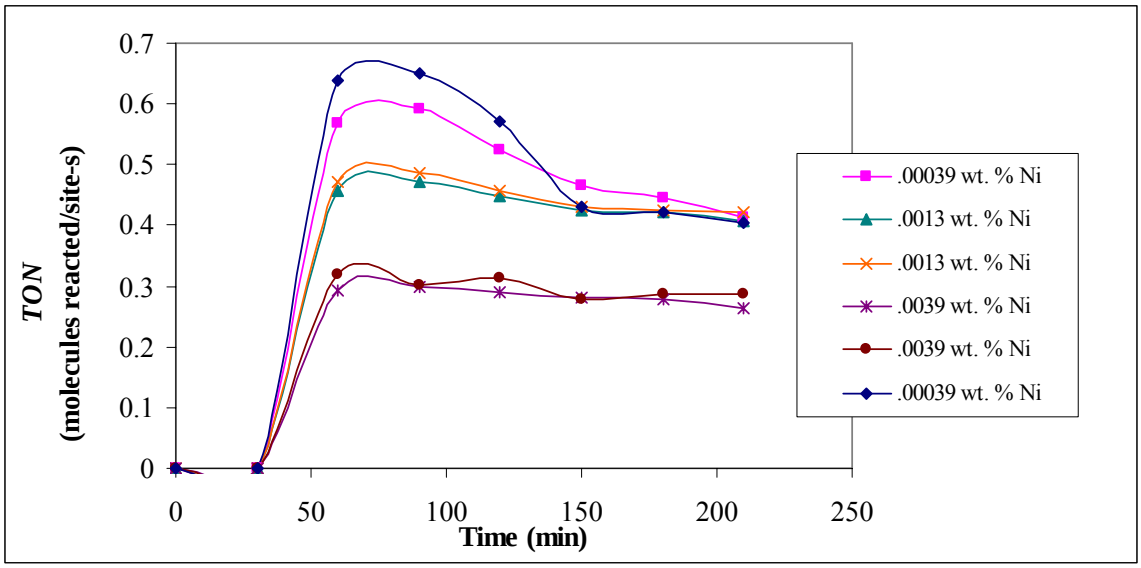

Figure 4.33 **Transient profiles for *TON* over a 3.5 hr. period using all emulsion-prepared catalysts in ethane hydrogenolysis. Two trials were run for each catalyst under the following conditions: feed – 6 mole % C_2H_6/54 mole % H_2/bal. He, total flow – 17 ml/min, and reaction temperature - 500˚C.**

In an effort to compare the activity for all three catalysts on the same basis, the *TON* values at the 90 min. duration were chosen to represent those over the fresh Ni surface. Figure 4.34 shows the *TON* values for ethane hydrogenolysis vs. particle size. *TON* average values are 0.62, 0.48, and 0.30, respectively, for the three catalysts.

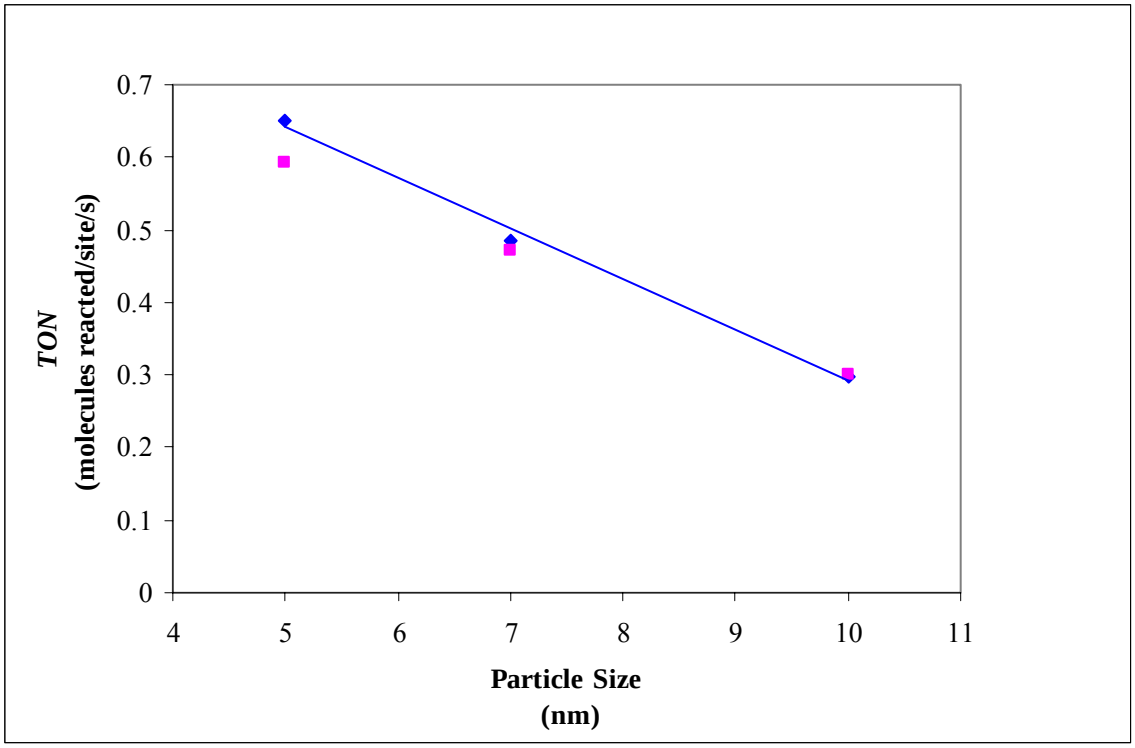

Figure 4.34 Ethane hydrogenolysis *TON* as a function of particle size (results from both runs included).

Referring to previous research conducted using ethane hydrogenolysis to study particle size effects on catalytic activity [7-11], the activity of catalysts composed of Ni metal clusters has been reported to decrease with increasing crystallite size in a larger extent than could be accounted for by the decrease in surface area. Based upon the earliest results obtained from Carter et al. [7] using ethane hydrogenolysis over Ni supported

catalysts, these particle sizes are in the range (> 4 nm) where the activity decreases with increasing particle size until a constant value is reached at a particle size of ~ 9 nm. Therefore, the results of this work verify that in the range of 4-10 nm, the catalytic activity decreases with increasing particle size due to intrinsic effects in which smaller particles may exhibit the chemical properties necessary for a higher activity. In terms of activity, comparisons between single-crystal data and conventional catalysts have shown that smaller particles are comparable to the Ni(100) surface and larger particles to the Ni(111) surface [10]. This supports the notion that crystallites of different sizes have different structural properties that may promote alternate reaction paths for ethane hydrogenolysis.

Using the .0039 wt. % Ni catalyst, the reaction temperature was also varied ± 25 ° C in order to determine temperature effects for the hydrogenolysis reaction. Using the Arrhenius equation described in Section A.3, the temperature-dependence data was used to determine the activation energy, E_a, of the reaction. The effect of temperature on catalytic activity is shown in Figures 4.35 and 4.36.

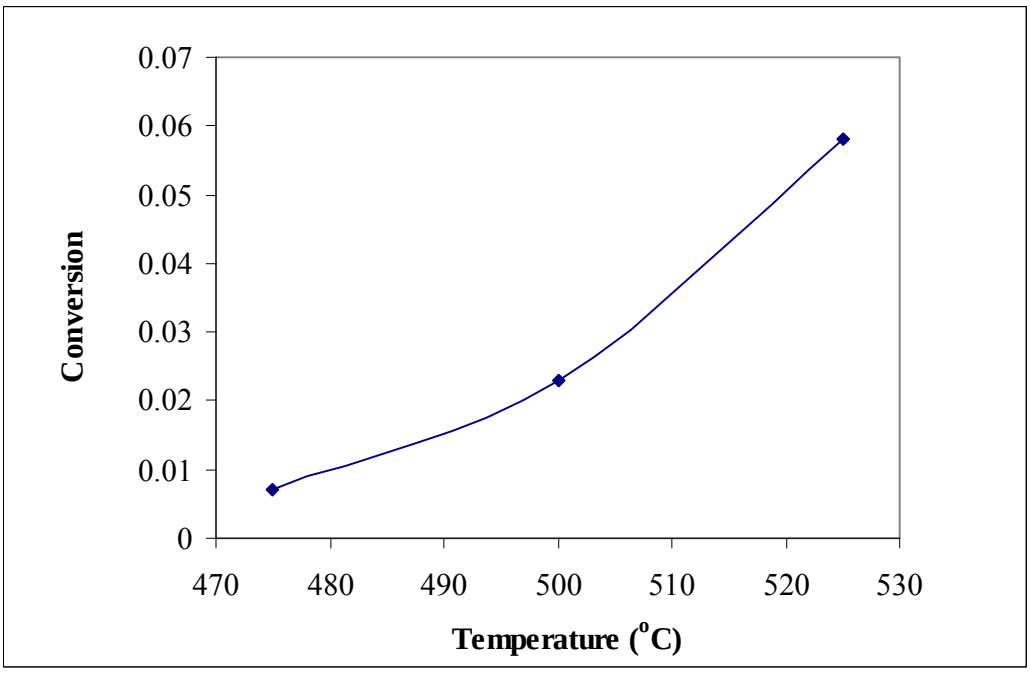

Figure 4.35 Ethane conversion vs. temperature at *t* = 90 min. using the 0.0039 wt. % Ni catalysts. Other reaction conditions remained the same.

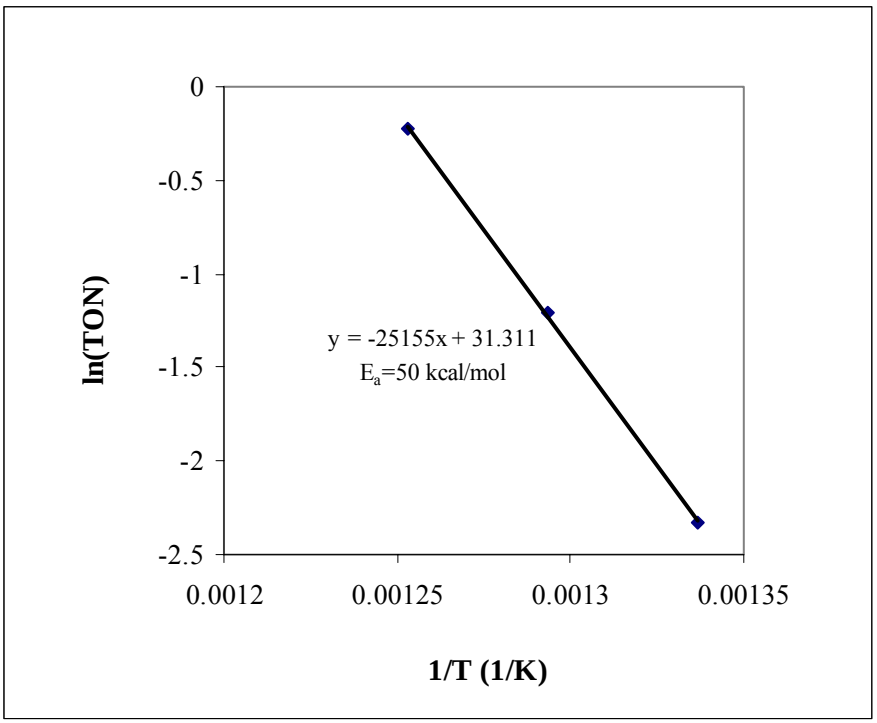

Figure 4.36 Arrhenius plot for ethane hydrogenolysis reaction using 0.0039 wt. % Ni/Al_2O_3. Plot based upon data shown in Figure 4.35.

The Arrhenius plot shown in Figure 4.36 was constructed using the temperature-dependence data shown in Figure 4.35. The activation energy was found to be approximately 50 kcal/mol, and this value is close to the value associated with that of the Ni(111) surface, which is 46 kcal/mol [10]. As previously discussed, single crystal studies have shown that larger Ni particles (> 4 nm) exhibit activity similar to that over the Ni(111) surface. In contrast, for Ni particles 1-3 nm in size, research has shown that the apparent activation energy for ethane hydrogenolysis on these particles is similar to the reported value on Ni(100) (24 kcal/mol) [10] Therefore, the 0.0039 wt. % Ni catalyst exhibits activity that is comparable to that observed from single crystal studies of the Ni(111) surface. Ultimately, for ethane hydrogenolysis, Ni crystallites sizes in the range of 1-3 nm have structural properties similar to that of the Ni(100) surface, while larger particles are structurally similar to the Ni(111) surface.

4.3-3 Ethylene Hydrogenation Studies

The ethylene hydrogenation reaction was also conducted using the emulsion-prepared catalysts in order to elucidate particle size effects on catalytic activity. The feed to the reactor consisted of 6 mole % C_2H_6, 54 mole % H_2, and balance He; a flow rate of 83 ml/min and reaction temperature of 120˚C were used in all runs. Using the .00039, .0013, and .0039 wt. % Ni catalysts, two runs were made for each catalyst in order to establish the reproducibility of results. Figures 4.37 and 4.38 show the ethylene conversion and *TON* as a function of time. Both the conversion and the *TON* profiles stay relatively flat after 60 minutes. Presumably, the carbon deactivation rates are very low at 120˚C. Figure 4.37 shows that ethylene conversion increases with Ni loading.

However, in terms of *TON*, one can see from Figure 4.38 that the activity does not change significantly. At t = 90 min., the average turnover numbers were 15, 17, and 14 for the 0.00039, 0.0013, and 0.0039 wt. % Ni catalysts, respectively. In contrast to the ethane hydrogenolysis results, the catalytic activity of the emulsion-prepared catalyst is not affected by the crystallite size, and thus is structure-insensitive. These results are comparable to those of McCrea and Somorjai in which the rate of reaction was found to be 11±1 and 12±1 molecules per site per second for Pt(111) and Pt(100), respectively.

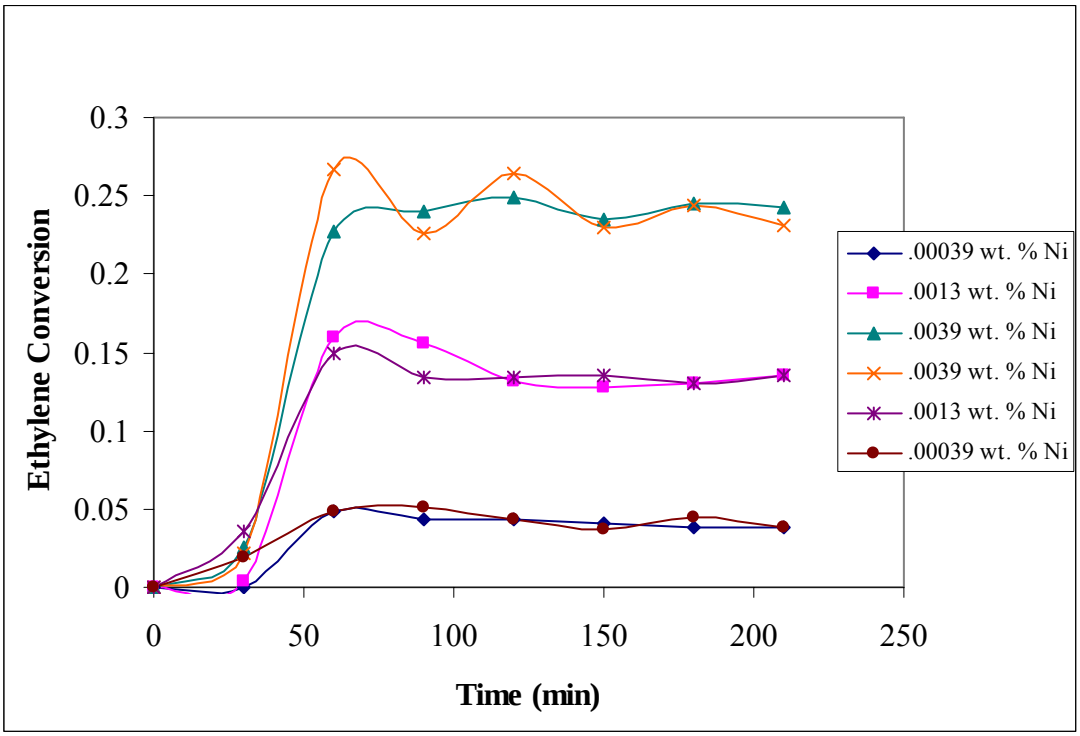

Figure 4.37 Transient profiles for ethylene conversion over a 3.5 hr. period using all emulsion-prepared catalysts. Two trials were run for each catalyst under the following conditions: feed – 6 mole % C_2H_6/54 mole % H_2/bal. He, total flow – 83 ml/min, and reaction temperature - 120˚C.

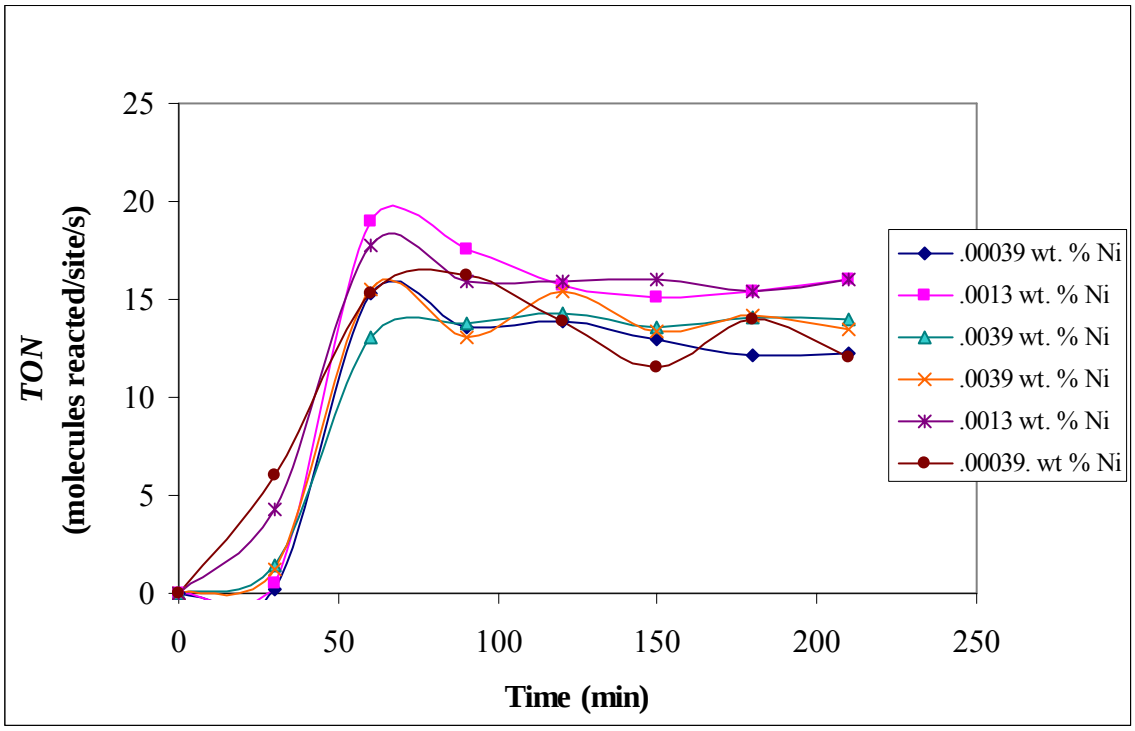

Figure 4.38 **Transient profiles for *TON* over a 3.5 hr. period using all emulsion-prepared catalysts in ethylene hydrogenation. Two trials were run for each catalyst under the following conditions: feed – 6 mole % C_2H_6/54 mole % H_2/bal. He, total flow – 83 ml/min, and reaction temperature - 120˚C.**

Using the .0039 wt. % Ni catalyst, the reaction temperature was also varied ± 25 ˚C in order to determine temperature effects on catalytic activity and to get an estimate of the reaction activation energy. Figures 4.39 and 4.40 show the temperature dependence of ethylene hydrogenation over the 0.0039 wt. % Ni catalyst in the range of 95-145˚C. As expected the conversion and reaction rate increase with temperature. From a temperature of 95 ˚C to 120 ˚C, the *TON* increased from a value of 1.4 to 14, resulting in a ten-fold rise in reaction rate. The *TON* also increased from 14 to 35 (a rise by a factor of 2.5) as the reaction temperature was changed from 120 ˚C to 145 ˚C. Therefore, although raising the temperature increases the reaction rate in the range of 95-145 ˚C, the rate of increasing activity decreases with increasing temperature. Figure 4.40 is an Arrhenius plot for ethylene hydrogenation over the 0.0039 wt. % Ni catalyst. The activation energy was found to be 20 kcal/mol.

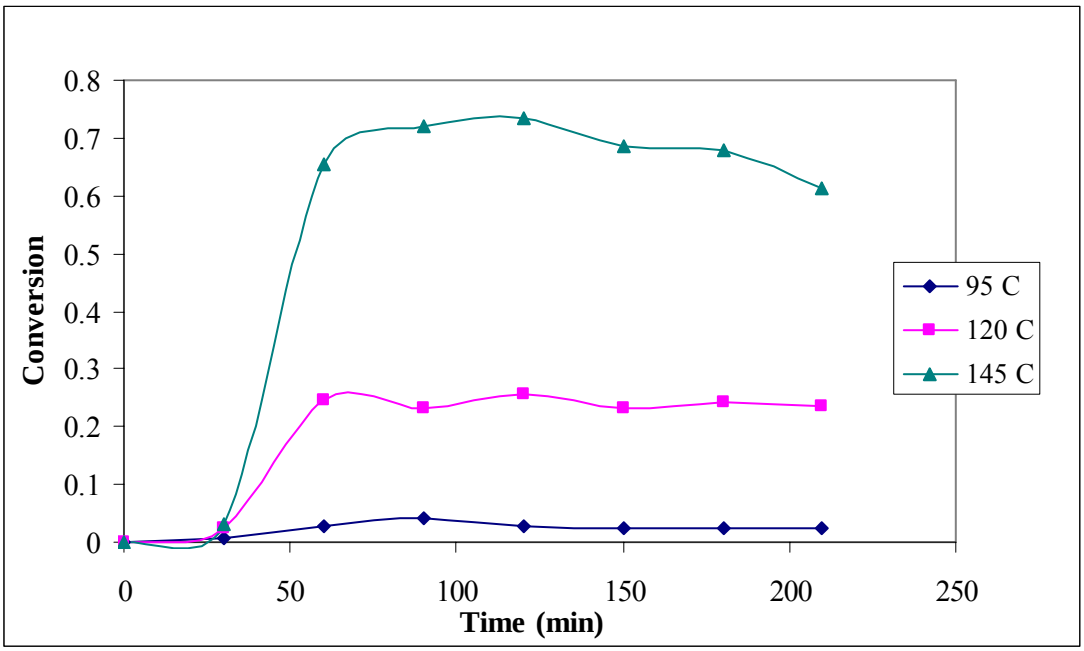

Figure 4.39 Ethylene conversion vs. time at several reaction temperatures for hydrogenation over 0.0039 wt. % Ni/Al_2O_3.

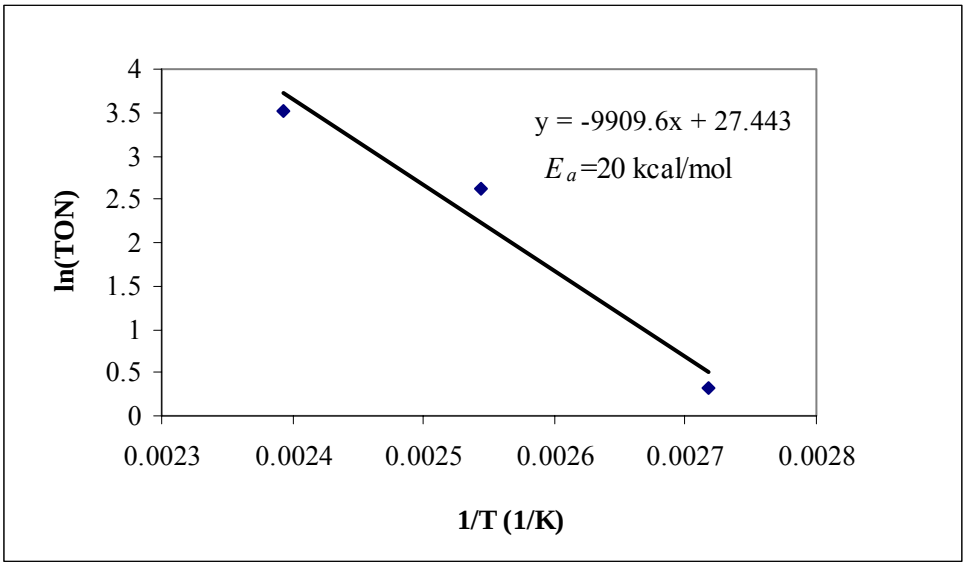

Figure 4.40 Arrhenius plot for ethylene hydrogenation reaction using 0.0039 wt. % Ni/Al_2O_3. Plot based upon data shown in Figure 4.39.

Figure 4.41 shows the effects of Ni crystallite size on ethylene hydrogenation activity. As one can see, the *TON* does not change significantly as a function of particle size. The largest change noted in *TON* is from 14 at 5 nm to 17 at 7 nm, a rise by only a factor of 1.2. In contrast, referring to Figure 4.34 for ethane hydrogenolysis, the largest change in *TON* is from 0.65 at 5 nm to 0.30 at 10 nm (over a double decrease). Because the structural properties of Ni crystallites are known to change with particle size, one can see that ethylene hydrogenation is structure-insensitive as evidenced by its nearly constant activity as a function of particle size.

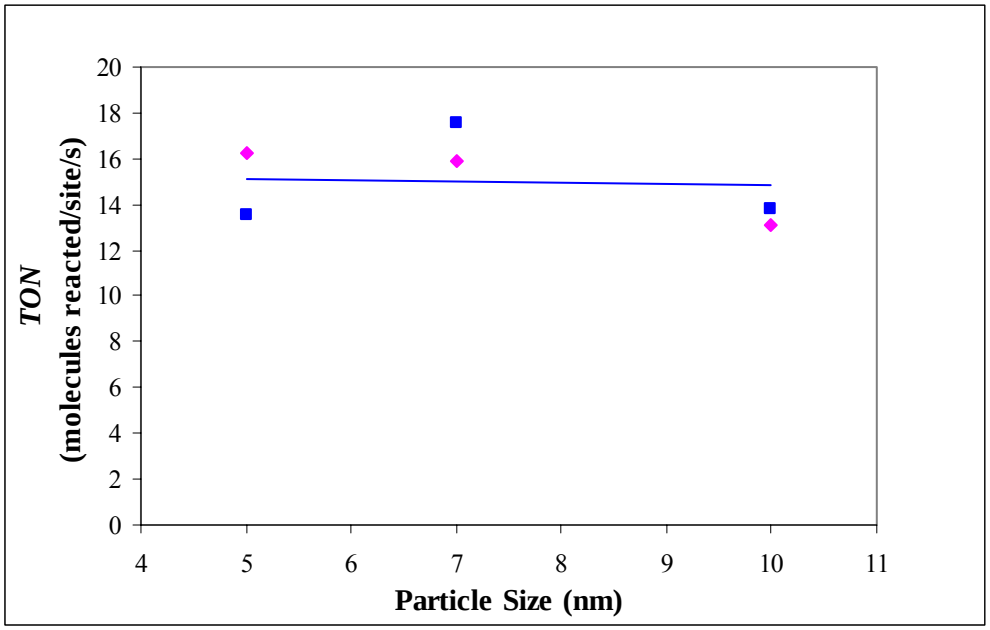

Figure 4.41 Ethylene hydrogenation *TON* as a function of particle size (results from both runs included).

Figure 4.42 shows the particle size effects on the catalytic activity of hydrogenolysis and hydrogenation reactions. For ethane hydrogenolysis, the activity decreases with increasing particle size. This may be due to the intrinsic particle size effects discussed in Section 2.3-1. These results verify that ethane hydrogenolysis is a structure-sensitive reaction and that crystallites of smaller sizes exhibit chemical properties or crystal facets that are favorable in promoting a higher rate of reaction. The ethylene hydrogenation reaction rate is relatively constant as a function of particle size. Thus, these results help confirm the structure-insensitivity of the reaction. The larger average turnover numbers for ethylene hydrogenation (13 for the .0039 wt. % Ni catalyst) as compared to those for ethylene hydrogenation (0.23 for the .0039 wt. % Ni catalyst) further prove that the reaction is not affected by various crystallite structure properties.

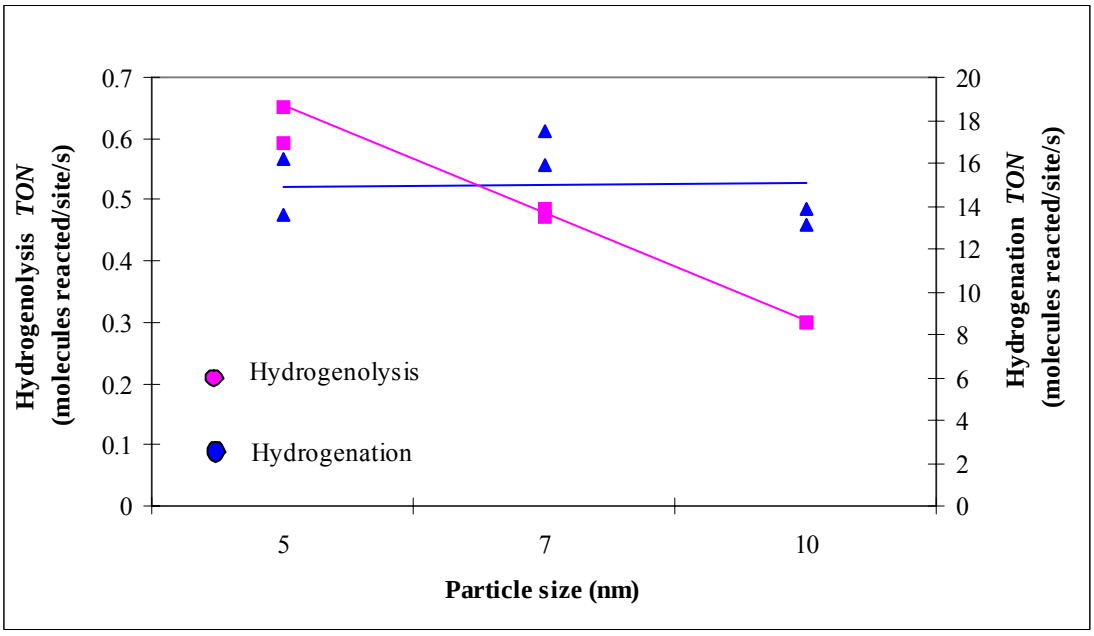

Figure 4.42 Particle size effects for hydrogenolysis and hydrogenation reactions at a reaction time of 90 minutes.

CHAPTER 5

CONCLUSIONS AND RECOMMENDATIONS

The results of this study have demonstrated that when using the hexanol to water ratio, *O/A*, and the water to surfactant ratio, W_o, as variables, it is possible to prepare reverse micelles that vary in polydispersity, stability, and size. It was determined that the *O/A* ratio of 2 and the W_o value of 10 provided reverse micelles with the lowest polydispersity and good stability, as well as the size of interest. The size of reverse micelles was found to increase linearly with increasing W_o, but using that variable to change crystallite size would have yielded metal clusters much larger than the desired range (2-10 nm). Besides, using higher values of W_o had an adverse effect on the stability of the reverse micelles. Therefore, varying the metal salt concentration within the reverse micelles seemed to be the best method of changing the Ni particle size in the nano-range once optimal values of W_o and *O/A* were determined. Changing the aqueous metal salt concentration was shown not to significantly affect the micelle size or polydispersity.

Procedures were developed to support these reverse micelles on silica plates, as well as non-porous α-alumina powder. Appropriate treatment (temperature and time) to dry, calcine, and reduce the Ni particles was necessary to translate mono-dispersed reverse micelles to mono-dispersed Ni clusters. Using high loadings of emulsion and/or high temperatures would inevitably lead to agglomeration and sintering of metal particles. SEM analysis of supported metal clusters proved useful in understanding the process of forming polydispersed clusters. Three catalysts with different Ni loadings

(0.00039 wt. %, 0.0013 wt. %, and 0.0039 wt. %) on α-Al_2O_3 were prepared and verified to be mono-dispersed. From SEM analysis of the catalyst precursors before and after reduction, one can clearly see the effects of sintering at the higher reduction temperature of 500 ˚C. Before reduction, the crystallites have adequate spacing between them. After reduction, the particles are in closer proximity to one another in certain locations on the support surface. One can conclude that surface migration at the elevated reduction temperature results in the formation of cluster-like active Ni. The actual crystallite sizes detected from SEM are slightly higher than those predicted using the reported reverse micelle diameter and known aqueous $NiCl_2$ concentration. This phenomenon may be the result of sintering.

These three catalysts were tested for their activity for ethylene hydrogenation and for ethane hydrogenolysis. The results obtained are in agreement with those reported in the literature, i.e., ethylene hydrogenation is a facile or structure-insensitive reaction, whereas ethane hydrogenolysis is a demanding or structure-sensitive reaction. This study supports the findings made using single crystal surfaces. This work shows that emulsion-prepared catalysts provide an adequate model for studying particle size effects of both demanding and facile reactions.

It is clear from the present study that the protocols for supporting reverse micelles or small metal clusters onto a porous support need to be developed much further if it is to serve as a basis for the preparation of commercial catalysts. This technique has a great potential for preparing multi-component catalytic sites. This can be used to prepare well-defined compositions of bimetallic clusters as well as promoted catalysts. This

preparation technique opens up an entire spectrum of possibilities for studying new catalytic systems.

This study had limited success in preparing Ni clusters smaller than 5-6 nm. This limitation was caused primarily by the low surface area of α-Al_2O_3 because that restricted the amount of Ni loading. Reducing the $NiCl_2$ concentration in the aqueous phase further would make it even harder to conduct reactor studies. It would be very desirable to vary the protocols with several porous supports (macropores larger than 70-80 nm) or amorphous, non-porous silica, for example. In the same vain, different pairs of organic media and surfactants might lead to the formation of smaller, yet stable, reverse micelles. Future efforts in the direction would be fruitful. Lastly, other demanding and facile reaction types, such as cracking, isomerization, partial oxidation, and oxidative hydrogenation, could also be investigated to determine if similar particle size effects hold true for different reactions.

APPENDIX A

PERTINENT CALCULATIONS

A.1 Calculation of Crystallite Size

Using the average micelle diameter obtained from dynamic light scattering, an estimate of the nickel nano-particle size could be derived in the following manner. From the micelle diameter, the volume of the micelle can be calculated using the following equation:

$$V_m = 1/6\pi d_m^3 \qquad \text{(A.1)}$$

where V_m is the micelle volume and d_m is the average micelle diameter. Because the content of the micelle is an aqueous solution of $NiCl_2$, one can assume that the volume of the micelle in cubic centimeters is approximately the mass of the micelle in grams. The mass of the micelle contents multiplied by the weight percent Ni yields the Ni mass within each micelle. Dividing the Ni mass by its molecular weight yields the number of gatoms of Ni within each micelle. Upon dividing the number of Ni moles by Avogadro's number, 6.02×10^{23}, the number of Ni atoms in each micelle can be obtained.

The volume of a cubic Ni lattice (fcc structure) is 43.6 $Å^3$ [36]. Because four Ni atoms contribute to each Ni lattice, the volume per Ni atom is equal to the total lattice volume divided by four. Therefore, the volume occupied by each Ni atom in the lattice is approximately 10.9 $Å^3$. Multiplying 10.9 $Å^3$ by the number of Ni atoms in each micelle yields an estimate of the total Ni atom volume in a micelle. Assuming that the Ni crystallite is present on the support surface as a hemisphere, the total number of Ni atoms in each micelle can be equated to a Ni cluster size. Using this correlation, an estimate of

the diameter of a nickel crystallite formed from the Ni atoms can be calculated as follows:

$$1/12\pi d_c^3 = \text{Ni atom volume} \qquad \text{(A.2)}$$

$$d_c = (12/\pi * \text{Ni atom volume})^{1/3} \qquad \text{(A.3)}$$

where d_c is the estimated nickel nano-particle diameter.

A.2 Dispersion Calculation

Dispersion is defined as the ratio of surface metal atoms to the total metal atoms within a metal cluster. For a given metal cluster of a certain size dispersed over a support, the dispersion of the active metal can be calculated in the following manner. Let d_c be the diameter of the crystallites in cm. The volume of the Ni crystallite can be calculated using the equation for the volume of a sphere, which is given below:

$$V_c = 1/6\pi d_c^3 \qquad \text{(A.4)}$$

Multiplying the volume of the micelle by the density of Ni, which is 8.9 g/cm^3, yields the weight of the crystallite in grams. Multiplying the Ni weight by Avogadro's number, 6.02x10^{23}, and dividing by the molecular weight of Ni, 58 g/gatoms, yields the total number of Ni atoms in a crystallite of size d_c. The surface area, A_c, of the Ni crystallite can be calculated from the following equation:

$$A_c = \pi d_c^2 \qquad \text{(A.5)}.$$

The area of one Ni atom is 6.5 $Å^2$ (based on an average of the three low index planes) [7]. Dividing the crystallite surface area, A_c, by 6.5 $Å^2$ yields the total number of surface Ni atoms. The dispersion is calculated by dividing the number of surface Ni atoms by the total number of Ni atoms in the crystallite.

A.3 Arrhenius Rate Law

The temperature dependence of the specific reaction rate, k, can be correlated using the Arrhenius equation. The equation is given by the following:

$$k(T) = Ae^{-Ea/RT} \qquad \text{(A.6)}$$

where A = preexponential factor or frequency factor,

E_a = activation energy, J/mol or cal/mol,

R = gas constant = 8.314 J/mol·K = 1.987 cal/mol·K, and

T = absolute temperature, K [6].

The activation energy can be determined experimentally by carrying out a certain reaction at several temperatures. After taking the natural logarithm of Equation (A.6), the following form of the Arrhenius equation is obtained:

$$\ln k = \ln A - (E_a/R)(1/T) \qquad \text{(A.7)}.$$

Therefore, a plot of ln$k$ versus $1/T$ should be a straight line whose slope is equal to E_a/R.

REFERENCES

1. Ponec, V., Bond, G.C. *Catalysis by Metals and Alloys.* **95**: 320 (1995).

2. Barnickel, P., Wokaun, A., Sager, W., Eicke, H.F., *J. Coll. Inter. Sci.,* **148(1)**: 80-90 (1992).

3. Qiu, S., Dong, J., Chen, G., *J. Colloid Interface Sci.* **216**: 230-234 (1999).

4. Goodman, D.W., *J. Vac. Sci. Tech***., 20(3)**: 522-526 (1982).

5. Boutonnet, M., Kizling, J., Stenius, R., *Colloids and Surfaces.* **5:** 209-225 (1982).

6. Fogler, H.S. *Elements of Chemical Reaction Engineering.* 3rd ed. New Jersey: Prentice Hall.,(2000).

7. Carter, J.L., Cusumano, J.A., Sinfelt, J.H., *J. Phys. Chem.,* **70:** 2257-2263 (1966).

8. St. Clair, T.P., Goodman, D.W., *Top. Cat.,* **13:** 5-19 (2000).

9. Rainer, D.R., Xu, C., Goodman, D.W., *J. Molec. Cat. A: Chem., **119:*** 307-325 (1997).

10. Coulter, K., Xu, X., Goodman, D.W., *J. Phys. Chem.,* **98:** 1245-1249 (1994).

11. Santra, A.K., Goodman, D.W., *J. Phys.: Condens. Matter,* **14:** R31-R62 (2002).

12. Chang, F.W., Kuo, M., Tsay, M., Hsieh, M., *Appl. Cat. A,* General **247:** 309-320 (2003).

13. Moffat, J.B., *Theoretical Aspects of Heterogeneous Catalysis.* New York: Van Nostrand Reinhold, (1990).

14. Chang, F.W., Tsay, M., Liang, A., *Appl. Cat. A,* General **209:** 217-227 (2001).

15. Chang, F.W., Hsiao, T.J., Shih, J.D., *Ind. Eng. Chem. Res.,* **37 (10):** 3838-3845 (1998).

16. Rosen, M.J., *Surfactants and Interfacial Phenomena.* New York: Wiley (1978).

17. Dadyburjor, D.B., Fout, T.E., Zondlo, J.W., *Cat. Today,* **63**: 33-41 (2000).

18. Ekwall, P., Mandell, L., Fontell, ., *J. Colloid Interface Sci.* **29(4)**: 639-646 (1968).

19. Ahmad, S.I., Friberg, S., *J. Amer. Chem. Soc.,* **94(15)**: 5196-5199 (1972).

20. Houyi, N., Taichene, S., Ganzuo, L., *J. Disp. Sci. Tech.* **13(6)**: 647-656 (1992).

21. Hu, Z.S., Chen, S.Y., Peng, S.Y., *Prep. Cat. VI,* **6:** 197-206 (1995).

22. Barnickel, P., Wokaun, A., *Molec. Phys.,* **67:** 1355-1359 (1989).

23. Chen B., Goodwin, J.G., *J. Cat.,* **158**: 228-235 (1996).

24. Heiz, U., *Appl. Phys. A.,* **67:** 621-626 (1998).

25. Goodman, D.W., *Surf. Sci*., **123:** L679-L690(1982).

26. Vannice, M.A., *J. Catal.* **44:** 152-159 (1976).

27. Shaikhutdinov, Sh., Hemmeier, M., Baumer, M., Lear, T., Lennon, D., Oldman, R.J., Jackson,S.D., Freund, H.-J., *J. Catal.* **200:** 330-339 (2001).

28. McCrea, K.R., Somorjai, G.A., *J. Molec. Catal A: Chemical* **163:** 43-53 (2000).

29. Hiemenz, P.C., Rajagopalan, R., *Principles of Colloid & Surface Chemistry*. New York: Marcel Dekker, Inc., (1997).

30. www.bic.com/90oper.htm.

31. www.proterion.com/ps_dynapro.html

32. Schork, F.J., Poehlein, G.W., Wang, S., Reimers, J., Rodrigues, J., Samer, C., *Colloids Surfaces A: Physiochem. Eng.* **153:** 39-45 (1999).

33. Oxford Instruments Analytical – Technical Briefing. *Energy Dispersive X-ray Microanalysis Hardware – Explained*. EDS Instruction Manual.

34. Carboosieve S-II Spherical Carbon Conditioning Instructions, Supelco Catalog (1999 Catalog).

35. Qiu, S, Dong, J., Chen, G., *Powder Technology.* **113:** 9-13 (2000).

36. Kittel, C., *Introduction to Solid State Physics.* 4th ed. New York: John Wiley., (1971).